DEPARTMENT OF PHYSICS
TECHNISCHE UNIVERSITÄT MÜNCHEN

Study of non-thermal electron energy distribution functions by modeling of electron cyclotron emission from the fusion plasmas of the ASDEX Upgrade tokamak

Severin Sebastian Denk

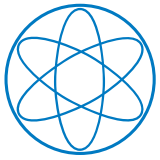

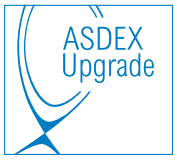

HELMHOLTZ
RESEARCH FOR GRAND CHALLENGES

EUROfusion

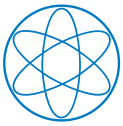

Technische Universität München

Max-Planck-Institut für Plasmaphysik

Study of non-thermal electron energy distribution functions by modeling of electron cyclotron emission from the fusion plasmas of the ASDEX Upgrade tokamak

Severin Sebastian Denk

Vollständiger Abdruck der von der Fakultät für Physik der Technischen Universität München zur Erlangung der akademischen Grades eines

Doktors der Naturwissenschaften

genehmigten Dissertation.

Vorsitzender:	Prof. Dr. Martin Zacharias
Prüfer der Dissertation:	1. Prof. Dr. Ulrich Stroth
	2. Hon.-Prof. Dr. Allen C. Caldwell

Die Dissertation wurde am 11.12.2018 bei der Technischen Universität München eingereicht und durch die Fakultät für Physik am 21.01.2019 angenommen.

DEPARTMENT OF PHYSICS
TECHNISCHE UNIVERSITÄT MÜNCHEN

Study of non-thermal electron energy distribution functions by modeling of electron cyclotron emission from the fusion plasmas of the ASDEX Upgrade tokamak

Author: Severin Sebastian Denk
Supervisor: Prof. Dr. Ulrich Stroth
Advisors: Dr. Rainer Fischer
Submission Date: 11.12.2018

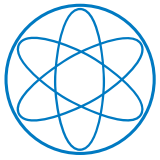

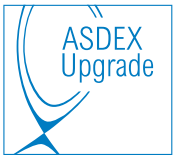

HELMHOLTZ
RESEARCH FOR GRAND CHALLENGES

EUROfusion

Abstract

Thermonuclear fusion has the potential to provide humanity with sustainable, carbon neutral and environmentally friendly energy. A leading design for a fusion reactor is the tokamak, a doughnut shaped device that utilizes magnetic fields to confine an ionized gas or plasma at a temperature of one hundred million degrees Celsius to achieve fusion. Multiple experiments have achieved a substantial amount of fusion reactions, but the energy injected into the plasma always exceeded the energy yield due to fusion reactions. The problem is the rapid pace at which plasmas lose their stored energy. To better understand and control this process further experiments, accompanied by accurate measurements of the plasma parameters are needed.

One of the key parameters for the energy transport in the plasma is the electron temperature (T_e), which needs not necessarily be equal to the ion temperature. A robust and well-established method for the determination of T_e is the measurement of the Electron Cyclotron Emission (ECE), radiated by the electrons gyrating in the magnetic field of the tokamak. Electron cyclotron emission occurs at the cyclotron frequency of the electrons and integer multiples thereof. In many cases the intensity of the ECE measured at a specific frequency is directly proportional to T_e allowing an ECE diagnostic to measure the T_e profile of the plasma with high spatial and temporal resolution.

Electrons in fusion grade plasmas reach relativistic speeds and the ECE is subject to relativistic mass-shift broadening and, if the line of sight is oblique to the magnetic field, also Doppler broadening. These two effects complicate the interpretation of ECE measurements of the plasma edge, at low optical depth, at large T_e, for viewing angles oblique to the ambient magnetic field, if resonances to multiple harmonics occur, and in case of non-Maxwellian electron velocity distributions. In the present work an existing radiation transport model was extended to include a fully relativistic absorption coefficient, cold plasma geometrical optics ray tracing. The resulting code, the Electron Cyclotron radiation transport model for Advanced Data analysis (ECRad), allows the interpretation of ECE spectra even if any or all of the limitations listed above apply. A numerically efficient and robust implementation makes ECRad suitable for the routine analysis of the ECE measurements at the tokamak ASDEX Upgrade.

The mean free path of the electrons in a plasma can be very long and a variety of processes can lead to non-Maxwellian velocity distributions. With an ECE diagnostic

it is possible to measure such distributions. Prominent examples are the distributions created by intense microwave beams used for heating fusion plasmas. This method also allows for the generation of currents, by causing an asymmetry in the distribution function. Experimentally it is very difficult to assess the efficiency of the current drive, and one is reliant on theoretical models. The ECE diagnostic is one of the few methods that can verify these models.

In this thesis the distribution functions computed by the RELAX code are tested against ECE measurements performed at ASDEX Upgrade. This work features for the first time a quantitative analysis of ECE measurements oblique to the magnetic field. It was discovered that absorption at higher order harmonics has a significant effect on the observed ECE. It was confirmed that a low, but not insignificant level of radial electron transport contributes to the steady-state distribution function in medium-sized tokamaks. Generally, a good agreement between model and measurements was found for electrons streaming in the direction of the driven current. However, an excess of electrons streaming in the opposite direction was observed in the experiments which could not be explained by RELAX.

Zusammenfassung

Kernfusion hat das Potenzial die Menschheit mit nachhaltiger, klimaneutraler und umweltfreundlicher Energie zu versorgen. Ein führendes Design für einen Fusionsreaktor ist der Tokamak, eine ringförmige Anlage, in der ionisiertes Gas, auch Plasma genannt, bei Temperaturen von einhundert Millionen Grad Celsius mittels Magnetfelder eingeschlossen wird, um Fusionsreaktionen zu ermöglichen. Eine beträchtliche Anzahl von Fusionsreaktionen wurde bereits in mehreren Experimenten erzielt, aber die in das Plasma injizierte Energie übertraf immer die Energieausbeute der Fusionsreaktionen. Das Problem ist, dass die in den Plasmen gespeicherte Energie durch Transportprozesse verloren geht. Um ein Fusionskraftwerk in die Wirklichkeit umzusetzen sind, dementsprechend, noch weitere Experimente begleitet von genauen Messungen der Plasmaparameter erforderlich.

Einer der Schlüsselparameter des Energietransports im Plasma ist die Elektronentemperatur, die nicht notwendigerweise der Temperatur der Ionen entsprechen muss. Eine robuste und gut etablierte Methode für die Bestimmung der Elektronentemperatur ist die Detektion der von den Elektronen emittierten Zyklotronstrahlung (ECE). Ihre Frequenz ist gleich der Zyklotronfrequenz der Elektronen oder einem ganzzahligen vielfachen davon. In vielen Fällen ist die gemessene Intensität direkt proportional zu der Elektronentemperatur. Das ermöglicht Elektronentemperaturprofile des Plasmas mit hoher räumlicher und zeitlicher Auflösung zu messen.

Die Elektronen in Fusionsplasmen erreichen relativistische Geschwindigkeiten. Daher wird das Spektrum der Elektronzyklotronemission durch die relativistische Massenverschiebung und, falls die Sichtlinie schräg zum Magnetfeld ist, auch durch den Doppler-Effekt, verbreitert. Beide Effekte erschweren die Interpretation des ECE-Spektrums nahe des Plasmarands, bei niedriger optischer Dicke, im Falle von hohen Elektronentemperaturen, für Blickwinkel schräg zum Magnetfeld, falls Resonanzen zu mehreren Harmonischen auf der Sichtlinie liegen oder wenn nicht-maxwellschen Elektronengeschwindigkeitsverteilungen im Plasma vorliegen. In diesee Arbeit wurde ein bereits existierendes Modell durch einen vollständig relativistischen Absorptionskoeffizienten und durch Strahlverfolgung unter der Annahme eines kalten Plasmas im Rahmen der geometrischer Optik erweitert. Mit dem entwickeltem Programm, genannt Electron Cyclotron radiation transport model for Advanced Data analysis (ECRad), können ECE-Spektren interpretiert werden, auch wenn die Auswertung der oben aufgeführten

Einschränkungen unterliegt. Dank einer effizienten und robusten Implementierung eignet sich ECRad auch für die routinemäßige Analyse der Elektronentemperatur beim Tokamak ASDEX Upgrade.

Die mittlere freie Weglänge der Elektronen in einem Plasma kann sehr groß sein, und eine Vielzahl von Prozessen kann zu nicht-Maxwellschen Geschwindigkeitsverteilungen führen. Mit der ECE-Diagnostik ist es möglich, solche Verteilungen zu bestimmen. Ein prominentes Beispiel sind Verteilungen, die durch intensive Mikrowellenstrahlung erzeugt werden, die zur Heizung von Fusionsplasmen verwendet werden. Die sogenannte Elektronzyklotronresonanzheizung ist eine der drei Hauptheizmethoden, die in der Fusion eingesetzt werden. Mit dieser Methode kann auch eine Asymmetrie in der Verteilungsfunktion verursachen was ermöglicht Strom im Plasma zu treiben. Experimentell ist es sehr schwierig, die Effizienz dieses Stromtriebs zu messen und man ist auf theoretische Modelle angewiesen. Eine der wenigen Methoden zur Überprüfung dieser Modelle ist die ECE-Diagnostik.

In dieser Arbeit werden Verteilungsfunktionen, die mit RELAX-Code berechnet werden, mit ECE-Messungen verifiziert, die am ASDEX Upgrade durchgeführt wurden. Einer der Hauptergebnisse der Arbeit ist die erstmalige, quantitative Analyse von ECE-Messungen schräg zum Magnetfeld. Des Weiteren wurde entdeckt, dass die Absorption, die an Harmonischen höherer Ordnung stattfindet, wesentliche Auswirkungen auf die beobachteten ECE haben kann. Es wurde bestätigt, dass ein niedriger, aber nicht unerheblicher radialer Elektronentransport die Verteilungsfunktion verändert. Im Allgemeinen stimmen Modell und Messungen überein für Elektronen, die sich in die Richtung des getriebenen Stroms bewegen. Jedoch wurde im Experiment ein Überschuss von Elektronen beobachtet, die in die entgegengesetzte Richtung strömen. Dies konnte nicht durch RELAX erklärt werden.

Contents

1 Introduction **1**
- 1.1 The energy problem . . . 1
- 1.2 En route to controlled thermonuclear fusion on earth . . . 1
- 1.3 Electron cyclotron waves in magnetized plasmas . . . 4
- 1.4 This thesis . . . 7

2 Modeling electron cyclotron emission and absorption **9**
- 2.1 Principle of the electron cyclotron emission diagnostic . . . 9
- 2.2 Wave propagation in a fusion plasma . . . 11
- 2.3 The radiation transport equation for electron cyclotron waves . . . 13
- 2.4 Electron cyclotron emission and absorption . . . 14
  - 2.4.1 The "polarization factor": . . . 17
  - 2.4.2 The electron momentum distribution . . . 18
  - 2.4.3 Relativistic electron cyclotron resonance . . . 18
- 2.5 The birthplace distribution of observed intensity . . . 21
- 2.6 Steady state non-thermal distribution functions . . . 25
  - 2.6.1 Electron cyclotron damping . . . 25
  - 2.6.2 Quasi-linear theory and bounce averaging . . . 28
  - 2.6.3 Loop voltage . . . 30
  - 2.6.4 Radial transport . . . 30
  - 2.6.5 Radiation reaction force . . . 30

3 Experimental Setup **33**
- 3.1 ASDEX Upgrade and its heating systems . . . 33
  - 3.1.1 ASDEX Upgrade . . . 33
  - 3.1.2 Neutral beam injection . . . 33
  - 3.1.3 Wave heating . . . 34
- 3.2 Diagnostics . . . 35
  - 3.2.1 The profile ECE diagnostic . . . 35
  - 3.2.2 The oblique ECE diagnostic . . . 37
  - 3.2.3 Thomson scattering . . . 38

3.3 Experiments with non-thermal electrons . . . 39
3.3.1 Optimization for Electron Cyclotron Emission (ECE) measurements 40
3.3.2 Validity range of the theoretical model . . . 40
3.3.3 Discharge design . . . 41
3.3.4 Experiments . . . 42

4 Data analysis techniques 45
4.1 Integrated data analysis . . . 45
4.2 The ECRad code . . . 46
4.2.1 ECRad as a forward model in Integrated Data Analysis (IDA) . 46
4.2.2 Antenna pattern . . . 47
4.2.3 Ray tracing . . . 48
4.2.4 Radiation transport . . . 48
4.2.5 Absorption and emission . . . 49
4.2.6 Wall reflections . . . 49
4.2.7 The polarization filter . . . 50
4.2.8 Input . . . 50
4.2.9 Output . . . 51
4.2.10 Interpolation of numerical distribution function profiles . . . 51
4.2.11 Graphical User Interface . . . 52
4.2.12 Validation of the ECRad code for thermal distribution functions 52
4.3 Magnetic equilibrium reconstruction – IDE . . . 55
4.4 RELAX . . . 56
4.4.1 Framework and automatic driver for RELAX . . . 56
4.4.2 Collisions and radial transport . . . 57

5 ECE analysis for thermal plasmas 59
5.1 Improved radiation transport modeling with ECRad . . . 59
5.1.1 Similarities between the two models . . . 60
5.1.2 Improvements of ECRad vs. ECFM . . . 60
5.1.3 Significance of improvements . . . 61
5.1.4 Relativistic vs. non-relativistic distribution function . . . 63
5.2 Limitations of ECRad . . . 64
5.2.1 The Abraham–Lorentz force . . . 64
5.2.2 Wall reflections . . . 66
5.2.3 O-mode emission during X-mode cutoff . . . 67
5.2.4 Influence of O-mode for routine ECE measurements . . . 69
5.3 Applications of electron cyclotron radiation transport modeling . . . 70
5.3.1 "Pseudo radial displacement" in the plasma core . . . 70

5.3.2 3rd harmonic emission and harmonic overlap . . . 72
5.4 Cross calibration of oblique ECE diagnostics . . . 75
5.4.1 Interpretation of oblique ECE diagnostics . . . 76
5.4.2 Cross-Calibration method . . . 77
5.4.3 Examples . . . 78
5.5 Further applications of ECRad . . . 82
5.6 Conclusions . . . 83

6 Analysis of non-thermal ECE spectra during electron cyclotron current drive (ECCD) 85
6.1 Preparation and validity check of the RELAX and ECRad calculations 86
6.1.1 Kinetic profiles as input for RELAX . . . 86
6.1.2 Geomtrical vs. quasi-optical beam tracing . . . 89
6.1.3 Configuration and validation of the GRAY calculations . . . 90
6.1.4 Validation of RELAX and ECRad in case of linear damping . . . 93
6.2 Basic calculations with RELAX and ECRad . . . 95
6.3 Phase space sensitivity of ECE . . . 96
6.3.1 Oblique ECE . . . 96
6.3.2 Radial ECE . . . 100
6.4 Parallel electric field and radiation reaction force . . . 106
6.4.1 Parallel electric field . . . 107
6.4.2 Radiation reaction force . . . 108
6.5 Radial diffusion with ECE . . . 108
6.6 Conclusions . . . 112

7 Summary and Outook 115

Appendix 119
1 Upper limit estimate for the absorption coefficient . . . 119
2 Wall reflection model assuming isotropic back ground . . . 120
3 Output of ECRad . . . 122
4 Most important parameters of the RELAX calculations . . . 123

Glossary 129

Acronyms 131

Bibliography 135

Acknowledgments 147

1 Introduction

1.1 The energy problem

Global warming, an ever rising world population and the receding amounts of fossil fuels make energy production one of the most substantial challenges for humanity today and even more so in the not so distant future. Even though great effort has been made to decrease the production of greenhouse gases, the amount of energy that can be gained through renewable, carbon neutral, resources is limited. The four main, carbon neutral, renewable energy sources are hydroelectric, solar and wind power. Furthermore, there is the production of bio fuels. Solar and wind power are not capable of delivering power continuously and there is currently no economically viable method for large scale energy storage. Hydroelectric power and bio fuels could compensate for the fluctuations in power output, but they consume extensive amounts of land mass and have a considerable environmental imprint. Hence, with current technologies it is not possible to make the transition to sustainable, carbon neutral and environmentally friendly energy production. Nuclear fission could be considered as an exception to this. Fission power plants are carbon neutral and the fuel for breeder type fission reactors is available in almost unlimited quantities [1]. However, the policies and technology employed for the long term storage of nuclear waste raise some concerns on whether nuclear fission qualifies truly as sustainable. Nevertheless, harnessing the binding energy of nuclei is extremely attractive, due to its vast energy yield per reaction. This energy can also be accessed by combining very light nuclei, which is called nuclear fusion.

1.2 En route to controlled thermonuclear fusion on earth

In order for two nuclei to fuse they need to be brought into the immediate proximity of each other. This does not occur naturally on earth, because nuclei are positively charged and repel each other. In nature this force can only be overcome in the core of stars where the massive gravitational force provides the pressure necessary for the fusion reaction. In laboratories nuclear fusion can be achieved by a variety of methods.

This particular work falls within the field of magnetic confinement fusion.

The development of a thermonuclear reactor is one of main goals in magnetic confinement fusion research. Such a fusion power plant would deliver sustainable, environmentally friendly and carbon neutral electricity. The fuel for the power plant is an even mixture of deuterium and tritium, the two isotopes of hydrogen. This particular fuel is chosen, because the fusion reaction of deuterium and tritium occurs already at comparatively low particle energies:

$$ {}^{2}_{1}\mathrm{D} + {}^{3}_{1}\mathrm{T} = {}^{4}_{2}\mathrm{He}^{2+}\,(3.5\,\mathrm{MeV}) + {}^{1}_{0}\mathrm{n}\,(14.1\,\mathrm{MeV}) \tag{1.1} $$

The fusion reaction produces a helium nucleus or alpha particle and a highly energetic neutron. Since the alpha particle is charged it is confined by the magnetic fields and can pass its energy to the deuterium and tritium ions. The neutron, on the other hand, is not confined and its energy can be used for the generation of electricity.

The fuel of the reactor is ecologically sound. The deuterium can be extracted from sea water. Tritium does not occur naturally, because it is radioactive with a comparatively short half-life of 12.3 years. Accordingly, it has to be created artificially by bombarding lithium with neutrons. Due to the extremely high energy yield of the fusion reaction, a fusion reactor consumes very little lithium. Half of the energy consumption of the world in 2008 could be covered by the tritium bred from less than a ton of lithium assuming a 50 % conversion rate from fusion energy to electricity. In current concepts the tritium is breed directly inside the reactor utilizing the neutrons of the fusion reaction. Even though the large neutron flux inside a thermonuclear reactor is convenient for the production of tritium, it raises two major challenges in the design of the reactor vessel [2]. First, neutron radiation alters material properties like the tensile, compressive and shear strength and, second, it creates radioactive isotopes. This limits the lifetime of any component subject to the neutron radiation and complicates the management of any decommissioned component. It also means that fusion reactors are a source of radioactive waste despite the fusion reaction itself being free of long-lasting radioactive products. However, unlike the radioactive waste produced by fission reactors it is possible to select the materials used for the reactor components such that the majority of the scrap material can be recycled after about a hundred years of storage [3].

As the name already indicates a magnetic confinement fusion reactor utilizes magnetic fields to confine the fuel. To initiate the fusion reaction a small quantity of gaseous fuel is injected into the vacuum chamber and heated to a 100 million degrees Kelvin. At these temperatures the deuterium-tritium fuel is in the plasma state. In a plasma the electrons and ions are dissociated and form a conductive fluid [4]. This causes the trajectories of the plasma particles to react to magnetic fields enabling the magnetic confinement scheme. In a tokamak type fusion reactor the plasma is confined in a

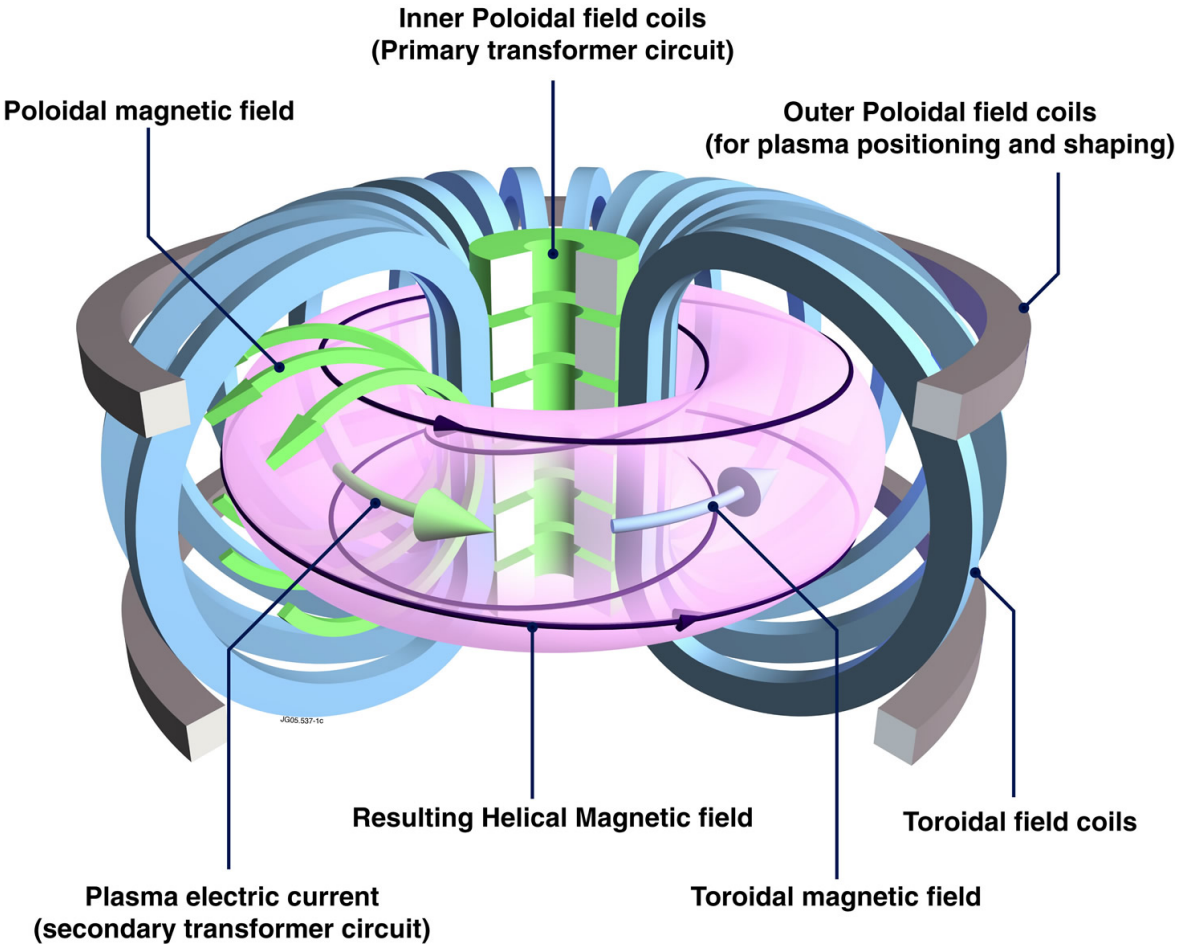

Figure 1.1: Illustration of the coils and magnetic fields in a tokamak. The toroidal field coils and the toroidal magnetic field are indicated in light blue. The central solenoid, the plasma current and the poloidal magnetic field are shown in light green. The shaping coils are displayed in gray. The magenta shaded torus is the confined plasma.

torus shape. This is achieved with the magnetic fields illustrated in Fig. 1.1. The fields can be separated into two components – the *toroidal* and the *poloidal* magnetic field. The toroidal magnetic field (light blue arrow in Fig. 1.1) is created by a set of coils arranged periodically around the torus (light blue in Fig. 1.1). By continuously increasing or decreasing the current of the central solenoid (green discs in the center) the toroidal *plasma current* (green arrow) is driven which, in turn, creates the poloidal magnetic field (green arrows). The plasma current can be sustained by the central solenoid for a limited time, only. Hence, for continuous operation the plasma current has to be supplied by other means, for example limited and for continuous operation other methods. Beside the central solenoid and the toroidal magnetic field coils there are also large coils near the top and bottom on the outer side of the torus (gray in Fig. 1.1). These coils elongate the plasma vertically while also improving stability.

To date no magnetically confined fusion experiment has ever achieved a positive energy balance, where the energy yield from the fusion reactions exceeds the power injected into the plasma. The main obstacle is the rate at which the plasmas loose energy. Several mechanics cause the plasma to leak energy – first and foremost turbulent transport. In order to understand related processes and validate theoretical models it is essential to assess the properties of plasmas in experiments. One of the fundamental qualities is the velocity distribution of the electrons. If the electrons are thermally distributed it is sufficient to measure electron temperature (T_e), but in non-thermal plasmas the velocity distribution function needs to be resolved. One method to measure T_e of most plasmas and the velocity distribution of some plasmas is the Electron Cyclotron Emission (ECE) diagnostic [5–7]. The description and explanation of ECE of fusion plasmas is the topic of this thesis.

1.3 Electron cyclotron waves in magnetized plasmas

Electron cyclotron emission is due to bremsstrahlung by the electrons gyrating in a magnetic field. The gyromotion of an electron in a magnetic field is illustrated in Fig. 1.2. The ECE of magnetically confined fusion plasmas lies in the upper microwave to lower terahertz range and the diagnostic has to be sensitive enough to measure spectral intensities of the order of $1\,\mu\mathrm{W\,cm^{-2}\,GHz^{-1}}$. These requirements are technically challenging, but the capability of ECE diagnostics to provide spatially and temporarily highly resolved measurements of T_e makes the technique very attractive. Accordingly, an ECE diagnostic can be found at nearly every major magnetic confined fusion device: JET [8–10], ASDEX Upgrade [11–13], DIII-D [14–16], W7-X [17], LHD [18, 19], KSTAR

[20, 21], ect. The present work exploits data from ASDEX Upgrade[1] of the Max-Planck Institute for Plasma Physics in Garching.

The radius of the electron cyclotron motion is the Larmor radius

$$\rho_{\mathrm{L}} = \frac{m_{\mathrm{e}} v_{\perp}}{eB}, \tag{1.2}$$

with the electron velocity perpendicular to the magnetic field $v_{\perp}$, the elementary charge e, the electron mass m_{e} and the total magnetic field strength B. The electrons gyrate with the (angular) cyclotron frequency

$$\omega_{\mathrm{c}} = \frac{eB}{m_{\mathrm{e}}} \tag{1.3}$$

around magnetic field lines and emit electromagnetic radiation at the cyclotron frequency. In fusion plasmas the Larmor radius is comparable to the wave length of the ECE. Consequently ECE also occurs at integer harmonics n of the cyclotron frequency.

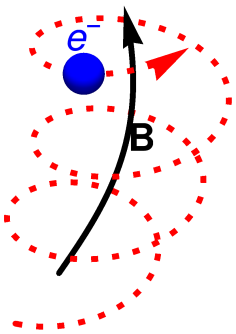

Figure 1.2: Gyration of an electron in a magnetic field.

The magnetic field strength in a tokamak is approximately proportional to the inverse of the major radius of the torus $B \propto 1/R$. The radial dependence of B and T_{e} are illustrated in Fig. 1.3. For ECE it is useful to distinguish between the high-field side (HFS) and the low-field side (LFS). As the names suggest and indicated in Fig. 1.3 the magnetic field on the HFS (LFS) is larger (smaller) than the magnetic field strength at the center of the plasma. Since the cyclotron frequency is unique for each radial position the intensity I_{ω} measured at a frequency ω can be mapped to a unique position, where the resonance condition $\omega = n\omega_{\mathrm{c}}(R)$ is met. For this treatment the finite velocity of the electrons in a plasma is neglected. Accordingly, this position is referred to as the *cold resonance position*. The conversion of the measured intensities to T_{e} is straightforward in many cases. For low harmonics $n < 3$ the plasma is also a strong absorber and the ECE can be considered as low frequency black body radiation which is directly proportional to T_{e} according to the Rayleigh-Jeans law. This procedure for the evaluation of ECE measurements will be referred to as *classical ECE analysis* in the following.

Classical ECE analysis is not always appropriate. The main problem is caused by the relativistic mass increase and the Doppler shift. Both effects cause the frequency of the ECE to be dependent on the velocity of the electron. Usually the electron velocities in

[1] ASDEX Upgrade stands for Axially Symmetric Divertor Experiment Upgrade

a tokamak are distributed according to a Maxwellian. Accordingly, electrons located at a specific point in the plasma have a wide variety of velocities and their ECE spectrum is broad instead of line-shaped.

To mitigate the broadening, ECE diagnostics usually view the plasma from the LFS with a line of sight (LOS) that is perpendicular to the magnetic field. The latter suppresses the Doppler effect and the former allows down-shifted emission due to the relativistic mass-increase to be absorbed near the cold resonance position. In case of weak absorption, positions other than the cold resonance position contribute to the measurement and it is inappropriate to approximate the measurement position as the cold resonance position. This challenge can be overcome if radiation transport of ECE in the plasma is considered [22]. This was demonstrated in Ref. [11], where the ECE measurements of the plasma edge affected by weak absorption could be successfully interpreted with a radiation transport forward model.

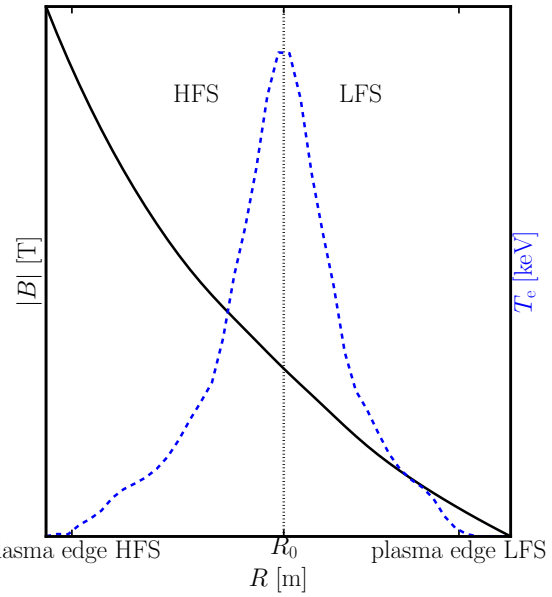

Figure 1.3: Radial dependence of the magnetic field (solid black line) and T_e (dashed blue line and right y-axis) in a tokamak. The center of the plasma at R_0 is marked by the vertical dashed line. The edges of the confined region are indicated as well as the HFS and the LFS.

Another problem for classical ECE analysis is posed by non-Maxwelian distributions, for which the conversion from intensities to electron temperatures via the Rayleigh-Jeans law is inappropriate. An example for a source of non-thermal distributions is electron cyclotron resonance heating (ECRH). For this heating method a focused microwave beam is injected into the plasma. The small diameter of the beam and the resonance condition allow for great control on where this power will be absorbed in the plasma. Because of this ability most magnetic confined fusion experiments feature an ECRH system [23–29]. If injected obliquely to the magnetic field, ECRH preferentially heats electrons that travel in a particular direction parallel to the magnetic field. This allows ECRH to create significant currents at the deposition site [30]. This technique is called electron cyclotron current drive (ECCD). It is a powerful asset in the design and control of high performance fusion plasmas. For example, it is expected to be essential to stabilize performance limiting neoclassical tearing modes in the International Thermonuclear Experimental Reactor [31]. To exploit ECCD to its fullest potential it is critical to know the *current drive*

efficiency, i.e. how many Ampères of current are driven by each Watt of microwave power. This quantity is difficult to measure in experiments and one is reliant on codes like RELAX [32], LUKE [33] or CQL3D [34] to compute it. These codes have in common that they are unable to model radial electron transport, which is known to reduce the current drive efficiency [7] and diminish the good localization of ECCD [7, 35]. At smaller tokamaks, like TCV, turbulent transport reduces the ECCD efficiency more strongly than at medium tokamaks like DIII-D [36, 37]. Furthermore, turbulence becomes especially important if the density of the deposited power is large [7, 38]. For the planned tokamak International Thermonuclear Experimental Reactor, which will be much larger than DIII-D, the foreseen power densities are very low and that turbulent transport is not expected to be detrimental for the ECCD efficiency and the localization [39]. Hence, for the current design of the ECRH system at International Thermonuclear Experimental Reactor it is assumed that codes like RELAX are accurate.

In the studies above the ECCD efficiency was derived from the profile of the total current, which consists of the current due to ECCD and the current driven by the central solenoid, the latter being very difficult to measure. Furthermore, the loop voltage induced by the transformer can interact non-linearly with ECCD further complicating the deconvolution of the total current into its individual components. These challenges can be avoided if the validation of the computed ECCD efficiency is achieved by the direct measurements of the electron distribution function [6, 40–42]. Of particular interest are ECE measurements which are very sensitive to the effect of ECCD on the distribution [6, 41]. However, all past studies of this kind were of a purely qualitative nature and a quantitative benchmark between modeled and experimentally observed distribution functions is still lacking.

1.4 This thesis

This work extends upon that of Ref. [11], where the radiation transport technique was only applied with the specific purpose of recovering T_e near the plasma edge. The radiation transport model of Ref. [11] was upgraded and the resulting code was named Electron Cyclotron radiation transport model for Advanced Data analysis (ECRad). With this code the ECE spectra of non-thermal electrons can be interpreted. Furthermore, a robust and fast implementation combined with the generalized physical model allows the large scale Integrated Data Analysis (IDA) of the ECE measurements to be performed at ASDEX Upgrade.

For the interpretation of ECE measurements one of two strategies is chosen depending on whether the ECE is due to thermal or non-thermal distributions. For Maxwellian distributed electrons, radiation transport modeling in the framework of IDA extents

the operational space of the ECE diagnostics and increases the accuracy of the inferred T_e profile. Another benefit of the IDA approach is that the limitations of ECRad could be clearly identified. The main results achieved in the case of thermal plasmas include an improved understanding of ECE spectra at large T_e values, a reliable method for the interpretation of measurements affected by harmonic overlap, and the analysis of measurements of oblique ECE diagnostics.

In case of non-thermal plasmas a direct reconstruction of the electron distribution function from the ECE is not possible, since the distribution has too many degrees of freedom. Instead, radial and, for the first time, oblique ECE measurements perfomed at the ASDEX Upgrade tokamak are exploited to verify the distribution functions computed by the Fokker-Planck code RELAX [32]. For this purpose discharges optimal for distribution function measurements with ECE were designed. Guided by these measurements ordinary mode (O-mode) polarized ECE due to non-thermal electrons and the contribution of higher order harmonics to the ECRH absorption were identified as crucial for the interpretation of ECE by non-thermal plasmas. Furthermore, the measurements allow the level of radial electron transport to be estimated. Lastly, the sensitivity of ECE to the velocity dependence of the radial transport is tested.

This thesis consists of a theory chapter, two methodological chapters and three result chapters. In the next chapter the details of electron cyclotron radiation transport and the physics of ECCD are discussed. In Chapter 3 the tokamak ASDEX Upgrade, the measurement hardware, and the experiments designed for this thesis are presented. The data analysis methods are explained in Chapter 4. The benefits of radiation transport modeling for the inference of T_e from ECE measurements are discussed using examples in Chapter 5. The sensitivity of ECE on ECCD induced non-thermal plasmas is investigated in Chapter 6. The most important results are summarized in Chapter 7.

2 Modeling electron cyclotron emission and absorption

This section introduces the individual aspects of electron cyclotron waves that are required for the construction of a synthetic ECE diagnostic. Another topic is the quasi-linear damping of electron cyclotron waves and a corresponding deviation of the distribution function from the thermal equilibrium.

2.1 Principle of the electron cyclotron emission diagnostic

In this section we describe the principle of what we refer to as *classical ECE analysis*. Classical ECE analysis assumes a cold plasma, i.e. any effect due to the finite electron velocity is neglected. Consequently, broadening due to the relativistic mass increase and the Doppler shift are neglected. These effects will be included later in Section 2.4. For cold electrons the resonance condition becomes

$$\omega = n\omega_{\mathrm{c},0} = n\frac{eB}{m_{\mathrm{e},0}}, \tag{2.1}$$

where the cyclotron frequency is replaced by the cold plasma cyclotron frequency $\omega_{\mathrm{c},0}$. Here the electron rest mass $m_{\mathrm{e},0}$ was introduced. As can be seen from n appearing in the resonance condition, higher order harmonics $n > 1$ are considered in classical ECE analysis, even through they are a finite electron velocity effect. This resonance condition provides the good localization of ECE measurements, because electron-cyclotron emission and absorption only occur if it is fulfilled.

With classical ECE analysis the measurements can be evaluated in two steps. First the cold resonance position on the LOS of the diagnostic is obtained. This is done by solving $\omega = n\omega_{\mathrm{c},0}(R_{\mathrm{res}})$, for the point R_{res} on the LOS. This point is called the *cold resonance position*. It is useful to transfer this position into a magnetic coordinate system. Commonly used are the flux of the poloidal magnetic field through the toroidal plane, i.e. the *poloidal magnetic flux* Ψ_{pol}, and the flux of the toroidal mangetic field

through the poloidal plane, i.e. the *toroidal magnetic flux* Φ_{tor}. In this work the coordinate of choice is the square root of the normalized poloidal magnetic flux ρ_{pol}:

$$\rho_{\mathrm{pol}} := \sqrt{\frac{\Psi_{\mathrm{pol}} - \Psi_{\mathrm{pol,ax}}}{\Psi_{\mathrm{pol,sep}} - \Psi_{\mathrm{pol,ax}}}} \tag{2.2}$$

Where Ψ_{ax} is the poloidal flux through the ring defined by the magnetic axis, the center of the plasma. Similarly, Ψ_{sep} is the flux through the ring formed by the boundary of the confined plasma. The advantage of this system is that it allows a 1D representation of the initially two-dimensional (R, z) T_{e} profile. This is possible because the electrons can travel quickly in the direction of constant magnetic flux, while their movement perpendicular to these surfaces is strongly inhibited. This causes T_{e} and also the electron density (n_{e}) to be constant on flux surfaces. In Fig. 2.1 the LOS of an ECE diagnostic is indicated in the poloidal cross-section of ASDEX Upgrade. The contours indicate the shapes of flux surfaces. The surfaces are closed for $\rho_{\mathrm{pol}} < 1.0$ and, open contours otherwise. At the very center of the plasma lies the magnetic axis for which $\rho_{\mathrm{pol}} = 0$.

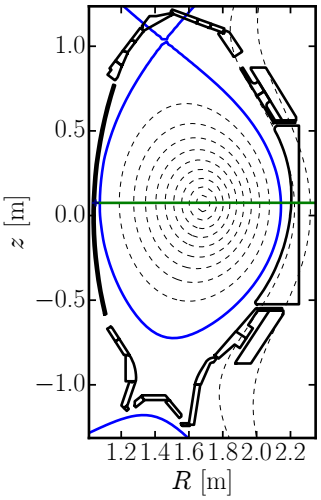

Figure 2.1: Poloidal cross section of ASDEX Upgrade with the LOS of an ECE diagnostic. Contours of the square root of the normalized poloidal flux are indicated.

In the second step the measured intensities are converted to temperatures. Since it is assumed that the observed intensity I_ω is black body radiation, the electron temperature at the cold resonance is given by

$$T_{\mathrm{e}} \approx \frac{8\pi^3 c_0^2}{\omega^2} I_\omega \tag{2.3}$$

with c_0 the vacuum speed of light and I_ω the measured, spectral wave intensity. Classical ECE analysis is insufficient, if absorption at the cold resonance position is too weak for the intensity to reach thermodynamic equilibrium with the plasma at the cold resonance position or if the velocity of the electrons is not normally distributed. Similar problems arise if positions other than the assigned cold resonance position contribute significantly to the observed intensity. In both cases the temperature derived from Eq. (2.3) is not an electron temperature but rather a radiation temperatures (T_{rad}). If classical ECE analysis is not valid, the radiation transport in the plasma needs to be considered to recover the T_{e} profile from T_{rad} measurements. How this is accomplished is the topic of the next

sections.

2.2 Wave propagation in a fusion plasma

To solve the radiation transport equation it is necessary to know the trajectory of the electron cyclotron waves in the plasma. Fusion plasmas are dispersive media for waves in the electron cyclotron range of frequencies. Hence, the radiation is subject to refraction and the LOSs of ECE diagnostics are not straight. The magnitude of the refraction depends on the polarization of the wave. In the cold plasma approximation, which is still used in this section, electron cyclotron waves can exist in two, decoupled polarization states. If the wave vector $\boldsymbol{k}$ of the waves is perpendicular to the ambient magnetic field $\boldsymbol{B}$ the two states are called the O-mode and the extraordinary mode (X-mode). For $\boldsymbol{k} \perp \boldsymbol{B}$ the O-mode is linearly polarized and its electric field is parallel to $\boldsymbol{B}$. If finite density effects are neglected, the X-mode is also linearly polarized, but its electric field is perpendicular to the plain spanned by $\boldsymbol{k}$ and $\boldsymbol{B}$. For finite electron densities the X-mode is elliptically polarized and it has a longitudinal, electrostatic component [43]. The electrostatic component is induced by the $\boldsymbol{E} \times \boldsymbol{B}$ force of the electric field of the wave and the background magnetic field. The terms X- and O-mode are, strictly speaking, only valid for propagation perpendicular to the magnetic field. However, this nomenclature is, nowadays, also used for arbitrary propagation directions [43] and for simplicity's sake this generalization is also used in this work.

Independent of the polarization state the trajectory of electron cyclotron waves can be described by geometrical optics [43], if the inhomogeneity scale of the plasma is large compared to the wavelength such that the WKB approximation holds [44]. In this case the path of the wave through the plasma can be obtained by solving the geometrical optics equations

$$\frac{\mathrm{d}\boldsymbol{x}}{\mathrm{d}s} = \left.\frac{\partial\Lambda/\partial\boldsymbol{N}}{|\partial\Lambda/\partial\boldsymbol{N}|}\right|_{\Lambda=0}; \qquad \frac{\mathrm{d}\boldsymbol{N}}{\mathrm{d}s} = -\left.\frac{\partial\Lambda/\partial\boldsymbol{x}}{|\partial\Lambda/\partial\boldsymbol{N}|}\right|_{\Lambda=0}. \tag{2.4}$$

The arclength is given by s and $\boldsymbol{x}$ is the spatial coordinate. The second canonical coordinate is $\boldsymbol{N} := \frac{c_0\boldsymbol{k}}{\omega}$ with $\boldsymbol{k}$ the wave vector. With Λ the cold plasma dispersion relation Eq. (2.5).

The index of refraction $N_{\mathrm{s},\omega}$ derived from the dispersion relation depends on the frequency of the waves, n_e and, in case of X-mode polarization, also on the total, equilibrium, magnetic field strength $B = |\boldsymbol{B}|$. For the determination of the LOS of an ECE diagnostic it is possible to neglect finite T_e effects for medium-sized tokamaks like ASDEX Upgrade [43]. If kinetic effects are disregarded, there are two roots in the

dispersion relation $\Lambda(\boldsymbol{x}, \boldsymbol{k}, \omega)$:

$$\Lambda(\boldsymbol{x}, \boldsymbol{N}, \omega) = |\boldsymbol{N}|^2 - N_{\mathrm{s},\omega}^2\left(X, Y, N_\parallel\right) \tag{2.5}$$

with $N_{\mathrm{s},\omega}$ the cold plasma refractive index [43]

$$N_{\mathrm{s},\omega}\left(X, Y, N_\parallel\right) = 1 - X - XY^2\frac{1 + N_\parallel^2 \pm \Delta}{2(1 - X - Y^2)}, \tag{2.6}$$

where

$$\Delta := \sqrt{(1 - N_\parallel^2)^2 + 4N_\parallel^2\frac{1 - X}{Y^2}} \tag{2.7}$$

In Eq. (2.5) the normalized plasma frequency $X = \frac{\omega_\mathrm{p}^2}{\omega^2}$ with the plasma frequency $\omega_\mathrm{p} = \sqrt{\frac{e^2 n_\mathrm{e}}{\epsilon_0 m_{\mathrm{e},0}}}$ and the normalized cyclotron frequency $Y := \frac{\omega_{\mathrm{c},0}}{\omega}$ were introduced. The vacuum permittivity ϵ_0 has its usual notation. The angle between the wave vector and the magnetic field is

$$\theta = \arccos\left(\frac{\vec{k}\cdot\vec{B}}{|\vec{k}|\cdot|\vec{B}|}\right). \tag{2.8}$$

The component of $\boldsymbol{N}$ that is aligned with the magnetic field is denoted as $N_\parallel = |\boldsymbol{N}|\cos\theta = \frac{\boldsymbol{N}\cdot\boldsymbol{B}}{|\boldsymbol{B}|}$. Accordingly, the component perpendicular to the magnetic field is analogously defined as $N_\perp = |\boldsymbol{N}|\sin\theta$. The "+" in Eq. (2.6) corresponds to the X-mode and "−" corresponds to the O-mode.

The two relations in Eq. (2.4) form a system of two coupled, ordinary three-dimensional differential equations, which have to be solved numerically. The ray paths given by the Hamiltonian system fulfill reciprocity. This is important as the focus of this work is the modeling of ECE diagnostics where the origin of the ECE is not known, but the position of the antenna is. Due to reciprocity of the Hamiltonian system the rays can be launched from the ECE antenna to determine the path of the radiation traveling through the plasma to the ECE antenna.

Generally the cold dielectric tensor is sufficient to describe the ray paths in a plasma and it is common practice to disregard kinetic effects in the computation of the trajectory of cyclotron waves with ray and beam tracing codes [45–48]. There is, however, an important exception where this practice is inaccurate. Near cut-off layers, where the refractive index becomes purely imaginary, there can be a considerable influence by kinetic effects [49]. Due to the large speed of the electrons, relativistic effects allow

propagation of electron cyclotron waves even if the refractive index given by the cold dispersion relation is purely imaginary. One encounters two problems, when calculating the ray paths from the fully relativistic dielectric tensor. The first is the highly oscillatory nature of the real part of the refractive index near a resonance and that the group velocity of the wave approaches zero [50]. The other problem is of technical nature. To date there is no analytical solution to the fully relativistic dispersion relation and instead an extensive numerical approach is required. Although, it was shown in Ref. [50] that propagation through a resonance can alter the wave path due to kinetic effects, most ray- and beam tracing codes rely on the cold plasma dispersion relation [45–48], because of these complications. The argument is that the deformation of the ray/beam due to resonances is negligible, because the spatial extent of the resonance is very small [51]. Nevertheless, there are codes that consider a rigorous weakly relativistic dielectric tensor for the wave propagation (e.g. [52]).

Independent of the choice of the dispersion relation the geometrical optics equations describe the path of the waves through the plasma. To attain the evolution of the energy flux of the waves it is necessary to solve the radiation transport equation along this path.

2.3 The radiation transport equation for electron cyclotron waves

The transport of radiation in an optically active medium is governed by the radiation transport equation [22]:

$$\frac{\mathrm{d}}{\mathrm{d}s}\frac{I_\omega(s)}{N^2_{\omega,\mathrm{ray}}(s)} = \frac{1}{N^2_{\omega,\mathrm{ray}}(s)}\left(j_\omega(s) - \alpha_\omega(s) I_\omega(s)\right). \tag{2.9}$$

The coordinate of the path along which the radiation propagates is the arc-length s and $N_{\omega,\mathrm{ray}}$ is the ray refractive index [22]. The absorption coefficient is denoted as $\alpha_\omega(s)$ and captures the relative loss of intensity due to wave absorption. The source term is the emissivity $j_\omega(s)$. Section 2.4 shows, how these two quantities can be calculated. Integrating Eq. (2.9) over the path of the ray yields the intensity $I_\omega(s_{\mathrm{ow}})$ for a measured frequency ω at the position of the outer wall s_{ow}. In practice this is the point where the radiation leaves the plasma vessel and is detected.

For the interpretation of ECE the values I_ω inside the plasma are irrelevant and only $I_\omega(s_{\mathrm{ow}})$ is of importance. In this case it is possible to set $N_{\omega,\mathrm{ray}}$ to one in Eq. (2.9).

This can be proven by inserting Kichhoff's law (cf. Eq. (2.15) below) into Eq. (2.9):

$$\frac{\mathrm{d}}{\mathrm{d}s}\frac{I_\omega(s)}{N^2_{\omega,\mathrm{ray}}(s)} = \alpha_\omega(s) I_{\mathrm{BB},\omega} - \alpha_\omega(s)\frac{I_\omega(s)}{N^2_{\omega,\mathrm{ray}}(s)}, \tag{2.10}$$

where $I_{\mathrm{BB},\omega}$ denotes the black body intensity. Introducing $I_\omega \equiv N^2_{\omega,\mathrm{ray}}\tilde{I}_\omega$ renders Eq. (2.10) independent of $N_{\omega,\mathrm{ray}}$. In vacuum at $s = s_{\mathrm{ow}}$ the ray refractive index is one and, therefore, $I_\omega(s_{\mathrm{ow}}) = \tilde{I}_\omega(s_{\mathrm{ow}})$. Although Kirchhoff's law was considered in this derivation, it can be shown that this approximation also holds for non-thermal distributions [43].

2.4 Electron cyclotron emission and absorption

To solve the radiation transport Eq. (2.9) the emissivity $j_\omega(s)$ and the absorption coefficient $\alpha_\omega(s)$ have to be calculated. In a tenuous plasma, where dispersion is negligible, the collective motion of the electrons can be neglected and the emissivity and absorption coefficient can be calculated as the sum of the contribution of each electron. Hence, the emissivity is given by the velocity space integral of the single electron emissivity weighted with the distribution function [5]. This approach requires that the refractive index $N_{\mathrm{s},\omega} \approx 1$. For plasma scenarios typical of ASDEX Upgrade and for the frequency range for which ECE is a useful diagnostic this criterion does usually not apply.

Hence, the dielectric properties of the plasma have to be retained when calculating the emissivity. This requires the knowledge of the complex wave vector $\boldsymbol{k}$, which fulfills the fully relativistic dispersion relation locally. However, to obtain the complex wave vector it is necessary to solve the fully relativistic dispersion relation for the complex refractive index [53]. To date no analytical solution to this problem is available and it has to be solved numerically.

Unlike the cold plasma dispersion relation, the fully relativistic dispersion relation exhibits more than two roots. Aside from roots that correspond to the X- and O-mode there are also roots that belong to electrostatic Bernstein waves [43]. Especially close to a resonance the roots corresponding to Bernstein modes can lie close or can even coincide with the roots of the X- and O-mode [54]. Since there is no scheme readily available that can reliably separate X- and O-mode roots from the Bernstein roots, the numerical root finding method delivers for certain scenarios a complex refractive index that is a solution for a Bernstein wave. Although a comparatively robust solution to this problem exists [53] the success rate of this method proved insufficient in practice to be viable for the large scale data analysis targeted in this thesis. Hence, a compromise

between the complete treatment and the tenuous plasma approach had to be found for this thesis.

A viable approximation for the absorption coefficient that retains the dielectric properties of the cold plasma is proposed in Ref. [55]. This approach can inherently only consider the electromagnetic energy flux of the wave, while the so-called sloshing flux, which is non-zero only if finite temperature effects are included in the dispersion relation, has to be neglected [55]. Furthermore, the refractive index $N_{\mathrm{s},\omega}$ of the plasma and the polarization of the wave only account for the cold dielectric tensor. The advantage is that the absorption coefficient and the emissivity can be expressed as an integral in momentum space that can be easily and robustly solved numerically. With these approximations it is possible to derive the emissivity of the n-th harmonic from the absorption coefficient given by Ref. [55] from equation (2.9) of Ref. [56] [57]

$$\begin{aligned} j_{\omega,n}(s) = \frac{N_{\omega,\mathrm{ray}}^2 \omega_{\mathrm{p},0}^2 \omega}{2\pi c_0^3} \iint \underbrace{\left(\frac{n}{\bar{\omega} N_\perp}\right)^2 \left| \left(e_x + \frac{\bar{\omega} N_\perp}{n} u_\parallel e_z\right) J_n(b) - \frac{ib}{n} J_n'(b) e_y \right|^2}_{\text{"Polarization factor"}} \times \\ \underbrace{f(s, u_\perp, u_\parallel)}_{\text{electron distribution function}} \times \\ \underbrace{\delta\left(\gamma - u_\parallel N_\parallel - \frac{n}{\bar{\omega}}\right)}_{\text{Resonance cond.}} \frac{u_\perp}{\gamma} \mathrm{d}u_\perp \mathrm{d}u_\parallel. \end{aligned} \tag{2.11}$$

The absorption coefficient for harmonic number n can be directly adopted from Ref. [55] and only the ray refractive index needs to be added to the expression [43]

$$\begin{aligned} \alpha_{\omega,n}(s) = 4\pi^2 \frac{{\omega_{\mathrm{p},0}}^2}{c_0 \omega} \iint \underbrace{\left(\frac{n}{\bar{\omega} N_\perp}\right)^2 \left| \left(e_x + \frac{\bar{\omega} N_\perp}{n} u_\parallel e_z\right) J_n(b) - \frac{ib}{n} J_n'(b) e_y \right|^2}_{\text{"Polarization factor"}} \times \\ \underbrace{\hat{R} f(s, u_\perp, u_\parallel)}_{\text{directional derivative of electron distribution function}} \times \\ \underbrace{\delta\left(\gamma - u_\parallel N_\parallel - \frac{n}{\bar{\omega}}\right)}_{\text{Resonance cond.}} \frac{u_\perp}{\gamma} \mathrm{d}u_\perp \mathrm{d}u_\parallel. \end{aligned} \tag{2.12}$$

Both, the emissivity and the absorption coefficient contain an integral in cylindrical, dimensionless momentum space, with $u_{\perp/\parallel} = p_{\perp/\parallel}/(c_0 m_{\mathrm{e},0})$ the (dimensionless) momentum perpendicular/ parallel to the magnetic field. The Lorentz factor is denoted as

$\gamma = \sqrt{1 + u_\perp^2 + u_\parallel^2}$ and $\bar{\omega}$ is defined as $\bar{\omega} := \frac{\omega}{\omega_{c,0}}$. The coordinate system for the polarization vector $\boldsymbol{e} = (e_x, e_y, e_z)$ normalized by the Poynting flux follows the convention used by Stix, where the x and z axes are chosen such that $\boldsymbol{k}$ lies in the x-z plane and z axis is aligned with $\boldsymbol{B}$ [44]. The Bessel function of first kind is denoted as $J_n(b)$ with n-th order and $b := \bar{\omega} N_\perp u_\perp$. Note that most of these quantities depend implicitly on the ray coordinate s. The absorption coefficients distinguishes itself from the emissivity by a factor and the operator $\hat{R}$ that is applied onto the electron distribution function.

$$\hat{R} := \frac{n}{\bar{\omega}} \frac{1}{u_\perp} \frac{\partial}{\partial u_\perp} + N_\parallel \frac{\partial}{\partial u_\parallel}. \tag{2.13}$$

The distribution function can be arbitrarily chosen in Eqs. (2.11) and (2.12). For the wave absorption the gradients of the distribution function in the directions of $u_\perp$ and $u_\parallel$ are the relevant quantities and not the distribution itself, while for the emissivity the distribution functions enters the equation directly.

The last term in Eqs. (2.11) and (2.12) is the resonance condition. It is a Dirac-delta function which ensures that the n-th harmonic of the electron cyclotron frequency in the phase space spanned by s, $u_\perp$ and $u_\parallel$ matches the measurement frequency ω. For the resonance condition the Doppler shift and the relativistic mass increase are considered. Their implications are discussed in detail in Section 2.4.3. The delta function is eliminated by integrating over either $u_\perp$ or $u_\parallel$. The integral then becomes a path integral in momentum space, which has the shape of a half ellipse. For an example of this curve see Section 2.4.3.

To attain the absorption coefficient α_ω and the emissivity j_ω it is necessary to sum up the contributions of the individual harmonics

$$\alpha_\omega = \sum_{n=1}^{\infty} \alpha_{\omega,n}; \qquad\qquad j_\omega = \sum_{n=1}^{\infty} j_{\omega,n}. \tag{2.14}$$

For the majority of the ASDEX Upgrade discharges the electrons can be approximated to be thermally distributed, which allows the absorption coefficient to be derived from the emissivity via Kirchhoff's law [43] and vice versa:

$$\alpha_\omega(s) = \frac{j_{\omega,n}(s)}{I_{\mathrm{BB},\omega}(s) N_{\omega,\mathrm{ray}}^2} \approx j_{\omega,n}(s) \frac{8\pi^3 c_0^2}{\omega^2 k_\mathrm{b} T_\mathrm{e} N_{\omega,\mathrm{ray}}^2}. \tag{2.15}$$

The Rayleigh-Jeans approximation for $I_{\mathrm{BB},\omega}$ yields the expression given on the right side of Eq. (2.15) [5] and k_b is the Boltzmann constant.

The omission of the sloshing flux and the cold plasma approximation for the refractive index and wave polarization restrict the validity of Eqs. (2.11) and (2.12) to harmonics

with $n > 1$ and $n > 2$, respectively, if $\omega_c \geqslant \omega_p$ [55, 58]. The inability to calculate the emissivity and absorption coefficient for the fundamental harmonic is not an issue for the data analysis at ASDEX Upgrade as measurements of fundamental ECE have not been exploited recently at ASDEX Upgrade. The second condition which applies for the second harmonic could, however, have consequences, as $\omega_c \approx \omega_p$ for most ASDEX Upgrade plasmas. It will be shown in Section 4.2.12 that the performance of Eqs. (2.11) and (2.12) is adequate for the purposes of data analysis even if $\omega \approx \omega_p$. It is found that the absolute values of the emissivity and absorption coefficient can deviate from the corresponding values derived self-consistently from the fully-relativistic dispersion relation by several tens of percent relatively (c.f. Section 5.1.3). However, it was found that the intensity does not depend sensitively on the exact value of the emissivity and the absorption coefficient. Accordingly, the intensity derived with the approximate emissivity and absorption coefficient and the intensity computed from the self-consistently derived absorption coefficients and emissivities do not deviate significantly(c.f. Section 5.1.3).

The emissivity and the absorption coefficient can be separated into three individual contributors as highlighted in Eqs. (2.11) and (2.12). These are the "polarization factor" [55], the distribution function and the (relativistic) resonance condition. Each term is discussed in the following.

2.4.1 The "polarization factor":

The "polarization factor" [55] accounts for the wave polarization and for finite Larmor radius effects. This term can be considered as the absorption strength of a single, resonant electron with momentum $\boldsymbol{u}$. The "polarization factor" is proportional to $\left(\frac{u_\perp}{\gamma}\right)^{2n}$, if the quasi-perpendicular approximation is applied and the Bessel functions are expanded to the lowest order [5]. Hence, the single electron emission increases strongly with increasing momentum. In Section 5.1.4 it will be shown that the emission of few, but highly energetic electrons can contribute significantly to ECE measurements.

In the cold plasma approximation, where kinetic effects are neglected, the dispersion relation can be analytically solved for the refractive index $N_{s,\omega}$ [43]. This also allows the analytic determination of the absolute value of the individual components of the normalized polarization vector $\boldsymbol{e}$ from the wave equation [43].

2.4.2 The electron momentum distribution

The distribution function normalized to unity for a relativistic, thermal plasma is given by the Maxwell-Jüttner distribution [59]

$$f_{\mathrm{MJ}}(u_\perp, u_\parallel) = \frac{\mu}{4\pi}\frac{1}{\mathrm{K}_2(\mu)}\mathrm{e}^{-\mu\gamma}; \qquad f_{\mathrm{MJ}}(\beta) = \frac{\gamma^2\beta\mu}{\mathrm{K}_2(\mu)}\mathrm{e}^{-\mu\gamma}; \qquad \mu = \frac{m_{\mathrm{e},0}c_0^2}{T_\mathrm{e}}. \tag{2.16}$$

The first form is for cylindrical momentum coordinates and the second for spherical velocity coordinates. The modified Bessel function of the second kind also known as the MacDonald function is denoted as $\mathrm{K}_l(\mu)$ with order $l = 2$ and $\beta = \frac{u}{\gamma} = \frac{v}{c_0}$ is the velocity normalized to the speed of light. In the non-relativistic limit, where $\gamma = 1$ and $\boldsymbol{u} = \boldsymbol{\beta}$, the Maxwell-Jüttner distribution becomes the well-known Maxwellian (here in cylindrical, normalized velocity coordinates $\beta = \frac{v}{c_0}$):

$$f_{\mathrm{M}}(\beta) = \beta\sqrt{\frac{2\mu^3}{\pi}}\exp\left(-\mu\frac{\beta^2}{2}\right). \tag{2.17}$$

One could argue that relativistic effects in the distribution function are negligible, because peak T_e observed at ASDEX Upgrade rarely exceed $20\,\mathrm{keV} \ll m_{\mathrm{e},0}c_0^2 \approx 511\,\mathrm{keV}$. But in practice the emission from highly energetic electrons with $E_\mathrm{kin} > 50\,\mathrm{keV}$ can contribute significantly to the observed T_rad (c.f. Section 5.1.4). While already critical for the interpretation of the ECE of high T_e thermal plasmas, the relativistic mass-increase becomes absolutely crucial for the interpretation of ECE of non-thermal plasmas.

2.4.3 Relativistic electron cyclotron resonance

If the relativistic mass-increase and the Doppler shift are taken into account the ECE resonance condition can be written as

$$\gamma - u_\parallel N_\parallel - \frac{n}{\overline{\omega}} = 0. \tag{2.18}$$

Only electrons that fulfill this condition will contribute to the ECE measured at frequency ω. In Fig. 2.2 the normalized abundance of cyclotron frequencies is shown considering (i) the relativistic mass-increase, (ii) the Doppler shift and (iii) their combined effect, for $T_\mathrm{e} = 8\,\mathrm{keV}$ in a) and for $T_\mathrm{e} = 1\,\mathrm{keV}$ in b) assuming an observation angle of $\theta = 80°$ with respect to the magnetic field and a refractive index of $N_{\mathrm{s},\omega} = 1$. The curves shown

in Fig. 2.2 are given by:

$$f\left(\frac{\omega_{\mathrm{c,obs}}}{\omega_{\mathrm{c},0}}\right) = 2\pi \iint u_\perp \mathrm{d}u_\perp \mathrm{d}u_\parallel \delta(\omega_{\mathrm{c,obs}} - \omega_{\mathrm{c},0}) f_{\mathrm{MJ}}(u_\perp, u_\parallel) \tag{2.19}$$

In Eq. (2.19) the observed cyclotron frequency $\omega_{c,\mathrm{obs}}$ was introduced according to the following definitions:

$$\frac{\omega_{\mathrm{c,obs}}}{\omega_{\mathrm{c},0}} \equiv \frac{n}{1 - \frac{u_\parallel}{\gamma} N_\parallel} \qquad \text{for the Doppler shift,} \tag{2.20}$$

$$\frac{\omega_{\mathrm{c,obs}}}{\omega_{\mathrm{c},0}} \equiv \frac{n}{\gamma} \qquad \text{for the relativistic mass-increase, and} \tag{2.21}$$

$$\frac{\omega_{\mathrm{c,obs}}}{\omega_{\mathrm{c},0}} \equiv \frac{n}{\gamma - u_\parallel N_\parallel} \qquad \text{for the combined effect.} \tag{2.22}$$

If only the Doppler effect is considered (dotted dashed lines in Fig. 2.2) the resulting cyclotron spectrum will show a symmetric broadening around the cold cyclotron frequency (dotted line) and the relativistic mass-increase only causes a frequency down-shift (dashed line). In the limit of large $u_\parallel$ the down-shift caused by the relativistic mass increase is larger than the Doppler up-shift. This gives rise to an upper limit for the up-shift if both effects are considered. This limit is marked in Fig. 2.2 by the vertical, dashed red lines and is given by:

$$\max\left(\frac{\omega_{\mathrm{c,obs}}}{\omega_{\mathrm{c},0}}\right) = \frac{n}{\sqrt{1 - N_\parallel^2}} \tag{2.23}$$

At $T_\mathrm{e} = 8\,\mathrm{keV}$ (see Fig. 2.2 a)) the combined spectrum (solid line) is strongly asymmetric and down-shifted frequencies are more abundant than up-shifted ones. For smaller T_e $= 1\,\mathrm{keV}$ (see Fig. 2.2 b)) the Doppler shift is more dominant and a frequency up-shifted is almost as likely as a frequency down-shift.

To understand the ECE it can be important to know how the relativistic resonance condition manifests itself in momentum space. For this purpose it is necessary to

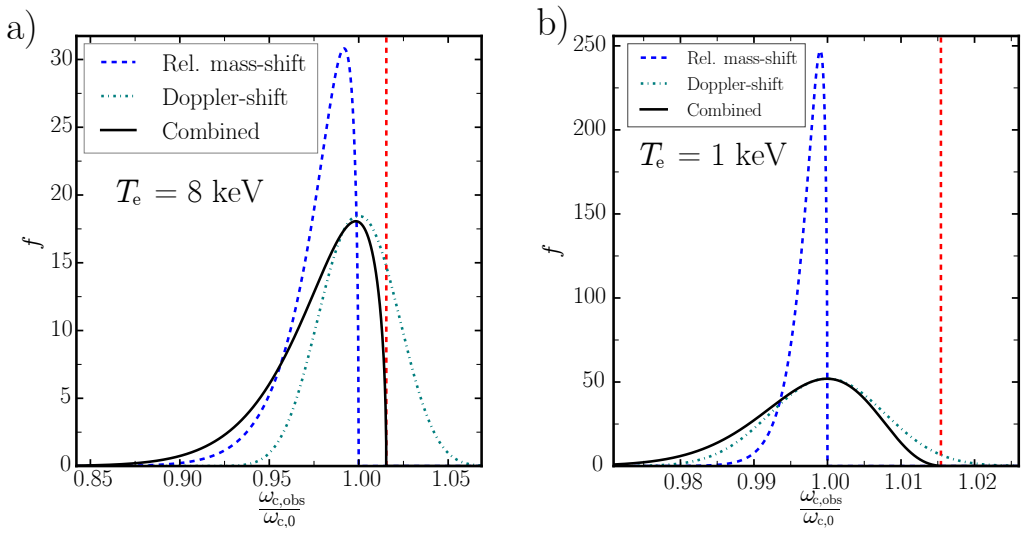

Figure 2.2: Normalized abundance of cyclotron frequencies as a function of the ratio between the observed cyclotron frequency and the (cold) cyclotron frequency for two electron temperatures. For both graphs the angle between $\boldsymbol{B}$ and $\boldsymbol{N}$ is $\theta = 80°$ and the refractive index $N_{s,\omega} = 1$. The red vertical line marks the largest possible up-shift.

express the resonance condition in terms of $u_\perp$ and $u_\parallel$:

$$\begin{aligned} \omega = \omega_{c,obs} &= \frac{n\omega_{c,0}}{\gamma - u_\parallel N_\parallel}, \\ \Leftrightarrow u_\perp(u_\parallel) &= \sqrt{\left(N_\parallel u_\parallel + \frac{n\omega_{c,0}}{\omega}\right)^2 - u_\parallel^2 - 1}. \end{aligned} \tag{2.24}$$

Hence, the resonance condition is fulfilled along a half ellipse in momentum space. Setting the argument of the square root in Eq. (2.24) equal to zero yields the interval in which a real solution for $u_\perp$ exits

$$u_{\parallel,\pm} = \frac{N_\parallel \frac{n\omega_{c,0}}{\omega} \pm \sqrt{N_\parallel^2 + \left(\frac{n\omega_{c,0}}{\omega}\right)^2 - 1}}{1 - N_\parallel^2}. \tag{2.25}$$

In case of perpendicular propagation, where $N_\parallel = 0$, the resonance line becomes a half circle with radius $\sqrt{\left(\frac{n\omega_{c,0}}{\omega}\right)^2 - 1}$. For $N_\parallel \neq 0$ the resonance ellipse is displaced from the $u_\parallel = 0$ axis.

Figure 2.3 shows two resonance curves for the second harmonic and $\frac{\omega_{c,obs}}{2\omega_{c,0}} = 1.33$.

As expected the resonance line corresponding to perpendicular propagation (blue solid line in Fig. 2.3) is centered around $u_\parallel = 0$. Given an $N_\parallel = 0.7$ the resonance curve (green dashed line) is shifted towards positive $u_\parallel$ and the curvature radius is much increased. Hence, changing $N_\parallel$ changes the region of momentum space that contributes to the observed ECE making oblique LOS highly attractive for the measurement of non-thermal electron momentum distribution functions.

It should be noted that the resonance of a wave in phase space is never truly just a line. Due to the uncertainty principle either the beam or the $N_\parallel$ spectrum have finite widths. This means that $N_\parallel$ and ω_c are not singular values in Eq. (2.24), but rather distributions. Furthermore, if the beam is not monochromatic also ω follows a certain distribution. Accordingly, the resonance in momentum space is a two-dimensional distribution function. In this work we limit ourselves to the path of the central ray and a singe $N_\parallel$. For ω always the central frequency is assumed in all plots showing resonance curves.

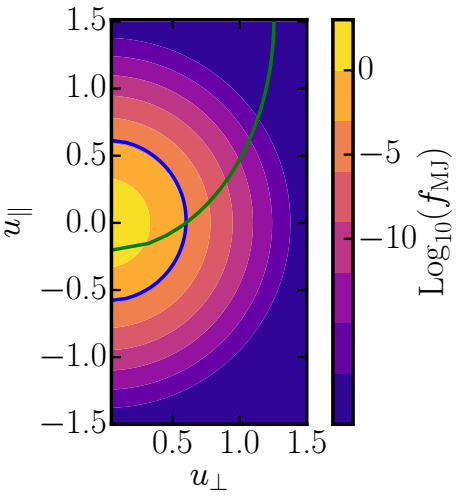

Figure 2.3: Two resonance lines are shown for the second harmonic and $\frac{\omega_{c,obs}}{2\omega_{c,0}} = 1.17$. The blue line corresponds to $N_\parallel = 0.0$ and the green line to $N_\parallel = 0.7$. The contours of the Maxwell-Jüttner distribution for $T_e = 8\,\mathrm{keV}$ are shown in the background.

2.5 The birthplace distribution of observed intensity

In classical ECE analysis each measurement frequency is mapped to its cold resonance position. Hence, there is a one-to-one correspondence between frequency and position. If broadening effects are to be considered in the analysis, this one-to-one relation is no longer applicable. Instead, for each measurement there is a distribution of measurement positions. This distribution will be referred to as the birthplace distribution of observed intensity in this work. It is defined by

$$D_\omega(s) = \frac{j_\omega(s) T_\omega(s)}{I_\omega(s_{ow})}, \tag{2.26}$$

where $T_\omega(s)$ is the transmittance of the plasma for waves at frequency ω along the ray path from point s to the observation point s_{ow}:

$$T_\omega(s) = \mathrm{e}^{-\tau_\omega(s)} = \exp\left(-\int_s^{s_{\mathrm{ow}}} \alpha_\omega(s')\mathrm{d}s'\right) \tag{2.27}$$

Functions similar to the birthplace distribution of observed intensity, although not normalized, have been used in various studies (see e.g. Ref. [60]). The were also used to compute "warm resonances" [60], for which the birthplace distribution is reduced to a singular point that includes any radial shift. This function has several names in the literature, e.g. "total emissivity" [61], "actual emission" [11] or "emitting profile" [62]. We propose our own wording here which does not allow any possible confusion of the birthplace distribution with the emissivity.

To obtain the birthplace distribution the integral representation of the radiative transport equation (2.9) is required, where the boundaries are given by the start and end points of the ray path (i.e. inner wall s_{iw} and outer wall s_{ow} for straight LOS):

$$I_\omega(s_{\mathrm{ow}}) = \int_{s_{\mathrm{iw}}}^{s_{\mathrm{ow}}} j_\omega(s) T_\omega(s)\mathrm{d}s \tag{2.28}$$

Normalizing the argument of the integral in Eq. (2.28) by the observed intensity $I_\omega(s_{\mathrm{ow}})$ yields the birthplace distribution of observed intensity (see Eq. (2.26)). If expressed as a function of the normalized minor radius ρ_{pol} it is the ECE equivalent to the power deposition profile used in ECRH studies (c.f. Fig. 2.4).

In the case of strong absorption near the cold resonance position, the birthplace distribution shows a narrow peak and all of the observed radiation is emitted by a thin layer of plasma near the cold resonance position. Accordingly, T_{rad} is approximately equal to T_{e} at the cold resonance position. All quantities relevant to the radiation transport are illustrated in Fig. 2.5 for such a scenario. In a) the intensity I_ω (black solid line), the black body intensity $I_{\mathrm{BB},\omega}$ (black-dashed line), and the emissivity j_ω (blue solid line) as functions of the normalized minor radius ρ_{pol}. In Fig. 2.5 b) the absorption coefficient α_ω (red line) and the transmittance T_ω (dashed black line) are visualized. The shape of D_ω is given by the product of emissivity j_ω and transmittance T_ω and is plotted in Fig. 2.4. Although the emissivity is non-zero for a large region, only a thin layer of

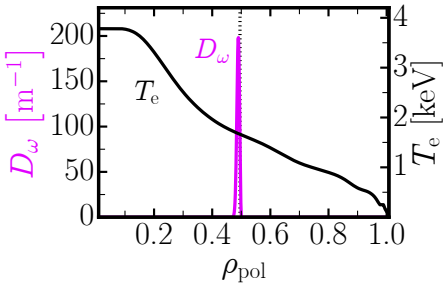

Figure 2.4: An example for a birthplace distribution. It has a narrow peak close to the cold resonance and is zero elsewhere.

the plasma contributes to the observed radiation, as the transmittance T_ω has a shape close to a step function around the cold resonance.

As expected, the birthplace distribution in Fig. 2.4 is strongly peaked near the cold resonance position (dashed vertical line), meaning that all the observed radiation originates indeed from a thin layer of plasma near the cold resonance position. It should be noted that for the ASDEX Upgrade ECE diagnostics there is always a small amount of up-shifted radiation caused by the Doppler shift [11]. This can be seen in Fig. 2.4 by the small part of the birthplace distribution that extends across the cold resonance towards the right, where the antenna is located. The birthplace distribution will be one of the main tools to understand various ECE measurements of thermal plasmas which will be discussed in Chapter 5.

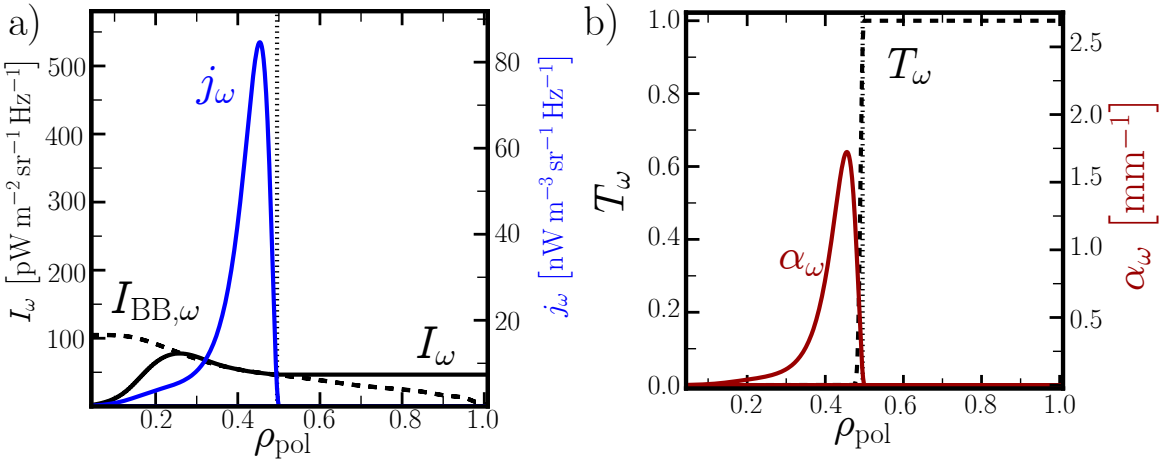

Figure 2.5: Key quantities of the radiation transport are displayed as function of ρ_{pol} for a plasma scenario and measured frequency where classical ECE analysis is applicable. The cold resonance position is indicated by the dotted vertical line. In a) the intensity I_ω, the emissivity j_ω and the black body intensity $I_{\mathrm{BB},\omega}$ are shown. Figure b) depicts the absorption coefficient α_ω and the transmittance T_ω.

To better understand ECE spectra from non-thermal electron momentum distributions, which can be anisotropic, it can be useful to extend the Birthplace distribution to the phase space spanned by a spatial coordinate and the momentum parallel and perpendicular to the magnetic field. The spatial coordinate can be flexibly chosen. In the following the major radius is the radial coordinate of choice. For the ensuing introduction to the 2D-birthplace distribution only thermal distributions are considered for simplicity's sake. The two-dimensional birthplace distribution is given by (c.f.

Eq. (2.11))

$$D_\omega(\rho_{\mathrm{pol}}, u_\parallel) = \frac{T_\omega(s)}{I_\omega}\frac{{\omega_{\mathrm{p},0}}^2\omega}{2\pi c_0^3}\int\left(\frac{n}{\bar{\omega}N_\perp}\right)^2\left|\left(e_x + \frac{\bar{\omega}N_\perp}{n}u_\parallel e_z\right)J_n(b) - \frac{ib}{n}J_n'(b)e_y\right|^2 \times f(s, u_\perp, u_\parallel)\delta\left(\gamma - u_\parallel N_\parallel - \frac{n}{\bar{\omega}}\right)\frac{u_\perp}{\gamma}\mathrm{d}u_\perp. \tag{2.29}$$

Its sole distinction from the one dimensional birthplace distribution is that the integration over $u_\parallel$ in the emissivity is omitted. An example for a two dimensional birthplace distribution of an oblique ECE diagnostic is shown in Fig. 2.6 using two different graphical representations. In a) the values of $u_\perp$ are indicated by color coded contour areas. The magnitude of the The birthplace distribution of observed intensity is signified by colored contour lines. The yellow-green-blue color pattern corresponds to $u_\perp$ and the black-purple-red-yellow color map to the magnitude of the birthplace distribution. In figure b) a three-dimensional illustration of the birthplace distribution is shown. The coloration indicates how strongly the individual points on the surface contribute. Both graphs only represent the birthplace distribution for the central ray of the volume of sight (VOS) with a singular frequency.

Similarly to the birthplace distribution of observed intensity the power deposition profile of ECRH also has a phase space representation. Again this requires the restriction to a single ray and frequency. In this case the power deposition profile can be written as

$$\frac{\mathrm{d}P_\omega}{\mathrm{d}s} = \alpha_\omega(s)P_0\mathrm{Exp}\left[-\int_{s_0}^{s_1}\alpha_\omega(s')\mathrm{d}s'\right], \tag{2.30}$$

where the ray enters the plasma at s_0 with a power of P_0 and leaves it at s_1. The extension to two dimensions follows completely analogous to the two-dimensional birthplace distribution. The α_ω, which is not part of the integral in Eq. (2.30) has to be replaced with its momentum space dependent variant (c.f. the integral in Eq. (2.12)). An example for the two-dimensional power deposition profile of an ECCD beam is shown in Fig. 2.7 using the same two illustration techniques as in Fig. 2.6.

When comparing Fig. 2.6 and Fig. 2.7 it seems that the two functions are very similar, but neither of the two representation allows a truly quantitative comparison. To check the phase space alignment of an ECE diagnostic and the ECRH, it is more convenient to separate the radial dependence of the birthplace distribution and the power deposition profile from the momentum space dependence. An example of how this can be achieved is illustrated in Fig. 2.8. In a) the radial dependence of the birthplace distribution and the power deposition are compared and it can be seen that they overlap almost entirely. In Fig. 2.8 b) the color coded resonance lines of the ECRH and the ECE diagnostic are shown for three radial positions each, which are indicated in Fig. 2.8 a) by the

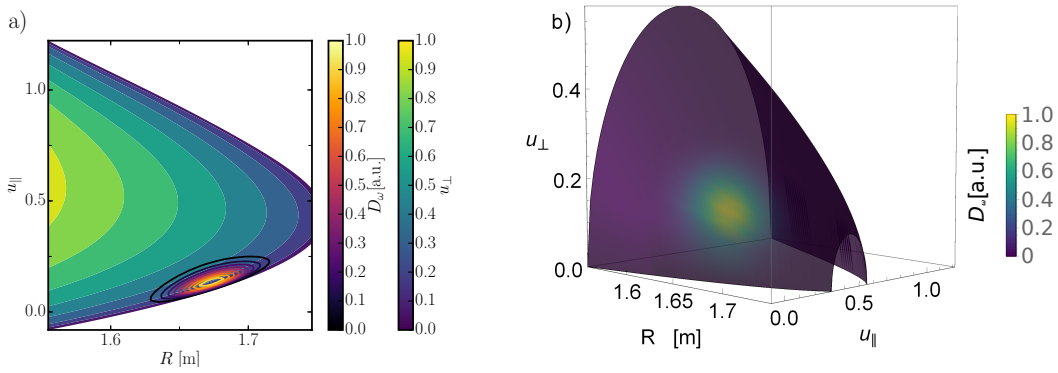

Figure 2.6: The resonance surface is plotted in phase space. a) The value of $u_\perp$ is indicated by the blue-green-yellow contour areas. The magnitude of the 2D-birthplace distribution is indicated by the black-purple-red-yellow contour lines. b) Three dimensional representation of the 2D-birthplace distribution. The coloration of the surface indicates the magnitude of the birthplace distribution.

vertical lines. The dotted vertical lines correspond to the ECE, and the dash-dotted, vertical lines to the ECRH. The size of the resonance curve decreases with increasing major radius. Additional to the resonance lines in Fig. 2.8 b) shows the contour lines (black) of the thermal distribution function at the radial position, where the birthplace distribution in Fig. 2.8 a) has its maximum.

2.6 Steady state non-thermal distribution functions

One of the unique features of the plasma phase state is that the collision frequency ν of a particle traveling with velocity v decays, at large speeds, with $\nu \propto \frac{1}{v^3}$. Consequently, the relaxation times of highly energetic particles can be quite large and many processes can lead to non-thermal distribution functions. One of the main topics of this thesis is the measurement of the electron distribution functions with ECE during highly intense ECCD. In this section non-linear electron cyclotron damping and quasi-linear theory are introduced. The importance of the parallel electric field, radial transport and the radiation reaction force are also addressed briefly.

2.6.1 Electron cyclotron damping

Electron cyclotron damping is in many aspects similar to Landau damping, which is discussed by most text books on plasma physics (e.g. [4]). The fundamental difference between the two processes lies in the resonant interaction between particle and wave. Landau damping describes the resonant interaction between particles and electrostatic

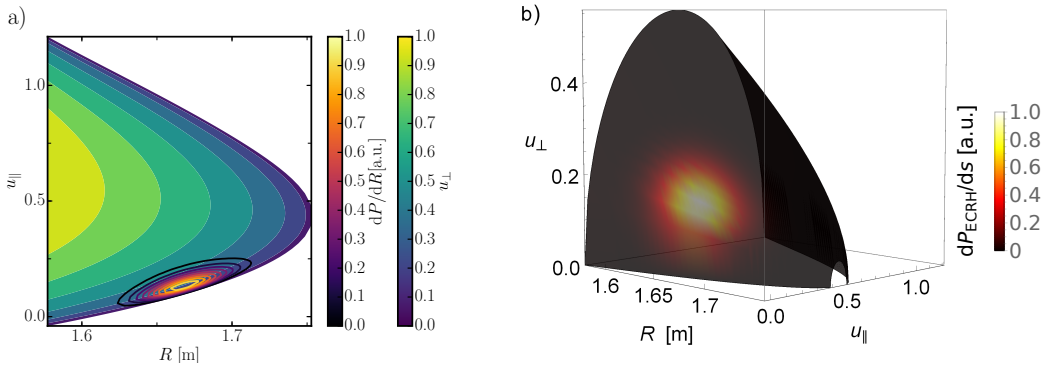

Figure 2.7: a) Power deposition profile of the ECRH in phase space. The plotting scheme is identical to Fig. 2.6 a). b) As Fig. 2.6 b) but here power deposition profile in phase space is plotted. The different color coding is chosen to better differentiate between ECRH and ECE.

waves which have phase velocities smaller than the speed of light. The resonance occurs if the speed of a particle parallel to the wave vector approaches the phase velocity of the wave. For electron cyclotron waves the refractive index of the plasma is usually smaller than one. Consequently, the phase velocity of electron cyclotron waves is superluminous and Landau damping is impossible. In case of cyclotron damping the wave resonates with the cyclotron motion of the particle, possibly, Doppler shifted if the wave vector is not parallel to the ambient magnetic field. The resulting resonance condition was discussed in detail in Section 2.4.3.

For electron cyclotron damping in fusion plasmas it is, in most cases, valid to approximate that the trajectory and gryo phase of the electron remain unperturbed by the energy transfer between wave and particle. This assumption allows the linearization of the Vlasov equation which describes the damping process. A detailed description of the linearized interaction of a single electron with an electromagnetic wave can be found in Refs. [63, 64]. To explain the long term, average effect of electron cyclotron waves on the distribution of the electrons three properties of the single particle picture are relevant:

1. For a finite time window Δt particles can interact with the wave even if they do not fulfill the resonance condition exactly. The Dirac-Delta like behavior is only reproduced in the limit of $\Delta t \to \infty$[65].

2. The strength of the interaction between particle and wave increases the closer the particle is to the resonance.

3. A particle can be either accelerated or decelerated by the wave depending on the phase-shift $\Delta\phi$ between the gyrophase of the particle and the phase of the

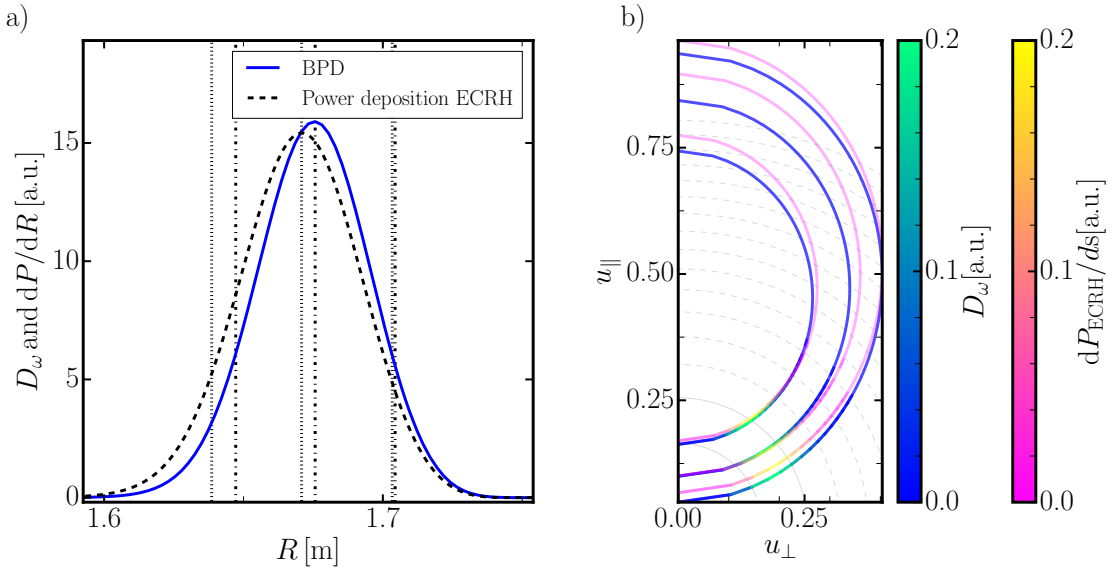

Figure 2.8: a) Power deposition profile of an ECCD beam and the birthplace distribution for the oblique ECE are drawn as functions of the major radius. b) Color coded resonance lines (blue to green color map) are shown for each of the radial positions indicated in a) by the vertical lines. Dotted, vertical lines correspond to the blue-to-green color coded resonance curves of the ECE. The radial positions of resonance lines of the ECRH, color coded in b) by a pink-to-yellow color scheme, are indicated in a) by the dashed-dotted vertical lines in a).

electron cyclotron wave. The energy transfer function is symmetric in $\Delta\phi$, i.e. there are as many $\Delta\phi$ that lead to acceleration of the particle as there are $\Delta\phi$ that cause the particle to be decelerated.

Generally it is a good assumption that $\Delta\phi$ is uniformly distributed. This can be either due to collisions or the intrinsic stochasticity of non-linear systems, like the dynamics of a fusion plasma (see Ref. [66]). The uniform distribution of $\Delta\phi$ could lead to the conclusion that on average the energy transfer between wave and particle is zero, but this is not the case.

For the following discussion it is useful to neglect the Doppler effect and introduce $\delta \equiv \omega - \frac{\omega_{c,0}}{\gamma}$ which quantifies how close the particle is to the resonance. Particles with velocities for which $\delta < 0$ move too slow to fulfill the resonance condition and are, henceforth, referred to as "slow" particles. "Fast" particles are defined analogously. A infinitesimally small increase of the velocity moves "slow" particles closer to the resonance and "fast" particles further away. The opposite applies for a decrease of the velocity. This means that "slow" particles tend to get accelerated by the wave while "fast" particles are decelerated.

Clearly, the total energy transfer rate $\frac{\mathrm{d}E}{\mathrm{d}t}$ between the particles and the wave depends on the ratio between the amount of "slow" and "fast" particles or, more precisely, on $\frac{\mathrm{d}E}{\mathrm{d}t} \propto \frac{\mathrm{d}f}{\mathrm{d}v}$. If there are initially as many "fast" particles as there are "slow" particles, i.e. $\frac{\mathrm{d}f}{\mathrm{d}v}\Big|_{v=v_{\mathrm{res}}} = 0$, then there is indeed no energy transferred between the electrons and the wave. But for thermal electrons $\frac{\mathrm{d}f}{\mathrm{d}v}$ is always negative and more of the "slow" particles are accelerated than "fast" particles are decelerated and because of energy conservation the intensity of the wave decreases. This results in a local flattening of the distribution function around the resonance. When the distribution function is completely flat at the resonance, linear electron cyclotron damping seizes. Because of this linear ECRH damping cannot cause a bump-on-tail distribution as indicated by the red curve in Fig. 2.9. In this case the wave decelerates more particles than it accelerates and the intensity of the wave increases and one speaks of inverse damping.

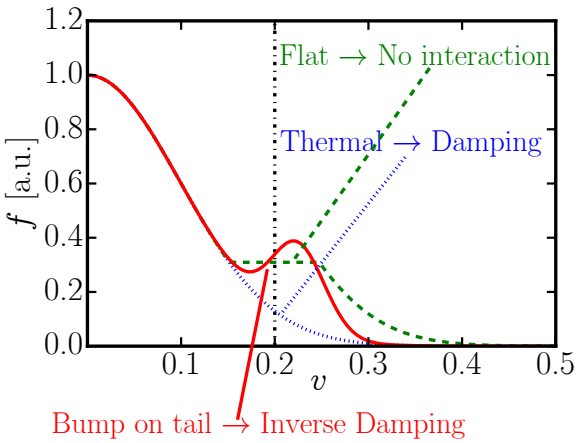

Figure 2.9: Depending on the gradient of the distribution at the resonance the wave is either damped or inversely damped. If the distribution is flat at the resonance then there is no wave-particle interaction.

2.6.2 Quasi-linear theory and bounce averaging

In the previous section collisions had no effect on the distribution function besides randomizing the gyrophase. To attain the steady-state distribution function it is essential to also consider the momentum and energy transfer due to collisions. Here one has to distinguish between the collisions in between electrons and electron-ion collisions. In fusions plasmas collisions are predominately small angle scattering events [4], allowing them to be approximated with the Fokker-Planck collision operator (see e.g. Ref. [67]). The general Fokker-Planck equation for the electrons reads [67]

$$\frac{\partial f_{\mathrm{e}}}{\partial t} + \boldsymbol{v} \cdot \boldsymbol{\nabla} f_{\mathrm{e}} - e\left(\boldsymbol{E} + \frac{\boldsymbol{v}}{c_0} \times \boldsymbol{B}\right) \cdot \boldsymbol{\nabla}_{\boldsymbol{p}} f_{\mathrm{e}} = \sum_s C(f_{\mathrm{e}}, f_{\mathrm{s}}). \tag{2.31}$$

with f_{e} the electron distribution function and f_{i} the distribution function of the ions. The Fokker-Planck collision operator between the electrons and species s is denoted as $C(f_{\mathrm{e}}, f_{\mathrm{s}})$. The electric field $\boldsymbol{E}$ and the magnetic field $\boldsymbol{B}$ include the ambient, static fields and the fluctuating components due to the ECRH waves. Numerically, this poses

a problem. To resolve the electric and magnetic field of the ECRH wave temporally, the time step has to be smaller than $\frac{1}{f_{\mathrm{ECRH}}} \approx 10\,\mathrm{ps}$. To properly model the effect of collisions the total simulation time has to be of the order of ms. Accordingly, with the current Fokker-Planck equation it would be required to have billions of time steps.

For this thesis only the steady state distributions during ECRH are of interest and, hence, it is much more effective to include only the average effect of the fast fluctuating fields on the distribution function. This can be accomplished by separating the electric and the magnetic fields into quickly $\tilde{\boldsymbol{E}}, \tilde{\boldsymbol{B}}$ and slowly varying $\hat{\boldsymbol{E}} = \langle \boldsymbol{E} \rangle_t \,, \hat{\boldsymbol{B}} = \langle \boldsymbol{B} \rangle_t$ components. The Fokker-Planck equation for the slowly varying distribution $\hat{f}$ can then be written as [67]

$$\frac{\partial \hat{f}_{\mathrm{e}}}{\partial t} + \boldsymbol{v} \cdot \boldsymbol{\nabla} \hat{f}_{\mathrm{e}} - e \left(\hat{\boldsymbol{E}} + \frac{\boldsymbol{v}}{c_0} \times \hat{\boldsymbol{B}} \right) \cdot \boldsymbol{\nabla}_{\boldsymbol{p}} \hat{f}_{\mathrm{e}} = -\boldsymbol{\nabla}_{\boldsymbol{p}} \cdot \left(\langle \boldsymbol{\Gamma}_{\mathrm{c}} \rangle + \left\langle \boldsymbol{\Gamma}_{\mathrm{ql}} \right\rangle \right), \tag{2.32}$$

with $\langle \dots \rangle$ indicating an averaging process over fast time scales as indicated below. $\boldsymbol{\Gamma}_{\mathrm{c}}$ is the flux due to collisions and $\boldsymbol{\Gamma}_{\mathrm{ql}}$ is the quasi-linear flux caused by the fluctuating components of the electric and magnetic fields [67]

$$\boldsymbol{\Gamma}_{\mathrm{ql}} = -e \left(\tilde{\boldsymbol{E}} + \frac{\boldsymbol{v}}{c_0} \times \tilde{\boldsymbol{B}} \right) \cdot \boldsymbol{\nabla}_{\boldsymbol{p}} \tilde{f}_{\mathrm{e}}. \tag{2.33}$$

A formal solution for $\tilde{f}_{\mathrm{e}}$ can be gained from the linearized Vlasov equation:

$$\frac{\mathrm{d}\tilde{f}_{\mathrm{e}}}{\mathrm{d}t} = \frac{\partial \tilde{f}_{\mathrm{e}}}{\partial t} + \boldsymbol{v} \cdot \boldsymbol{\nabla} \tilde{f}_{\mathrm{e}} - e \left(\hat{\boldsymbol{E}} + \frac{\boldsymbol{v}}{c_0} \times \hat{\boldsymbol{B}} \right) \cdot \boldsymbol{\nabla}_{\boldsymbol{p}} \tilde{f}_{\mathrm{e}} = e \left(\tilde{\boldsymbol{E}} + \frac{\boldsymbol{v}}{c_0} \times \tilde{\boldsymbol{B}} \right) \cdot \boldsymbol{\nabla}_{\boldsymbol{p}} \hat{f}_{\mathrm{e}} \tag{2.34}$$

by integrating along the unperturbed electron trajectories [68]

$$\tilde{f}_{\mathrm{e}}(t) = \int_{-\infty}^{t} e \left(\tilde{\boldsymbol{E}} + \frac{\boldsymbol{v}}{c_0} \times \tilde{\boldsymbol{B}} \right) \cdot \boldsymbol{\nabla}_{\boldsymbol{p}} \hat{f}_{\mathrm{e}} \mathrm{d}t'. \tag{2.35}$$

To attain the steady state electron distribution function during ECRH it is possible to average the fluxes (quasi-linear and collisional) needed for Eq. (2.32) over the gyro orbits and the bounce orbits of the electrons. The $\langle \dots \rangle_t$ in Eq. (2.32) becomes a double average and Eq. (2.32) is called the *bounce-averaged Fokker-Planck equation*. The details of averaging process are not relevant for the present work and the interested reader is referred to [67, 68] for the details. With the bounce averaged Fokker-Planck equation it was shown that in general ECRH does not create significantly non-thermal electron distribution functions, but this can change at low n_{e} and high power densities [69].

2.6.3 Loop voltage

In order to drive the plasma current a loop voltage is induced in the tokamak by a transformer at the center of the torus. The vast majority of this current is carried by the electrons. Under most circumstances this leads to a slight deformation of the distribution function a low electron energies and the generation a tail of highly energetic electrons. The parallel electric field can be introduced into the Fokker-Planck equation as an additional flux [68]. Including this flux into the calculation can be important, because the parallel electric field can interact non-linearly with ECCD.

2.6.4 Radial transport

In the bounce averaged Fokker-Planck equation all flux surfaces are treated independently and the energy and particle transport between flux surfaces is neglected. It has been shown that radial transport should not be neglected when obtaining the steady state distribution function during ECCD [7]. Currently it is not feasible to model the radial transport rigorously since this is only possible if the bounce average is omitted. In this case turbulent effects in the plasma can be treated but this comes at very high computational cost [70].

A much less rigorous, but also much computationally cheaper approach, is to couple the Fokker-Planck equation to a radial diffusion equation. The diffusion coefficients can be obtained from gyrokinetic calculations [39], but due to their large cost this is not performed routinely. Hence, in this work the assumed radial diffusion coefficients are purely empirical (see Section 6.5).

2.6.5 Radiation reaction force

For electrons with large perpendicular momenta collisions are weak while the energy loss due to the ECE can become considerable. It is, therefore, possible that the ECE becomes important in the determination of the steady-state distribution function at high energies (see [71] and [43] and references therein). To discuss this it is helpful to distinguish between the ECE caused by low harmonics ($n \leq 3$ for current devices) and the ECE due to high harmonics ($n > 3$). For low harmonics the optical depth of the plasma is high. Accordingly, the ECE is black body emission and only leads to comparatively small amounts of energy loss of the plasma. Nevertheless, inside the plasma low harmonic ECE is a form of non-local energy transport, which can have a critical influence on the shape of the T_e profile [72]. For the ECE of high harmonics the optical depth of the plasma is low and the ECE is not reabsorbed. Hence, the ECE of high harmonics is a direct energy loss mechanism for magnetically confined fusion

plasmas [55].

To include the influence of ECE in the computation of the steady-state distribution function it is of course necessary to compute the gyro- and bounce-orbit averaged flux $\langle\langle\Gamma_{\mathrm{ECE}}\rangle_{t_{\mathrm{gyro}}}\rangle_{t_{\mathrm{bounce}}}$. Since reabsorption is important for the ECE of low harmonics the corresponding flux is quite cumbersome to obtain. But the ECE of low harmonics is only relevant for total radiated power of a gyrating electron if $v \ll c_0$ where it is expected that $\langle\langle\Gamma_{\mathrm{ECE}}\rangle_{t_{\mathrm{gyro}}}\rangle_{t_{\mathrm{bounce}}} \ll \langle\langle\Gamma_{\mathrm{c}}\rangle_{t_{\mathrm{gyro}}}\rangle_{t_{\mathrm{bounce}}}$[43]. For large electron velocities, where $\langle\langle\Gamma_{\mathrm{ECE}}\rangle_{t_{\mathrm{gyro}}}\rangle_{t_{\mathrm{bounce}}}$ is expected to become non-negligible, most of the radiated power is due to high harmonics [55] and reabsorption becomes negligible. Further simplifications can be made by assuming $v \approx c$, where the, quite intricate, expressions for the radiation drag due to ECE reduces to the Abraham-Lorentz force [73, 74].

The flux due to the Abraham-Lorentz force is [57]

$$\Gamma_{\mathrm{ECE}} = \nabla_{\boldsymbol{u}} \cdot \left(f \left\langle \frac{\partial \boldsymbol{u}}{\partial t} \right\rangle \right) = \nabla_{\boldsymbol{u}} \cdot \left(f \frac{\partial \boldsymbol{u}}{\partial u} \left\langle \frac{\partial u}{\partial t} \right\rangle + f \frac{\partial \boldsymbol{u}}{\partial \zeta} \left\langle \frac{\partial \zeta}{\partial t} \right\rangle \right), \tag{2.36}$$

with $\boldsymbol{u} = \frac{\boldsymbol{p}}{m_{\mathrm{e},0} c_0^2}$, the total momentum $u = |\boldsymbol{u}|$ and the pitch angle $\zeta = \frac{u_\parallel}{u}$. If the magnetic field curvature is neglected then:

$$\left\langle \frac{\partial u}{\partial t} \right\rangle = -u\gamma \frac{1-\zeta^2}{\tau_{\mathrm{r}}} \qquad \left\langle \frac{\partial u}{\partial \zeta} \right\rangle = -\zeta \frac{1-\zeta^2}{\tau_{\mathrm{r}}\gamma} \qquad \tau_{\mathrm{r}} = \frac{6\pi\epsilon_0 m_{\mathrm{e},0}^3 c_0}{e^4 B^2} \tag{2.37}$$

The importance of the Abraham-Lorentz force for ECE will be included in the analysis of ECE measurements of strongly non-thermal distribution functions during ECCD. Furthermore, it will be demonstrated in Chapter 5 that the Abraham-Lorentz force can be neglected in the routine analysis of the ECE spectra at ASDEX Upgrade. To estimate the significance of the radiation reaction force on ECE measurements the linear solution for the steady-state electron distribution function resulting from the Abraham Lorentz force [75, 76] and relativistic collisions [77] was calculated analytically assuming a homogeneous plasma and $u = \gamma\beta \approx 1$. The details on the calculation can be found in the appendix of [57]. The resulting steady state distribution

$$f = f_{\mathrm{MJ}}(u) \left(1 + \sum_{n=0}^{\infty} g_n(u) P_n(\zeta) \right), \tag{2.38}$$

is expressed as a sum of Legendre polynomials P_n. The coefficients of the Legendre polynomials g_n are given by:

$$g_0 = -\alpha \left(\arctan(u) - u + \frac{u^3}{3} \right) \tag{2.39}$$

$$g_2 = \alpha \left(\frac{\gamma+1}{u}\right)^{3(Z_{\mathrm{eff}}+1)} \int_0^u \frac{u'^4}{\gamma'^2} \left(\frac{u'}{\gamma'+1}\right)^{3(Z_{\mathrm{eff}}+1)} \mathrm{d}u' \tag{2.40}$$

The variable α is defined as $\alpha \equiv \frac{2\mu\tau}{3\tau_{\mathrm{r}}}$ and Z_{eff} is the effective ion charge. It can be shown that all other coefficients (g_1, $g_{n>2}$) are zero. Note that the distribution function given by Eq. (2.38) has to be multiplied by a factor to ensure normalization. However, the normalization factor differs only very slightly from one, because only $f_0 g_0$, which is of the order of 1.0×10^{-5}, contributes to the normalization.

3 Experimental Setup

This section discusses the experimental framework of this thesis. First the tokamak ASDEX Upgrade and its heating systems are introduced. Afterwards the diagnostic techniques employed in this thesis are presented with a special emphasis on the ECE. A part of this work was the design of experiments optimal for the study of fast electron generation with ECRH. The key features of these experiments are discussed at the end of this chapter.

3.1 ASDEX Upgrade and its heating systems

3.1.1 ASDEX Upgrade

ASDEX Upgrade with its major radius of 1.65 m and a plasma height of about 2 m [78] belongs to the category of medium-sized tokamaks. It supports a maximum on axis toroidal magnetic field strength of 3.1 T and a maximum plasma current of 1.2 MA [78]. Typical plasma discharges do not last longer than ten seconds. One of the main distinguishing features of ASDEX Upgrade is that all plasma facing components are made of tungsten [79], which is also the material that will be used for the divertor in International Thermonuclear Experimental Reactor [80]. A typical poloidal cross section of ASDEX Upgrade and the contours of constant poloidal flux are shown in Fig. 3.1. This discharge uses the Upper Single Null (USN) configuration where the X-point is above the plasma. The usual configuration is Lower Single Null (LSN), where the magnetic X-point lies at the bottom, but all scenarios discussed in this thesis use the USN configuration.

3.1.2 Neutral beam injection

One method to heat a plasma is the injection of highly energetic particles. Because of the magnetic field it is not possible to inject ions, as they would be deflected by the magnetic field before they can transfer their energy to the plasma. Hence, the ions are neutralized prior to the injection into the plasma. The Neutral Beam Injection (NBI) heating system at ASDEX Upgrade is capable of delivering a total power of 20 MW [78]. The system consists of two beam boxes with four ion sources each. The acceleration

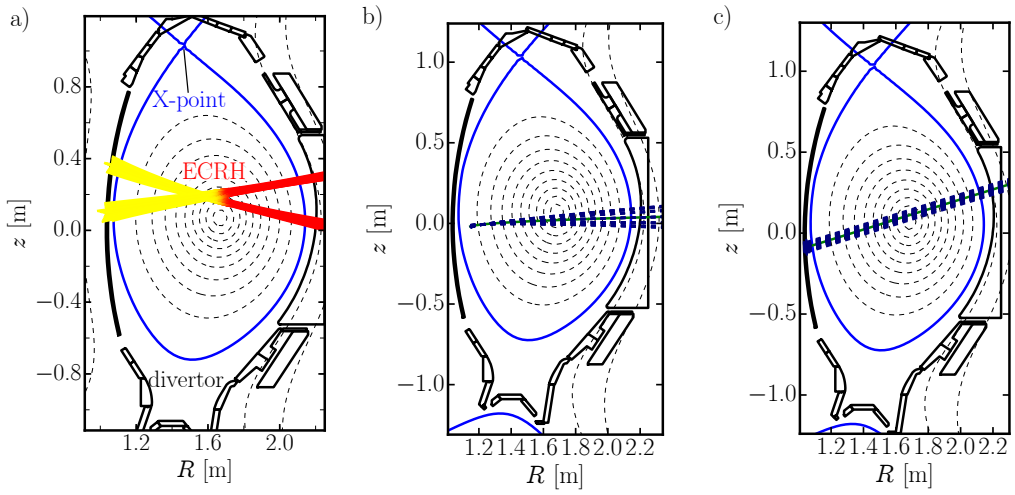

Figure 3.1: Poloidal cross section of ASDEX Upgrade including the flux surfaces from discharge # 34663 and $t = 3.60\,\mathrm{s}$. a) The trajectory of two ECRH beams and the power content of the beam is indicated. Red means the individual ray is at its initial power. Yellow means no power is left. Figure b) shows the volume of sight of the profile radiometer and c) an example viewing geometries of the oblique ECE.

voltage of the beam boxes can be adjusted in the range from 30 kV to 60 kV for one and 50 kV to 93 kV for the other box. This allows the control of the injected power per NBI source. For this thesis NBI was used to vary T_e in experiments.

3.1.3 Wave heating

The plasma can be heated by the injection of powerful electromagnetic waves. Either waves in the range of the electron-cyclotron- or the ion cyclotron frequency are used, leading to electron- and ion cyclotron resonance heating (ICRH), respectively. At ASDEX Upgrade both systems are available. For this work ECRH is of special significance. The main advantage of ECRH over all other heating methods is its capability to deliver its power to a very precise location in the plasma. In Fig. 3.2 the power deposition of ECRH is compared to the power deposition of NBI, ion cyclotron resonance heating (ICRH) and the Ohmic heating for discharge # 29783 at $t = 4.5\,\mathrm{s}$. All four profiles were normalized to one. For reference, the T_e profile is indicated in Fig. 3.2.

The microwaves necessary for ECRH are created with gyrotrons. The ASDEX Upgrade ECRH system is currently being upgraded to have a total of eight dual frequency gyrotrons capable of delivering in between 800 kW to 1000 kW each for a duration of ten seconds [81] and either 140 or 105 GHz.

Each of the gyrotrons has an individual set of mirrors that allow the precise control over the poloidal and toroidal angle of injection [81, 82]. All eight of the launchers can be steered poloidally during a discharge. The toroidal angle of the launchers can only be altered in between discharges. Two of the launchers are located above the mid plane, four in the mid plane and two below. The beam geometry for two of the launchers is illustrated in Fig. 3.1 a).

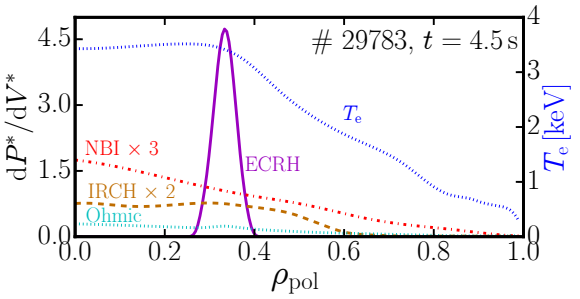

Figure 3.2: Comparison of the normalized power deposition profile of ECRH, ICRH, NBI and Ohmic heating with each other for # 29783 and $t = 4.5\,\mathrm{s}$. The ICRH and NBI power deposition profiles are scaled by a factor of 2 and 3 respectively.

3.2 Diagnostics

This section introduces the diagnostics relevant for this thesis. Of the highest importance are two ECE diagnostics, the absolutely calibrated profile radiometer and the oblique ECE system. Another diagnostic for T_e is Thomson scattering which is also described briefly in this section.

3.2.1 The profile ECE diagnostic

A 60-channel heterodyne radiometer is used for ECE measurements. The antennae of the ECE system view the plasma in the mid-plane and are located on the LFS of the plasma vessel [11, 83, 84]. In Fig. 3.3, the optics of the ECE diagnostic are illustrated. The radiation emitted by the plasma is focused into a rectangular bundle of circular, overmoded wave guides by a quasi-optical system consisting of three lenses. The axis of the quasi-optical system is aligned with the center of the bundle, which is arranged in three rows and four columns. The wave guides are illustrated in Fig. 3.3 by the small rectangles on the left. To avoid cluttering of the figures only the optical paths of two wave guides are shown in each of the figures.

The optical system is shared with an ECE imaging diagnostic using a beam splitter [12]. Since the optical axis is aligned with the center of the wave guide column and there are four columns, none of the LOS of the ECE diagnostic is perfectly radial. For the two inner wave guides the toroidal viewing angle (i.e. the deviation from a perfectly radial view) is $\phi_\mathrm{tor} = \pm 0.7°$ and for the two outer wave guides $\phi_\mathrm{tor} = \pm 2.2°$. The volume of sight inside the torus is indicated in Fig. 3.1 b).

The ASDEX Upgrade profile radiometer is designed to observe the the second

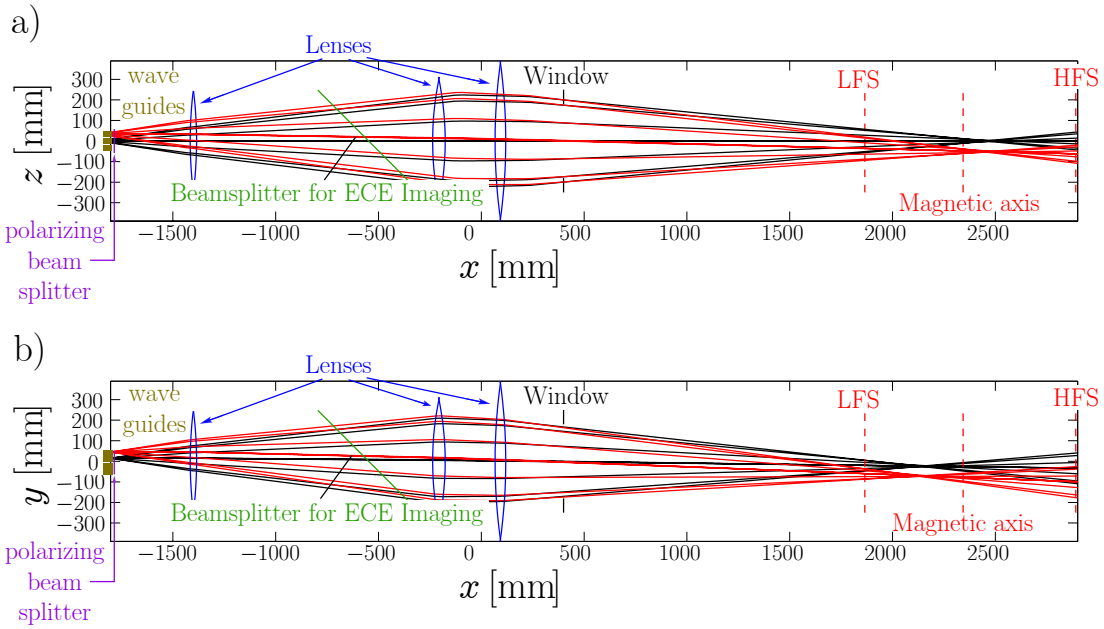

Figure 3.3: The optics system of the profile ECE diagnostic is illustrated as if viewed from the side a) and the top b).

harmonic emission with extraordinary mode (X-mode) polarization. A wire grid polarizer aligned along the toroidal direction reflects the majority of ordinary mode (O-mode) mode polarized radiation. The efficiency of the polarizer is not perfect, which means that a fraction of the measured intensity is actually O-mode emission. How this affects the measurements of thermal plasmas is addressed in Chapter 5 and, for non-thermal plasmas, in Chapter 6.

The radiometer covers a frequency range from 84.3 GHz to 143.6 GHz. For typical magnetic field strengths of ASDEX Upgrade ($|B_t| \approx 2.5\,\mathrm{T}$), the electron cyclotron resonance positions are chosen to cover a few centimeters of the HFS close to the magnetic axis and the entire LFS including the scrape of layer. 36 of the 60 channels feature a bandwidth of 300 MHz in the intermediate frequency, which corresponds to a spatial resolution (disregarding frequency broadening effects) of $\approx 0.5\,\mathrm{cm}$ in the plasma edge. The channels are distributed non-equidistantly with an average spacing of 400 MHz. The other 24 channels have a wider bandwidth of 600 MHz and a frequency spacing of approximately 1 GHz. This translates into a spatial resolution of $\approx 1.2\,\mathrm{cm}$ in the plasma core. The ASDEX Upgrade profile radiometer is calibrated using the hot and a cold source [85] technique and the estimated systematic uncertainty of the calibration is 7 %. The sample rate of the diagnostic is 1 MHz. Measurements of this diagnostic shown throughout this thesis are averaged for 1 ms and the error bars are

composed of the systematic uncertainties and one standard deviation of the combined statistical and systematic uncertainty.

3.2.2 The oblique ECE diagnostic

Oblique ECE measurements are performed with a collective Thomson scattering system [86]. This system uses ECRH wave guides and launchers for the transmission. Since all these components are shared with parts of the ECRH system, measurements with this diagnostic decrease the maximum amount of available gyrotrons. The advantages of this diagnostic are the large flexibility regarding its viewing geometry and its high resolution close to the frequency of the ECRH system. The oblique ECE diagnostic consists of two independent radiometers each connected to one of the ECRH beam lines. The radiometer "CTA" features 50 channels irregularly spaced ranging from 4.4 GHz below the central frequency to 4.5 GHz above it. As central frequency either 105 GHz or 140 GHz can be selected through a wave guide switch, which can be toggled in between discharges. The second radiometer, named "CTC", has 48 individual ECE channels that are spaced slightly narrower around the central frequency than in the "CTA" system. The lowest measured frequency is 3.0 GHz below the central frequency and the highest 3.0 GHz above it. The "CTC" system has only one mixer and the central frequency is 105 GHz. Both diagnostics are sampled at 200 kHz. One of the viewing geometries possible with this diagnostic is illustrated in Fig. 3.1 c).

An adjustable PIN-switch had to be added to the collective Thomson scattering diagnostic to allow the oblique ECE measurements. The switch has two functions. The stray radiation of the gyrotrons is generally a danger for ECE diagnostics. This is especially true for the oblique ECE diagnostic, which has its antenna close to the launchers of the ECRH beams. The ECE spectral intensity of the plasma is in the range of $1\,\mu W/cm^2$ GHz, and the ECRH power per launcher is almost one MW. Usually this danger can be mitigated by a notch-filter which attenuates intensity in the frequency range of the gyrotrons strongly. For collective Thomson scattering it is beneficial for the notch-filter to be as narrow as possible. During switch-on and switch-off gyrotrons exhibit a frequency drift which is not covered by the notch filter. This is compensated by the PIN-switch which closes while the gyrotrons are switched on and off. The switch also allows the attenuation of the diagnostic to be adjusted. This is necessary, because ECE is much more intense than radiation due to collective Thomson scattering.

Additional to the direct influence of stray radiation from the gyrotrons it is also possible for the waves of the gyrotrons to experience a parametric decay [87]. The ECRH wave decays into two sub waves, one with a much lower frequency than the original wave and one with an only slightly lower frequency than the ECRH wave. The wave with the larger frequency falls inside the range of measured frequencies, but

outside the range of the notch-filter. Hence, it enters the radiometer unattenuated. The parametric decay events appear as bursts of radiation in the measured signals and can reach T_{rad} of the order of MeV [87]. They can be powerful enough to potentially damage the diagnostic hardware. These bursts can severely complicate the data analysis of the measurements as they need to be detected and filtered, which is not trivial due to their varying peak height. Empirically, it seems that the parametric decay events are recorded more rarely in case of oblique LOS as oppose to radial views. Nevertheless, known sources of parametric decay events should be avoided.

The diagnostic is not absolutely calibrated and has to be cross-calibrated. Oblique ECE diagnostics are sensitive to up-shifted emission, which inhibits classical ECE analysis of the measurements [88]. Hence, radiation transport modeling is required for the cross-calibration between the absolutely calibrated radial ECE and the oblique ECE. It was observed that the calibration coefficients change if the LOS of the diagnostic is changed drastically. The LOS geometry is unique in every experiment dedicated to the study of ECCD induced non-thermal distribution functions and, therefore, a cross-calibration during each dedicated experiment is necessary. Of, course, for the cross-calibration to succeed it is essential that the distribution function is Maxwellian. Additionally, it is beneficial if T_{e} is varied during the cross-calibration to identify possible systematic errors. A detailed analysis of the cross-calibration can be found in Section 5.4.

The polarization vector of electron cyclotron waves depends on the angle between wave vector and magnetic field θ. Hence, to measure an X-mode ECE spectrum it is necessary to adapt the polarizer of the diagnostic, which consists of two wire grids, according to the currently chosen LOS configuration. The collective Thomson scattering system was optimized for measurements around 105 GHz. Since the efficiency of the polarizers for waves with frequencies around 140 GHz was not clear calculations were performed (courtesy to S.K. Nielsen).They showed that the efficiency of the polarizer is $> 98\,\%$ for all channel, which is sufficient to assume a pure X-mode spectrum in the interpretation of the measurements.

Unless otherwise specified, the measurements shown for this diagnostic are averaged over 1 ms and the error bars indicate one standard deviation of the statistical uncertainty. One standard deviation of the estimated systematic uncertainty due to the cross-calibration is shown for every fifth measurement. It is assumed that the systematic uncertainty of the calibration is the same for all channels.

3.2.3 Thomson scattering

Alternatively to ECE the electron distribution function can be also measured via Thomson scattering [89]. For this technique a short and intense laser pulse is injected

into the plasma. The laser beam scatters off the electrons. Because of the Doppler effect and the relativistic mass increase the frequency of the light is dependent on the speed of the electron it scattered with. Hence, the width of the scattered spectrum contains information on the electron distribution function and, for thermal plasmas, allows the inference of T_e. From the total amount of back scattered light n_e can be determined.

At ASDEX Upgrade the Thomson scattering system consists of a total of ten lasers and two groups of optics. The cross section of the Thomson scattering process is quite small and, accordingly, the lasers used for Thomson scattering have to be quite powerful. This limits the repetition rate of the lasers to 20 Hz. The system is illustrated in Fig. 3.4. The two groups of lasers shoot vertically through the plasma Two lenses guide the scattered light to the polychromators (not depicted) located outside the vessel. Four of the lasers and one of the optics constitute the core Thomson scattering system and the other six lasers and optic are designed for high resolution measurements near the edge of the plasma [90]. The Thomson scattering diagnostic is absolutely calibrated to deliver T_e and n_e profiles.

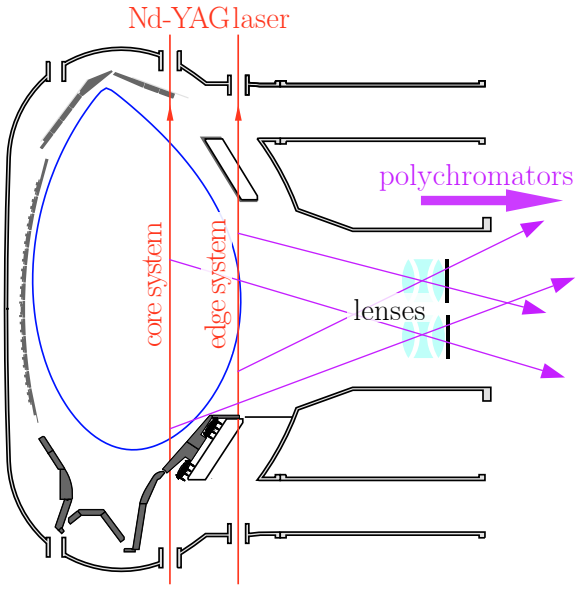

Figure 3.4: Illustration of the Thomson scattering system (courtesy of B. Kurzhan).

3.3 Experiments with non-thermal electrons

To study the steady state, non-thermal electron distribution function during intense microwave heating thirteen dedicated experiments were conducted at ASDEX Upgrade within the framework of this thesis. To allow a successful interpretation of the measurements the experiments had to fulfill a wide of range of boundary conditions. In this section the different aspects of said boundary conditions are discussed and three discharges where all boundary conditions were met satisfactorily are introduced.

3.3.1 Optimization for ECE measurements

For the successful measurement of the electron distribution function with ECE the experiment has to fulfill three conditions. Most importantly is, of course, that the non-thermal features of the distribution are large enough to be detected with ECE. The "non-thermalness" of a distribution due to ECRH scales with $1/n_e^2$ [69]. It also increases with rising T_e which decreases the frequency of thermalizing collisions.

Further boundary conditions arise because of the cross calibration of the oblique ECE. The cross-calibration is only meaningful if the distribution function is thermal. Even though non-thermal electrons induced by ECCD are expected to relax quickly after the ECRH switch-off, it is possible for the ECCD to seed slide-away distributions which are sustained by the plasma current alone. To avoid the contamination of the cross calibration by a slide-away distribution is has to be, either, performed before any ECRH is applied or at elevated density after any phase with ECCD. To estimate of the systematical uncertainties of the cross calibration it is also necessary to vary T_e during the cross calibration. If ECRH is used for the T_e variation, n_e has to be large to avoid the generation of non-thermal electrons. Unfortunately reducing n_e by pumping is a slow process. Hence, if the calibration has to be done before any fast electrons are generated the T_e modulation has to be performed by NBI heating only and at low n_e. For a sufficiently large modulation of the T_e profile at least 1 MW of NBI power is required.

Lastly, parametric decay of ECRH waves has to be avoided, since they appear as bursts in the oblique ECE measurements severely complicating the data analysis. The majority of the parametric decay events observed at ASDEX Upgrade are correlated with edge localized modes, a Magnetohydrodynamic (MHD) instability that occurs at the edge of high confinement mode plasmas [91]. Accordingly, the amount of parametric decay events can be drastically reduced if the plasma is operated in low confinement mode, where the Edge localized mode do not occur.

3.3.2 Validity range of the theoretical model

The Fokker-Planck model used in this thesis for the computation of the distribution function including ECRH damping, the parallel electric fields and the radiation reaction force. The result of the calculations is the steady-state distribution for the given experimental conditions. The model uses realistic time steps and it usually takes about 50 ms to reach steady state. During this time T_e, n_e, the magnetic equilibrium and the ECRH power are assumed to be constant. Furthermore, the starting point of the calculations is always a thermal distribution and all possible hysteresis effects that could occur in the experiment are excluded.

3.3.3 Discharge design

To summarize the previous sections, the discharge program should feature two phases. One with low n_e and large T_e for the non-thermal electron studies, i.e. a "non-thermal phase", and another phase with varying T_e and a thermal distribution function, i.e. the "cross-calibration phase". Another, quite stringent requirement is the avoidance of High confinement mode. This is not only because of the parametric decay events correlated with edgle localized modes, but also because of good particle cofinment of high confinement mode. Any transition to High confinement mode causes an irreversible and rapid rise in n_e rendering the discharge worthless. To avoid the High confinement mode the experiments use the upper divertor instead of the lower one. In the USN configuration with standard toroidal magnetic field and current the $\vec{B} \times \nabla \vec{B}$ drift points away from the X-point, which increases the power threshold for achievieing High confinement mode [92].

Without the improved energy confinement of High confinement mode and only two gyrotrons compatible with the oblique ECE measurements it was initially assumed that a so-called internal transport barrier was necessary in order to reach T_e large enough for a sufficiently strong non-thermal electron generation. One method to generate internal transport barriers is the application of central, counter ECCD early in the discharge, when the plasma current has not fully diffused to the center of the plasma. For counter ECCD the current generated by the waves flows in the direction opposite to the plasma current. This causes a local reversal of the magnetic shear near at the deposition site of the ECRH [93]. The resulting reduction in turbulence leads to a steep rise in T_e. While it was possible to generate a transport barrier with just the two available gyrotrons the transport barriers proofed highly transient and the rapid changes in the central T_e were irreconcilable the steady-state conditions required for the simulations. Since the transient behavior of the transport barrier was anticipated, a backup "non-thermal phase" was incorporated into the discharge. In this phase also counter ECCD was used, because the toroidal injection angle of the ECRH cannot be changed during a discharge. Nevertheless, the formation of a transport barrier could be avoided by giving the plasma current sufficient time to diffuse to the center of the plasma before applying the ECCD. Since the non-thermal electron generation proved to be very strong even without a transport barrier phase, the early ECCD was removed in subsequent experiments. With counter ECCD being no longer mandatory one experiment was dedicated for the study of non-thermal electrons generated by co-directional ECCD, i.e. the case when the current produced by the waves and the plasma current point in the same direction.

3.3.4 Experiments

The quite stringent boundary conditions of the scenario were met in three of the thirteen dedicated scenarios. For each of the scenarios a time window was chosen for the study of the non-thermal electrons while multiple time windows where considered for the cross-calibration of the oblique ECE diagnostic. In the following the time traces of the discharges are discussed. Since the analysis of the individual time windows requires some details on the data analysis techniques, their discussion was moved to later sections. The cross calibration is discussed in Section 5.4 and the phases with non-thermal electrons in Section 6.1.1.

Discharge #33697

Discharge #33697 can be subdivided into three phases as indicated in Fig. 3.5. The figure depicts the time traces of T_e and n_e on the magnetic axis and the input power by ECRH and NBI. The blue shading marks the phase with a strong transport barrier, the pink shaded region is a phase with a stationary non-thermal distribution function and the cross-calibration commences in the green shaded phase with NBI heating. The first phase with a strong, but unstable transport barrier does not reach steady state conditions. The second phase reaches steady-state at $t = 4.4\,\mathrm{s}$ for 800 ms and is used for the measurement of the non-thermal distribution function. During the cross calibration phase (green) T_e is continuously reduced, which allows the systematic uncertainties of the cross-calibration to be estimated (see also 5.4). To inhibit the drive of fast electrons n_e is increased by a factor of three and the ECRH was shifted outwards, radially reducing the absorbed power density significantly. The details of the ECRH launcher configuration and the oblique ECE antenna pattern can be found in Section 6.1.3.

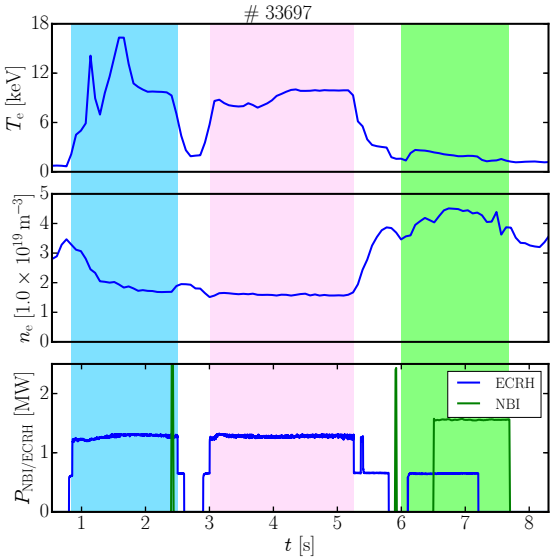

Figure 3.5: Time traces of core T_e, n_e, and external heating powers by ECRH and NBI for discharge #33697. The blue shading marks the phase with a strong internal transport barrier, the pink shaded region is a phase with a stationary non-thermal distribution function, and the cross-calibration commences in the green shaded phase.

Discharge #33705

Discharge #33705 is similar to #33697 with the sole distinction is that the calibration is done first replacing the phase with the transport barrier. Two phases with counter ECCD follow. Since #33705 also used the USN configuration, pumping proofed to be very slow as can be seen by the very slow decay of the density in the non-thermal phase (c.f. Fig. 3.6 a)). This was anticipated and the density of the calibration phase was chosen to be lower than in the calibration phases in #33697. No ECRH is applied in the calibration phase to assure a thermal electron distribution function. The change in n_e should be small enough to allow a steady-state approach in the analysis. Nevertheless, the non-thermal response is reduced in #33705 due to the higher n_e compared to #33697.

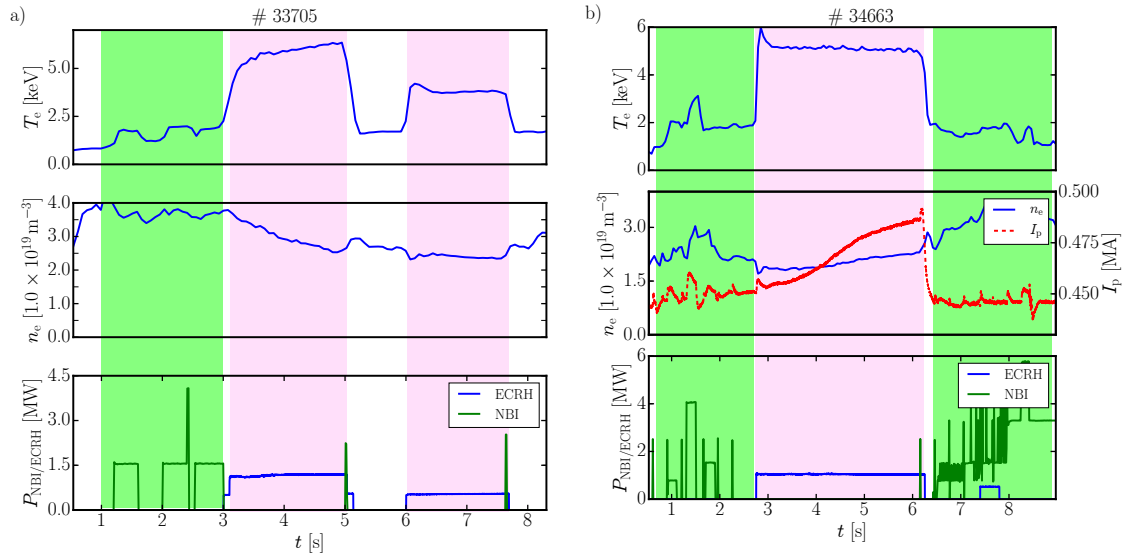

Figure 3.6: Like Fig. 3.5, but for a) #33705 and b) #34663. Figure b) also shown the plasma current.

Discharge #34663

Initial Fokker Planck calculations predicted very large ECCD currents. Unfortunately all diagnostic for the current at ASDEX Upgrade, like the motional stark effect diagnostic [94] or polarimetry [95] are either incompatible with the parameters of the experiment or not very accurate at low density. Consequently, the ECCD current cannot be measured directly. To get an estimate for the ECCD efficiency a different experiment was required to determine the driven current. For this purpose two discharges with the same ECRH power are compared. Once the power is injected radially, i.e. without ECCD, and

once obliquely giving rise to a current co-directional with the plasma current. In both discharges the loop voltage, which drives the plasma current, is the same and, therefore, the difference in total current would be the current generated by the ECCD. For the experiment to succeed the T_e profiles in the two discharges have to match such that the plasma conductivity is the same and the loop voltage indeed produces the same plasma current in both cases. Unfortunately, most likely due to a degradation of plasma purity, the T_e profiles could not be matched in the experiment and it was not possible to asses the driven current in the experiments. Despite failing its primary objective the discharge #34663 with co-ECCD is still useful to investigate the steady state distribution function during co-ECCD as will be shown in Chapter 6. The time traces of the most important quantities is shown Fig. 3.6 b). In this figure also the plasma current is shown. In the pink shaded phase the loop voltage is constant and the applied ECCD raises the plasma current, which does not reach a stationary state. Before and after the time window shaded pink in Fig. 3.6 b) the loop voltage is controlled externally to produce a constant plasma current.

4 Data analysis techniques

4.1 Integrated data analysis

At ASDEX Upgrade the measurements of multiple diagnostics for T_e and n_e are combined with the Integrated Data Analysis (IDA) code package to deliver unified profiles. The principle of the IDA is Bayes' Theorem [96]:

$$P(H \mid E) = \frac{P(E \mid H)P(H)}{P(E)} \tag{4.1}$$

where the measurements are represented by E while H represents the hypothesis that supposedly explains the measurements. $P(H \mid E)$ is also called the *posterior* and it is the probability that the hypothesis is correct given the experimental observation. $P(H)$, called *prior*, contains the a priori belief in the hypothesis. $P(E)$ is the *model evidence* and it the probability of the measurements given all possible hypothesis. Lastly $P(E \mid H)$ is the *likelihood*, which is the probability of the experimental quantities to be observed given the current hypothesis. In practice one wants to find the hypothesis or model that maximizes the posterior. The model evidence can be discarded, because it is independent of the hypothesis and the absolute value of the posterior is irrelevant. To compute $P(E \mid H)$ it is necessary to calculate synthetic measurements for the current hypothesis. This is accomplished with forward models.

In the IDA toolkit the hypothesis are parameterized T_e and n_e profiles as functions of ρ_{pol}. Each of the considered diagnostics has a forward model and the most likely T_e and n_e profile is determined by maximizing the posterior probability [96]. An example for the prior could be a monoticity constraint on the profiles. The IDA framework is capable of considering measurements from ECE [11] (T_e), the Thomson scattering diagnostic [90] (T_e, n_e), lithium beam emission spectroscopy [97] (n_e), and plasma interferometry [98] (n_e). For this thesis a time window of 1 ms is considered for all diagnostics except for the Thomson scattering diagnostic, for which the time window is chosen individually for each discharge.

4.2 The ECRad code

The ECRad code was developed as a part of the present thesis. It solves the geometrical optics equations and the radiation transport equation to obtain synthetic ECE measurements. It is written in Fotran90. OpenMP parallelization allows for the geometrical optics and the radiation transport equations to be solved for multiple channels simultaneously. There exist several similar codes, e.g. SPECE [99], TRAVIS [52] and NOTEC [100]. ECRad distinguishes itself from the other codes through its optimization for large scale, automatized data analysis and its support for arbitrary, numerical distribution functions. ECRad is the forward model for the analysis of the ECE data in IDA and in this thesis it is used for the computation of synthetic ECE spectra for non-thermal distribution functions. One of its primary features is that the calculated ECE spectra are differentiable with respect to the input parameters. This includes T_e and distribution function profiles, and to some extent the n_e profile and the magnetic equilibrium. To apply IDA on a large scale the maximum posterior search has to be performed with gradient-based optimization methods. Hence, the forward models employed in the IDA code have to provide synthetic measurements that are continuously differentiable with respect to the T_e and n_e profiles. This inhibits the usage of random number based algorithms, root finding and adaptive step size methods in the forward models. Additionally, they have to be reliable and numerically robust for a large range of input profiles. In this section several key aspects of the implementation of the ECRad code are discussed.

4.2.1 ECRad as a forward model in IDA

One of the primary design goals of ECRad was to analyze the ECE measurements of the profile radiometer at ASDEX Upgrade within the framework of IDA. For this particular problem it was known beforehand that refraction of the LOS was not of critical importance. Accordingly, it is not necessary to solve the geometrical optics Eqs. for every single optimization step. For this reason the calculation of T_rad is split in two steps. Before entering the main optimization loop, the geometrical optics Eqs. are solved, completely independently of the radiation transport Eq. Then, during the maximum posterior search, only the radiation transport Eq. is solved and the LOS of the diagnostic is static. To adapt to any large change in n_e during the maximum posterior search it can be beneficial to split the optimization into several sub-optimizations and recalculating the LOS between each sub-optimization. This approach is pursued in the IDA (see also Section 4.1).

4.2.2 Antenna pattern

As in the model of Ref. [11] the volume of sight of each ECE antenna is discretized into a rectangular bunch of $N_{\mathrm{ray}} \times N_{\mathrm{ray}} + 1$ rays. The rays are spanned on a grid suitable for Gaussian quadrature. The +1 is because there is always a central ray, which does not enter the computation of T_{rad}, unless $N_{\mathrm{ray}} = 0$. The purpose of the central ray is to map various quantities of the ray bundle to a singular ray. It is assumed that the volume of sight of the diagnostic is a Gaussian beam with the $1/e$ beam width w of the electric field.

One of the limitations of geometrical optics is that diffraction is neglected and the beam waist is zero at the focus point. To mitigate this, the initial conditions of the rays are chosen such that the beam width w at the focus point s_{focus} equals the beam waist expected of a Gaussian beam in vacuum. The evolution of the beam waist of a Gaussian beam in vacuum is given by

$$w(s) = w_0 \sqrt{1 - \frac{\lambda^2 (s - s_{\mathrm{waist}})^2}{\pi w_0^4}}, \tag{4.2}$$

with s the arc length of the beam, λ the wave length, s_{waist} the position of the waist and w_0 the beam waist. Both w_0 and s_{waist} have to be calculated from the radius of curvature R_{curv} and the beam width at the antenna. To solve this problem $R_{\mathrm{curv}}(s)$ of a Gaussian beam is required:

$$R_{\mathrm{curv}}(s) = (s_{\mathrm{waist}} - s) \sqrt{1 - \frac{\pi w_0^4}{\lambda^2 (s - s_{\mathrm{waist}})^2}} \tag{4.3}$$

The discretization of frequency bandwidth is also adapted from Ref. [11] and $N_{\mathrm{freq}} + 1$ uniformly distributed sub-frequencies are assumed. The frequency discretization is only considered for the radiation transport and only the central frequency is considered in the geometrical optics Eq. to reduce computational time. For the averaging of T_{rad} over the bandwidth a Gaussian quadrature algorithm is used.

The code expects that the provided antenna position is sufficiently far away from the plasma such that n_{e} at antenna position is negligibly small. It is not required that this position lies inside the domain where the magnetic equilibrium and the input T_{e} and n_{e} profiles are defined.

4.2.3 Ray tracing

The geometrical optics Eqs. are solved using the DLSODE [101] package. Straight propagation is assumed until a position is reached, where the magnetic equilibrium and the kinetic profiles are defined and $\rho_{\mathrm{pol}} < 1.20$ or $\left(\frac{\omega_{\mathrm{p}}}{\omega}\right)^2 > 0.04$ with ω_{p} the plasma frequency. Upon plasma entry the rays are coupled to the plasma by Snell's law. The propagation is stopped if either the ray passes through a port, reaches the upper hybrid resonance $\omega_{\mathrm{UH}}^2 = \omega_{\mathrm{p}}^2 + \omega_{\mathrm{c}}^2$ in case of X-mode polarization or leaves the domain for which the magnetic equilibrium or the kinetic profiles are defined. Another noteworthy exit condition for the ray tracing algorithm are reflections at a cut-off layer inside the plasma. If the wave vector $\vec{k}(s)$ deviates by more than 90° from the initial wave vector $\vec{k}(s_{\mathrm{ant}})$ the ray tracing is stopped:

$$\arccos\left(\frac{\vec{k}(s_{\mathrm{ant}})\cdot\vec{k}(s)}{|\vec{k}(s_{\mathrm{ant}})||\vec{k}(s)|}\right) \geq 90^\circ \tag{4.4}$$

The reasoning behind this treatment is the following. Usually the core n_{e} in ASDEX Upgrade discharges is rather flat. For flat n_{e} profiles even small uncertainty in n_{e} or the magnetic equilibrium can give rise to large errors in the ray path near and especially after a cut-off layer is encountered. Accordingly, the amount of ECE that is scattered into the antenna by the cut-off layer is subject to large uncertainties. To circumvent the computational effort necessary to accurately propagate the uncertainty of the density profile onto the prediction of T_{rad} in a cut-off situation the treatment above was chosen. Since the ray path is reduced by this approach the predicted optical depth is lower than it would be for the full path. If the optical depth of the shortened path is low, the measurement can be automatically removed from the data analysis according to the criterion from Section 4.2.6. If, however the optical depth of the measurement is large then the amount of radiation scattered towards the antenna by the cut-off layer is irrelevant, because it is absorbed. Hence, unnecessary computational effort is avoided.

4.2.4 Radiation transport

The radiation transport Eq. can be solved by a simple, explicit 4th order Runge-Kutta scheme on a static grid. The grid size depends on whether the current position on the ray is close to a resonance. Near the cold resonance positions of the fundamental or the second harmonic the grid is dense. Everywhere else the grid is ten times sparser by default. This approach was adapted from Ref. [11]. An insufficiently small step size is identified by comparing T_{rad} computed with the forth order Runga-Kutta scheme to T_{rad} attained from the explicit forward Euler method at each step. If the deviation

between the two schemes is larger than 50 % the sparse and the dense step size is halved and the grid is recalculated. To avoid problems with differentiability the iterative determination of the grid size must not be carried out during an optimization. Because of this and because of the static ray paths during optimizations, it is useful to carry out several optimizations and to update the ray paths and the grid size in between optimizations.

4.2.5 Absorption and emission

The evaluation of the absorption coefficient Eq. (2.12) and the emissivity Eq. (2.11) is the most computationally intensive step when solving the radiation transport equation. Far away from a cold resonance and for sufficiently small T_e the absorption coefficient and the emissivity are negligibly small. To identify these sections on the ray trajectories a new approximation formula for the absorption coefficient was developed. The details on this approximation can be found in Appendix 1. On average the amount of evaluations of the complete absorption coefficient is reduced by 30 % to 60 % depending on the plasma scenario.

4.2.6 Wall reflections

For the lower range of measured frequencies, for which the cold resonances lie near the plasma edge or in the scrape-off layer (SOL), the optical depth of the plasma τ_ω can be very small. This means that the radiation passes through the plasma multiple times without being fully absorbed. The amount of radiation scattered into the antenna by reflections on the vessel wall can be estimated by an infinite reflection model [11]. This model assumes that neither the trajectory of the wave nor its polarization is affected by the reflection. The model has a single parameter, which is the wall reflection coefficient.

In practice this approach produces satisfactory results if $\tau_\omega > 1$. At extremely low optical depths ($\tau_\omega \lesssim 0.5$) the simple model of infinite reflections is insufficient and the agreement between forward modeled T_rad and the measurements can become quite poor (see Chapter 5). For this reason the ECRad model is not reliable if the optical depth of a measurement is below $\tau_\omega \lesssim 0.5$.

The scaling factor κ_Refl between the observed intensity $I_{\omega,\mathrm{Refl}}$ and the intensity obtained from the radiation transport I_ω is given by [102]:

$$\kappa_\mathrm{Refl} := \frac{I_{\omega,\mathrm{Refl}}}{I_\omega} = \frac{1}{1 - R_\mathrm{wall}\mathrm{e}^{-\tau_\omega}} \tag{4.5}$$

The wall reflection coefficient is given by R_wall. Note that R_wall is not only a material property, because it is also dependent on ray path. As shown in Ref. [11] values close

to one show the best fit for a majority of the measurements. In the ECRad code the wall reflection coefficients for X- and O-mode need not be identical. The default values for R_{wall} are 0.90 for the X-mode and 0.92 for the O-mode. Unless otherwise stated these values are considered for any result shown in this thesis. Per default the scaling factor κ_{Refl} is only considered for measured frequencies with $\tau_\omega < 9$.

The limitation of the current wall reflection model motivated the development of an improved wall reflection model. Although a promising approach could be formulated, the solution is computationally too cumbersome to be practical. The derivation of said improved wall reflection model and a short discussion can be found in Appendix 2.

4.2.7 The polarization filter

Most ECE diagnostics have a beam-splitting polarizer designed to filter either X- or O-mode radiation. If X-mode is desired, the filter is usually aligned with the toroidal direction of the torus. Because of the poloidal magnetic field and by some extent due to the magnetic field ripple this implies that the filter is not perfectly aligned with $\vec{B}$, even if the LOS is perfectly radial. With the ECRad code it is possible to include this polarization mismatch in the calculation of T_{rad}. In this case the measured T_{rad} is given by:

$$T_{\mathrm{rad,mod}} = \left(\vec{e}_{\mathrm{X}} \cdot \vec{p}\right)^2 T_{\mathrm{rad,mod,X}} + \left(\vec{e}_{\mathrm{O}} \cdot \vec{p}\right)^2 T_{\mathrm{rad,mod,O}} \tag{4.6}$$

The radiation temperature for X- and O-mode are calculated separately. The fractions of X- and O-mode that pass through the filter are obtained by projecting the (normalized) polarization vector $\vec{e}_{\mathrm{X/O}}$ of the X/O-mode onto the polarization vector of the filter $\vec{P}$. To calculate the polarization vector the plasma parameters at the last closed flux surface are considered. This practice is common for the determination of ECRH polarization and should also be appropriate for ECE [103]. Cold plasma dispersion is considered in the computation of $\vec{e}_{\mathrm{X/O}}$ [43, 55].

4.2.8 Input

The basic input consists of four matrices describing the magnetic equilibrium (B_{r}, B_{t}, B_{z}, Ψ_{pol}), profiles of T_{e} and n_{e} and the antenna pattern of the diagnostic. It is also possible to provide T_{e} and n_{e} as matrices, for cases where poloidal asymmetries in the kinetic profiles are to be considered. For fast electron studies it is possible to supply a distribution function profile. The distribution function grid is expected to be given as a function of ρ_{pol}, normalized momentum u and pitch angle ζ. In addition to an input file that controls the settings of ECRad needs to be provided.

4.2.9 Output

The code has two primary modes in which it operates. One is designed for speed, which produces solely the cold resonance positions, T_{rad} and τ_ω as output. The other mode is designed for highest verbosity. In this mode the radiation transport equation is always solved twice considering two sets of absorption coefficients and emissivities. Per default the primary set of T_{rad} is obtained with Eqs. (2.11) and (2.12) assuming a thermal distributions. The secondary set of T_{rad} considers the absorption coefficient and emissivity according to Ref. [53] and Kirchhoff's law. The approach from Ref. [53] features higher overall accuracy, because the absorption coefficient is derived self-consistently from the fully relativistic dispersion relation. This means it is also appropriate for ECE of the fundamental, unlike the primary model. These two features come at an increased computational cost and at reduced robustness. The purpose of the secondary set of T_{rad} is to allow the identification of cases, where Eqs. (2.11) and (2.12) are inappropriate. In case of non-thermal distributions the primary and secondary results are obtained with Eqs. (2.11) and (2.12). The primary results consider the non-thermal distributions while thermal equilibrium is assumed for the secondary results. For the details on the output files see Appendix 3.

In verbose mode ECRad produces the birthplace distribution of observed intensity binned to a signed ρ_{pol} axis, where negative signs correspond to positions on the HFS. It also provides warm resonance positions and additionally and birthplace distributions for each considered ray which allows the birthplace distribution to be fully resolved in all three spatial coordinates.

4.2.10 Interpolation of numerical distribution function profiles

To attain T_{rad} for a given distribution function profile it has to be interpolated in the radial direction and in momentum space. Furthermore, the momentum space derivatives of the distribution function are required to evaluate the absorption coefficient. The interpolation and the differentiation in momentum space is achieved with the rectangular bivariate spline from the Fitpack package [104]. The radial interpolation of the distribution function is handled with a one dimensional interpolation of each momentum space grid cell with an univariate spline which is also provided by Fitpack. Instead of interpolating the distribution function directly, the natural logarithm of the distribution function is interpolated. This assures that the values to be interpolated do not vary over several orders of magnitude and that all interpolated values are positive. Zero values in the numerical distributions are replaced by a small positive number (1.0×10^{-30}).

4.2.11 Graphical User Interface

A Graphical user interface (GUI) has been developed for computations with ECRad. The GUI features the automatic loading of profiles from the ASDEX Upgrade database, easy manipulation of the ECRad configuration and antenna pattern of the ECE diagnostic. To quickly examine the results from ECRad the GUI allows T_{rad}, τ_ω, the birthplace distributions and the ray geometry to be plotted. Lastly the GUI has tools to perform and examine cross-calibrations.

4.2.12 Validation of the ECRad code for thermal distribution functions

To avoid unnecessary computational cost and to improve numerical robustness the following simplifications are made in ECRad. The absorption coefficient is approximated under the assumption of a tenuous plasma. II. The volume of sight is discretized into a single ray. III. The IF-band width is neglected and only a single frequency per channel is computed. In the following the validity of said approximations is discussed.

Absorption coefficient

The text of the following subsection is in large identical to the text published in Ref. [57]. For the approximated absorption coefficient given by Eq. (2.12) the refractive index, the polarization vector and the energy flux are derived from the cold plasma dispersion relation. This approximation is valid for any harmonic $n > 2$ and for the second harmonic ($n = 2$) if [43, 58]

$$\omega_{\mathrm{c},0}^2 \gg \omega_{\mathrm{p},0}^2 \tag{4.7}$$

But for, e.g., $B_{\mathrm{t}} = -2.5\,\mathrm{T}$ which is typical for ASDEX Upgrade, $\omega_{\mathrm{c},0} \approx \omega_{\mathrm{p},0}$ for $n_{\mathrm{e}} \approx 6.0 \times 10^{19}\,\mathrm{m}^{-3}$. For routine data analysis at ASDEX Upgrade the radiation transport model has to perform reasonably well for densities up to the cut-off density $n_{\mathrm{e,cut\text{-}off}} \approx 1.0 \times 10^{20}\,\mathrm{m}^{-3}$. Nevertheless, for the analysis of ECE measurements the approximated absorption coefficient is a viable approximation even if the condition given by Eq. (4.7) is violated. The approximated absorption coefficient is benchmarked against the absorption coefficient derived self-consistently from the solution of the fully relativistic (or warm) plasma dispersion relation (see Ref. [53]).

The two absorption coefficients are compared in Fig. 4.1 a) for three densities $n_{\mathrm{e}} =$ 10.0, 8.0 and 6.0 $\times 10^{19}$ m^{-3} and a measurement frequency of $f = \frac{\omega}{2\pi} = 140\,\mathrm{GHz}$. In Fig. 4.1 b) $f = 110\,\mathrm{GHz}$ is chosen and, to avoid cut-off, lower densities of $n_{\mathrm{e}} = 6.0$, 4.0 and 2.0 $\times 10^{19}$ m^{-3} are selected. In both cases the angle between the magnetic

field lines and the wave vector is 85° and T_e is 8 keV. For the selected frequencies and all densities deviations in the order of 5 % to 15 % occur for almost the entire range of $\omega_{c,0}/\omega$. Larger deviations occur for $\omega_{c,0}/\omega < 1.75$ in case of the largest density respectively in Fig. 4.1 a) and b). In contrast to the absorption coefficient from the warm plasma dispersion relation the approximated absorption coefficient does not allow for wave propagation for small $\omega_{c,0}/\omega$ and large densities.

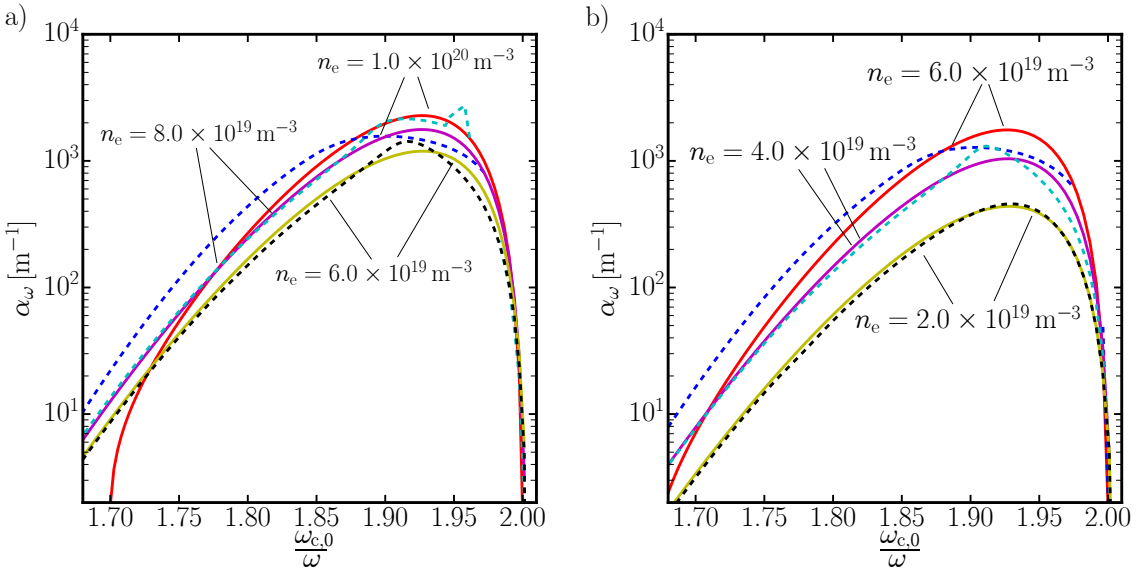

Figure 4.1: The approximated absorption coefficient of Eq. (2.12) (sold lines) and the absorption coefficient derived from the warm dispersion relation (dashed lines) are shown for f_{ECE} =140 GHz in (a) and f_{ECE} =105 GHz in (b) for three different densities each as a function of the cyclotron frequency normalized by the measurement frequency.

Figure 4.1 shows that the cold plasma dispersion produces the largest errors in when $\omega_{c,0}$ becomes smaller than ω_p, e.g. for the case with $n_e = 1.0 \times 10^{20}\,\mathrm{m}^{-3}$ for small $\omega_{c,0}$. Although the relative deviations are of the order of ten percent in the range of $\omega_{c,0}/\omega$ and all considered density and frequency combinations, in practical applications, the cold plasma dispersion for the absorption coefficient is sufficient to provide good estimates for T_{rad} for the ASDEX Upgrade ECE diagnostic.

To exemplify this, discharge # 33596 at $t = 3.48$ s is selected for the benchmark of T_{rad}. The peak temperature is about 11 keV and the density is about $6.0 \times 10^{19}\,\mathrm{m}^{-3}$, which is similar to the parameters of the benchmark of the absorption coefficients. The magnetic field of the discharge is on axis −2.5 T and the ECE channels useful for data analysis cover a frequency range from 110 GHz to 143 GHz. The result of the benchmark of T_{rad} is shown in Fig. 4.2. ECRad was used to determine the shown T_e profile. The T_e profile, the ECE measurements and the two forward modeled T_{rad} profiles

correspond to the left y-axis. The right y-axis shows the relative deviation between the two forward modeled T_{rad}. The measurements shown in the red shaded region have optical depths $\tau_\omega < 0.5$ and are not considered in the analysis. Measurements with optical depth $\tau_\omega < 0.1$ were removed from the figure. The relative deviations between the two calculated T_{rad} profiles are below 5 % for all measurements that enter the data analysis. Only channels with an extremely low optical depth of $\tau_\omega < 0.5$ show a significant deviation between the two forward modeled T_{rad} profiles. For these channels, however, the high sensitivity on the empirical wall reflection coefficient renders the T_{e} information stored in the measurement irrecoverable by the IDA method regardless of which absorption coefficient is used.

Unfortunately, the implementation of the absorption coefficient derived from the warm dispersion relation cannot be used in conjunction with non-thermal distribution function. Nevertheless, it is plausible that Eq. (2.12) is a good approximation for these scenarios, since they have extremely low density of $n_{\mathrm{e}} \approx 1.5 \times 10^{19}\,\mathrm{m}^{-3}$. Furthermore, the deformation of the distribution function by ECCD occurs mainly at high electron energies in the discharges investigated in this thesis. Hence, the bulk of the distribution function is still thermal. Although few highly energetic electrons can already cause strong ECE, the dispersive properties of the plasma are governed by the bulk of the distribution function. Hence, the cold plasma approximation of the refractive index, wave polarization and Poynting vector should also hold for the study of non-thermal ECE presented in section 6.

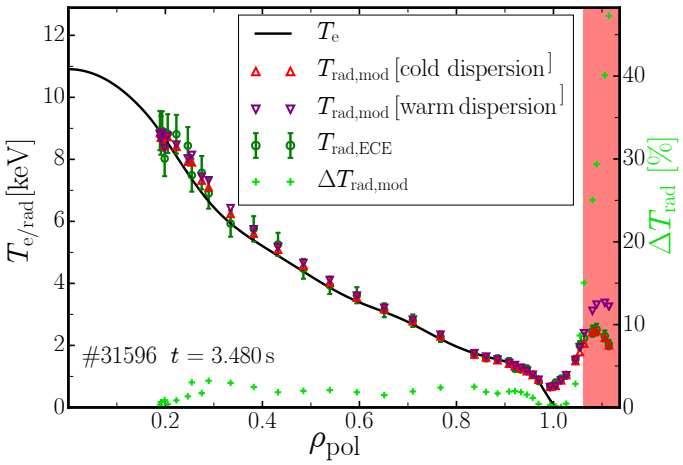

Figure 4.2: Comparison of T_{rad} calculated with the approximate absorption coefficient and the absorption coefficient derived from the warm dispersion relation. Significant deviations between the two calculated $T_{\mathrm{rad,mod}}$ ($> 5\,\%$) occur only for the channels that are highly sensitive to the wall reflection coefficient (red shaded area).

Volume of sight and frequency bandwidth discretization

As shown in Section 3.2 the waist of the volume of sight of the ECE diagnostic can be rather large. This raises the question if modeling a single ray per channel is sufficient

to get an accurate estimate for T_{rad}. Furthermore, also the bandwidth of the ECE channels could have an effect onto the forward modeled T_{rad}. A study containing a wide variety of discharges confirmed that the forward modeled T_{rad} profile is rather insensitive to the number of rays and modeled frequencies per channel.

Figure 4.3 a) shows two forward modeled T_{rad} profiles for discharge #33596 at $t = 3.48\,\mathrm{s}$, where the red triangles were calculated by assuming a single LOS per channel and the purple upside down triangles are obtained with a 4×4 bundle of rays. Approximating the volume of sight by a single ray introduces errors of the order of less than 3 % for all channels relevant for the data analysis. This motivates the single ray approximation in the routine analysis.

Figure 4.3 b) shows two forward modeled T_{rad} profiles for the same data as in a), where the T_{rad} profile depicted by the red triangles are calculated by considering a single frequency, only. The T_{rad} profile illustrated by the purple upside down triangles is obtained if the band width is discretized into eight sub-frequencies. As the light green crosses show, the error introduced by the single frequency approximation are below 2 % and are, therefore, negligible.

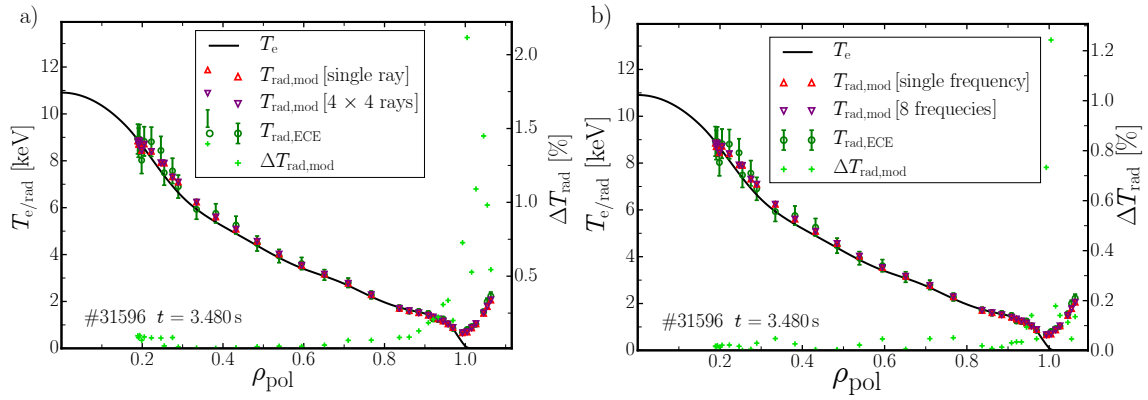

Figure 4.3: a) T_{rad} profile obtained considering a single ray shows no significant deviations ($< 3\,\%$) from the T_{rad} profile obtained if a 4×4 bundle of rays is considered. b) The T_{rad} profile obtained considering a single frequency per ECE channel show no significant deviation ($< 1.3\,\%$) from the T_{rad} profile, where the bandwidth is discretized into eight distinct frequencies. In both figures the scenario is given by discharge #33596 at $t = 3.48\,\mathrm{s}$.

4.3 Magnetic equilibrium reconstruction – IDE

To determine the shape of the flux surfaces it is necessary to solve the Grad–Shafranov equation. This equation is derived from the force balance between magnetic and kinetic

pressure in the ideal MHD limit for a tokamak plasma [105]. In many cases only magnetic measurements are considered in the equilibrium reconstruction [106] which causes the reconstruction to face ambiguity for the plasma core region. Usually this problem is overcome by applying artificial smoothness constraints. The Integrated Data analysis Equilibrium (IDE) code circumvents this problem by coupling the Grad–Shafranov equation to a current diffusion equation, which allows to lessen the influence of artificial smoothness constraints [106]. For the current diffusion equation the bootstrap current, current redistribution by sawteeth and external current sources like ECCD and neutral beam current drive are considered. The Grad–Shafranov equation solver of IDE does not only consider magnetic measurements, but also the electron pressure profile obtained with IDA, the ion pressure profile from charge exchage recombination spectroscopy and an empirical value for the effective charge and the fast ion pressure profile from the TRANSP [107, 108] or the RABBIT [109] code. Additionally, it is possible to include current measurements like form the motional stark effect diagnostic or polarimetry.

Since the pressure profile obtained with IDA enters the IDE reconstruction it is not recommended to directly carry out the IDA analysis with IDE. Rather, a two-step process is required, where the first IDA analysis uses the equilibrium reconstruction from CLISTE [110] which is optimized to work only of magnetic measurements. In the second step an IDE equilibrium is obtained based on the results of the IDA analysis. Finally, the IDA analysis is repeated with the IDE equilibrium. This iterative process was performed for the three discharge scenarios discussed in Chapter 6. For all other scenarios the CLISTE equilibria were considered.

4.4 RELAX

The steady state, non-thermal distribution functions are attained with the bounce averaged, quasi-linear Fokker-Planck code RELAX [32]. In this section the framework around the computation with RELAX and some details on collision and radial diffusion model in RELAX are discussed.

4.4.1 Framework and automatic driver for RELAX

All calculations with the RELAX code presented in this thesis were performed on the EUROFusion WP CD Gateway[1]. Since this framework is very different from the typical data management at ASDEX Upgrade a GUI was created that loads the ASDEX Upgrade data required for the calculations with RELAX and performs sanity tests on the transformed equilibria according to Ref. [111]. Afterwards it creates

[1] See http://www.euro-fusionscipub.org/eu-im

the corresponding Consistent Physical Object (CPO). The GUI also features some rudimentary plots for the analysis of the loaded data and the results of linear and quasi-linear electron cyclotron damping calculations.

An automatic driver for the RELAX calculations was developed. It takes the results from the quasi-optical, linear ray tracing code GRAY [46] stored in a CPO and automatically prepares the radial grid and the parallel electric field for RELAX. The spacing of the radial grid is decided by two factors. First the grid has to be highly resolved near the points where significant power is deposited. The second factor is the T_e profile, which needs to be resolved well enough to avoid interpolation errors. For the latter the critical quantity is the gradient of T_e normalized by T_e. The best result is attained when a set of uniformly distributed points is mapped to the inverse of the integral of the sum of the normalized power deposition profile and the normalized gradient of the T_e profile. The automatic driver also provides the parallel electric field to RELAX. It is assumed that the loop voltage is uniform in the plasma.

The bounce averaged Fokker-Planck equation is solved iteratively for a predetermined time step Δt. The size of the time step and the amount of time steps is also handled by the automatic driver for RELAX. To check whether the current RELAX run has converged it periodically checks the radiation temperatures computed by ECRad for the current set of distribution functions computed by RELAX. Hence, a run is declared as finished once further iterations in RELAX do not alter T_rad significantly. As defaults 500 time steps are performed in RELAX in between each check with ECRad.

4.4.2 Collisions and radial transport

Since the ECE is sensitive to electrons in the energy range from a few eV to several hundred keV it is necessary to include relativistic effects for the collisions. Nevertheless, it is possible to simplify the collision operator significantly by neglecting relativistic effects for collisions between two relativistic electrons, while retaining relativistic effects in collisions between a relativistic and a non-relativistic electron [68]. This approximation is justified by the fact that collisions between two relativistic electrons are are rare [68].

If the collision operator is energy conserving the issue of energy pile-up due to the continued energy influx from the ECRH arises. Therefore, it is common practice to use a truncated, momentum conserving collision operator which only considers a thermal distribution. In reality the energy pile-up is prevented by the radial energy transport in the plasma. It is not possible to include this rigorously in a bounce-averaged Fokker-Planck calculation. Too little is known about the radial energy and particle transport to make an empirical treatment feasible. To model radial transport the bounce averaged Fokker-Planck equation is coupled to a radial diffusion equation. In RELAX the model

for radial transport is designed such that any diffusive particle flow is exactly canceled by an inward pinch [35]. Hence, there is no radial particle transport and only radial heat diffusion. The diffusion equation in RELAX allows the radial diffusion coefficient to be an arbitrary function of the radial coordinate and momentum. Three different models for the velocity dependence of the radial diffusion coefficient will be compared in Section 6.5.

5 ECE analysis for thermal plasmas

In this chapter the ECE analysis with ECRad in case of thermal plasmas is discussed. The first two sections are on the inference of the T_e profile from ECE measurements within the framework of IDA. It will be demonstrated that the relativistic treatment of the distribution function in ECRad is a critical improvement over the non-relativistic Maxwellian used in its predecessor, the radiation transport forward model presented in Ref. [11]. Additionally, the more general formulation of ECRad extends the amount of ECE measurements that can be reliably interpreted within IDA. The third section is on the interpretation of oblique ECE diagnostics in general and on the specific challenge of cross-calibrating oblique ECE diagnostics against a given T_e profile. This last section is a preparation for the last chapter where the cross-calibrated, oblique ECE measurements will be used for the measurement of the electron distribution function.

5.1 Improved radiation transport modeling with ECRad

The previous electron cyclotron forward model (ECFM) [11] is compared with ECRad by using plasma scenarios with significant shine-through from the core to the edge due to heavily down-shifted emission of relativistic electrons. A direct comparison of the ECFM presented in Ref. [11] and ECRad is not possible, because for the selected scenarios ECFM faces issues with numerical stability and validity limitations.

It is emphasized that these problems arise only for the type of scenarios addressed in this section, whereas the results presented in [11] are not affected. Three modifications are made to the previous ECFM [11] for the benchmark against ECRad:

1. In the model from Ref. [11] the cut-off density of the second harmonic X-mode was approximated using $\omega_{\mathrm{c},0} = 2\omega$. While this approximation holds at the cold resonance position of the second harmonic, it is invalid for strongly down-shifted emission for which $\omega < 2\omega_{\mathrm{c},0}$.

2. The analytical solution of the emissivity integral presented in Ref. [11] relies on a numerical implementation of the Dawson integral[11], which becomes numerically

unstable strongly for down-shifted emission. Replacing the analytical solution of the integral with a Gaussian quadrature scheme avoids this problem.

3. The forward Euler solver for the radiation transport differential equation is replaced with a 4th order Runge-Kutta integrator, which improves numerical stability.

From this point on ECFM refers to the model from Ref. [11] including the modifications explained above.

5.1.1 Similarities between the two models

Both ECRad and ECFM, first calculate the LOS and then solve the radiation transport equation along the LOS in a second step. Both models assume a thermal plasma and apply Kirchhoff's law relating the emissivity and the absorption coefficient. For the comparison only the second harmonic X-mode emission is considered, because unlike ECRad, ECFM was not designed for any other harmonic or wave polarization. The infinite reflection model is used in both models [11, 102]. Like for all other calculations in this thesis the wall reflection coefficient is chosen to be $R_{\mathrm{wall,X}} = 0.9$.

5.1.2 Improvements of ECRad vs. ECFM

Compared to ECFM, ECRad has four major improvements:

1. Cold plasma refractive index and wave polarization in ECRad [55, 112] instead of $N_\omega = 1$ in ECFM [5, 11].

2. Arbitrary propagation direction of the wave inECRad [55, 112] instead of quasi-perpendicular propagation in ECFM [5, 11].

3. Fully relativistic single-electron emissivity [43, 55, 112] instead of non-relativistic single electron emissivity [5, 11]

4. Fully relativistic Maxwell-Jüttner distribution for the emissivity/absorption coefficient in ECRad [55, 112] instead of a non-relativistic Maxwellian in ECFM [5, 11]

Another minor difference is that in ECFM the emissivity is calculated explicitly and the absorption coefficient is derived using Kirchhoff's law, while in ECRad the absorption coefficient is calculated explicitly and the emissivity is derived.

shot	time [s]	n_e [10^{19}m^{-3}]	main ion species
#31594	$t = 1.30$	1.8	deuterium
#32740	$t = 5.06$	3.0	helium
#31539	$t = 3.29$	4.7	deuterium

Table 5.1: : The core electron density values and main ion species of the three benchmark scenarios.

5.1.3 Significance of improvements

In order to assess the various improvements implemented in ECRad, a hybrid model ECFM+ is introduced containing all improvements (1 to 3) except for the relativistic distribution function (4).

Figure 5.1 compares the radiation temperature T_{rad} evaluated with the three models ($T_{rad,mod}$) with the measured values $T_{rad,ECE}$ for three different scenarios. All three scenarios have strong central ECRH, correspondingly high T_e in the plasma core, and an on-axis magnetic field strength of about $B_t = -2.5\,T$. The main distinction is given by different on-axis electron densities n_e and the main ion species which are listed in Table 5.1.

The T_e and n_e profiles shown in Fig. 5.1 a), c) and e) are estimated within the IDA framework as described in Section 4.1. Only for #32740 Thomson scattering measurements of n_e replace the lithium beam spectroscopy measurements, because overlapping lithium and helium lines reduce the reliability of lithium beam spectroscopy in helium plasmas. The measured and modeled radiation temperatures in figures 5.1 a), c) and e) are mapped to the cold resonance position of the second harmonic. ECRad was used for the inference of the T_e profile and only ECE measurements within the confined region ($\rho_{pol} < 1$) were considered. Therefore, the comparison of the measured and forward modeled T_{rad} in the SOL ($\rho_{pol} \geq 1$) allows one to validate the various models.

For channels with cold resonance positions in the SOL, ECRad provides the best agreement between the measured and modeled T_{rad} even though these channels are not considered in the fit. ECFM shows the worst agreement and ECFM+, including three out of the four improvements, performs only little better. Although ECRad describes the relatively small measured ECE intensities at the outer edge reasonably well, there are residual discrepancies, especially for #31539 (c.f. Fig. 5.1 e)). These residual discrepancies are discussed in Sections 5.2.1 and 5.2.2.

In most plasmas there is no significant difference between the T_{rad} of ECFM and ECRad inside the confined region (c.f. Fig. 5.1 c) and e)). However, model ECFM performs poorly if T_e and n_e are extremely small in the edge of the confined region (c.f.

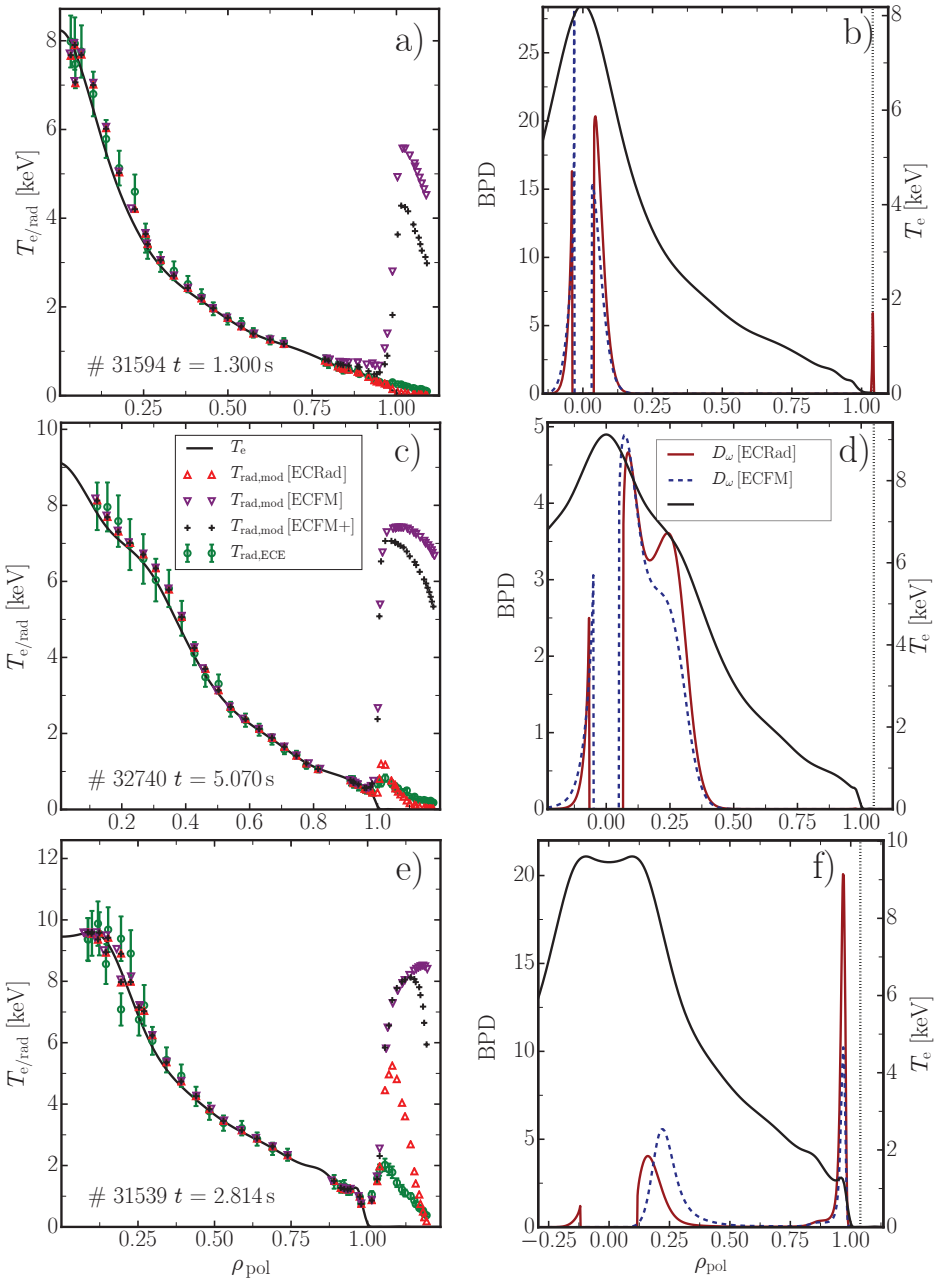

Figure 5.1: a), c), and e) : Estimated T_e profiles from radiation transport modeling in the IDA scheme as functions of ρ_{pol}. Additionally, the modeled $T_{rad,mod}$ according to ECFM, ECFM+ and ECRad are compared to the measured $T_{rad,ECE}$. Both, synthetic and actual measurements are mapped to the cold resonance position of the second harmonic. b), d) and f) illustrate the birthplace distributions of observed intensity, as calculated by ECFM and ECRad, for a channel with a cold resonance position of $\rho_{pol} \approx 1.04$ (dotted vertical line) for the three plasma scenarios of a), c) and e).

Fig. 5.1 a)). Such conditions arise at ASDEX Upgrade routinely in Ohmic discharges which necessitates the analysis with ECRad.

5.1.4 Relativistic vs. non-relativistic distribution function

For the scenarios studied with ECFM in Ref. [11] the measurements and forward modeled T_{rad} were consistent which was confirmed with ECRad. These scenarios had relatively large n_{e} ($> 5 \times 10^{19}\,\mathrm{m}^{-3}$) and moderate T_{e} ($< 5\,\mathrm{keV}$). The different performances of ECFM, ECFM+ and ECRad for the present plasma scenarios mainly result from the different electron energy distribution functions considered and the shine-through of down-shifted emission from relativistic electrons in the plasma core. The origin of the radiation is given by the birthplace distribution of observed intensity in Figs. 5.1 b), d) and f) for the cases of Fig. 5.1 a), c) and e), respectively. Negative (positive) values of ρ_{pol} correspond to positions on the HFS (LFS), respectively. The ECE channel was chosen such that its cold resonance position lies at $\rho_{\mathrm{pol}} \approx 1.04$ (dotted line).

In all three cases a significant amount of the observed radiation originates from the plasma core, which was not observed for the scenarios discussed in Ref. [11]. The gap in the birthplace distribution close to the plasma center arises from the LOS not going exactly through the plasma center. The contribution of the plasma core relative to that of the plasma edge is reduced for the scenario with the largest density as expected due to the increased optical depth. It can also be seen that in ECFM the contribution by the plasma core is larger than in ECRad for b) and e). This leads to the conclusion that the large peaks of T_{rad} in the SOL predicted by ECFM and ECFM+ result from an over-estimation of the strongly down-shifted radiation from electrons in the plasma core. The Maxwell distribution does not account for the relativistic mass increase resulting in an over-population of the relativistic speeds. With an on-axis magnetic field strength of $|B_{\mathrm{t}}| = 2.5\,\mathrm{T}$ the second harmonic of the cyclotron frequency is

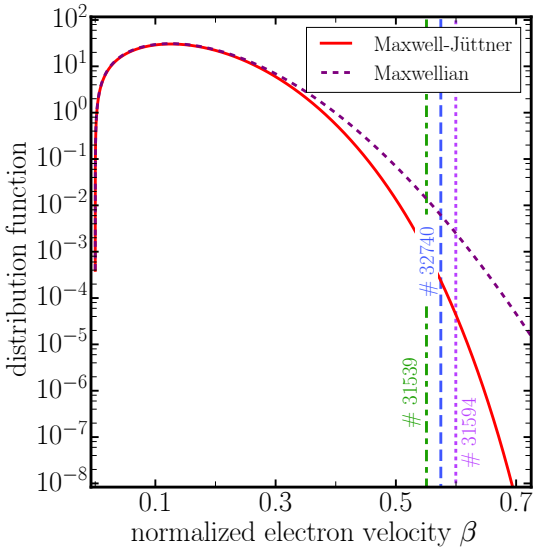

Figure 5.2: Maxwellian and Maxwell-Jüttner distribution for $T_{\mathrm{e}} = 8\,\mathrm{keV}$. The velocities with the largest amount of down-shifted emission for the SOL channels shown in Fig. 5.1 b), d) and f) are indicated.

$2f_c = 140\,\mathrm{GHz}$ in the plasma core. In contrast, the measurement frequency f_{ECE} of the channels for which the cold resonance positions lie in the SOL is only about 105 GHz. If the down-shift is attributed to the relativistic mass increase alone (i.e. if the Doppler shift is neglected), a Lorentz factor of $\gamma = 1.4$ is required. This corresponds to an electron velocity $\beta = v/c_0 = 0.7$, where c_0 is the vacuum speed of light, and a kinetic energy of about 200 keV. Hence, a relativistic distribution function needs to be used for the emissivity and absorption coefficient described in Section 2.4. Figure 5.2 compares the Maxwellian with the Maxwell-Jüttner distribution for $T_e = 8\,\mathrm{keV}$. For $\beta > 0.3$ the Maxwellian is significantly larger than its relativistic counterpart.

With the two-dimensional birthplace distribution introduced in 2.5 the velocity with the strongest contribution to the observed, down-shifted emission can be determined. It is indicated by the vertical lines in Fig. 5.2s. The variability of β from 0.55 to 0.60 is due to different Doppler shifts and the different birthplace distributions. The scenario with the smallest (largest) n_e shows the region with largest (smallest) frequency down-shift.

5.2 Limitations of ECRad

In Fig. 5.1 e) ECRad overestimates the T_{rad} measured in the near SOL. These measurements set themselves apart from other measurements in two aspects. First, they are strongly affected by emission from the plasma core, but have low optical depth unlike the usual ECE measurements of the plasma core. Second, a large quantity of the observed radiation is produced by highly energetic electrons with low collisionality. It will be shown that the latter is unlikely to be the cause of the discrepancy. Instead the most probable explanations is that ECRad's wall reflection model performs poorly for ECE measurements of the plasma core with low optical depth. This hypothesis is supported by the fact that ECRad is unable to describe the O-mode spectra observed during X-mode cut-off, which also have very low optical depth and have the origin in the plasma core region. How O-mode and the inability to predict it affects the determination of T_e in the everyday application of ECRad is discussed in the last section.

5.2.1 The Abraham–Lorentz force

A possible reason for an overestimation of T_{rad} is the omission of the Abraham–Lorentz force [74] (see Section 2.6.5), which can deplete the high-energy tail of a thermal distribution. Accordingly, the heavily down-shifted emission from relativistic electrons might be reduced. This hypothesis is supported by Ref. [71] in which it was shown that radiation drag could reduce the efficiency of electron cyclotron current drive in

future devices. A reduction of highly energetic electrons would affect the measurements significantly because the emissivity and absorption coefficient scale strongly non-linearly with the velocity perpendicular to the magnetic field ($\propto \beta_\perp^4$). This effect would only be observable for plasmas with significant intensity in the ECE channels originating from down-shifted core emission, i.e. in #31539, but not in #31594 or #32740, where the down-shifted emission from the core is too weak.

The analytical solution for the steady state distribution resulting from relativistic collisions and the radiation reaction force, as presented in Section 2.6.5, was compared with the numerical solution of this problem obtained with the Fokker-Planck code RELAX [32]. In the analytical model the mean value of the magnetic field B on each flux surface is considered, while RELAX performs the appropriate bounce-average of the magnetic field. In both approaches an effective charge $Z_{\text{eff}} = 1.5$ is assumed. The deviation of the distributions including the radiation reaction force from a thermal distribution was computed and normalized by the value of the thermal distribution. These normalized deviations are shown in Fig. 5.3 a) as functions of the dimensionless momentum perpendicular to the magnetic field $u_\perp$ for $u_\parallel = 0$ and $\rho_{\text{pol}} = 0.2$. Both distributions show a depletion of highly energetic electrons of the order of 5 % to 20 % in the relevant range of $u_\perp$ =0.6 to 0.8.

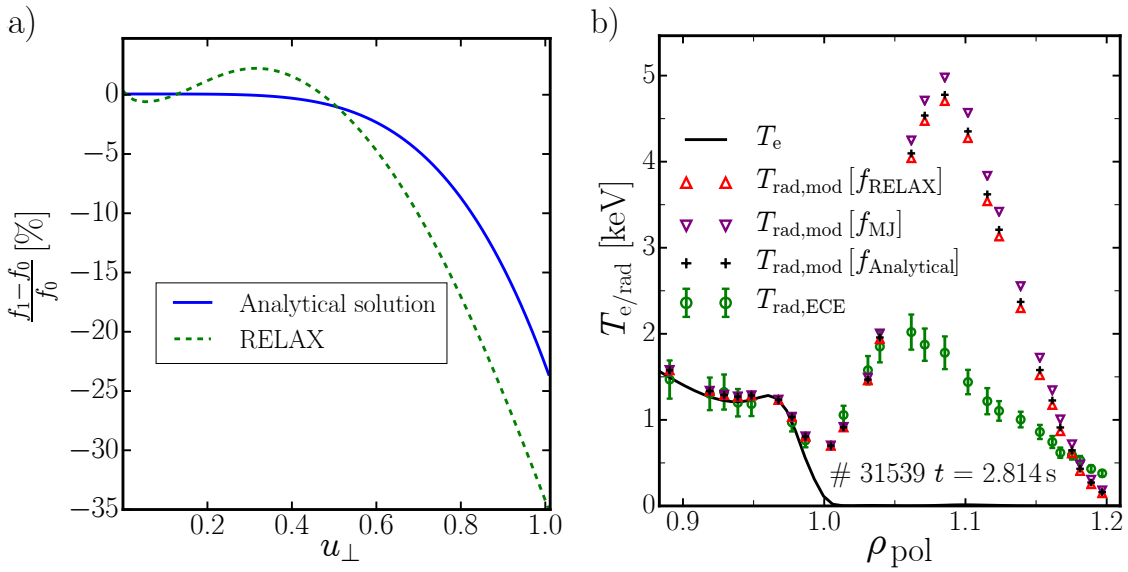

Figure 5.3: a) The normalized deviations from a thermal distribution due to the Abraham-Lorentz force are shown for the analytical and the numerical distribution function profile for $\zeta = 0$, where the deviation is expected to be strongest. b) Comparison of the forward modeled T_{rad} considering the analytically computed distribution, the distribution function from RELAX, and a thermal distribution.

In Fig. 5.3 b) T_{rad} derived from the analytical distribution-function profile and the distribution function profile of RELAX are compared to the thermal T_{rad} profile for the ECE channels with resonance positions in the SOL. The reduction of T_{rad} compared to the T_{rad} evaluated with a thermal distribution function is only of the order of a few %. This clearly shows that the effect of the Abraham Lorentz force is too small to be responsible for the overestimation of T_{rad} by ECRad in Fig. 5.1 e). The observed discrepancy between the modeled and the measured T_{rad} must, therefore, have a different reason as addressed in the following section.

5.2.2 Wall reflections

Another possible reason for this overestimation is given by the simplicity of the infinite wall reflection model (see Section 4.2.6). Figure 5.4 compares $T_{\mathrm{rad,mod}}$ computed with the wall reflection coefficients $R_{\mathrm{wall}} = 0.9$ and without reflections. The much better agreement between the measurements and the modeling without wall reflections indicates that for this discharge wall reflections might be overestimated by the infinite reflection model.

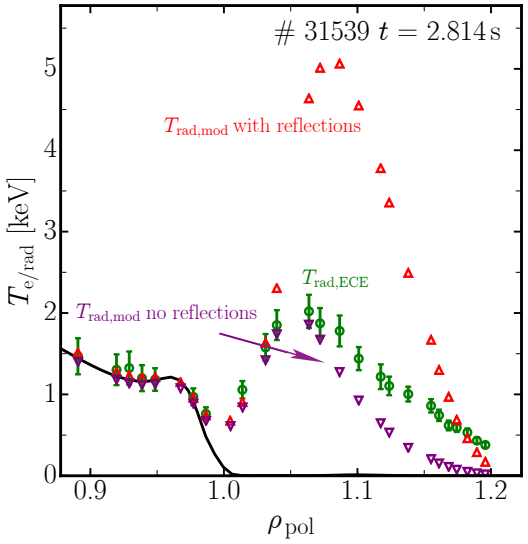

Figure 5.4: The forward modeled T_{rad} with and without wall reflections are compared to the ECE measurements in the SOL of discharge #31539.

This appears to be plausible since the infinite wall reflection model is known to be inappropriate if the optical depth is very small [102]. As discussed in 5.1.3 the optical depth of the plasma in discharge #31539, for channels with resonance positions $\rho_{\mathrm{pol,res}} > 1.04$, is $\tau_\omega < 0.2$. For this situation and assuming an idealized case of a perfectly reflecting wall ($R_{\mathrm{wall}} = 1$) more than 15 direct reflections are needed to provide a total optical depth $\tau_\omega > 3$. For these cases, it is expected that the entire plasma volume contributes to the ECE measurement [113]. Ref. [102] suggests assuming that the radiation from the plasma is in thermal equilibrium with the wall. The wall then provides an initial radiation temperature to the radiation transport equation resulting in a significantly smaller intensity at the ECE antenna compared to the infinite wall reflection model. However, the formalism of Ref. [102] cannot be directly used for radiation transport modeling, since it assumes that only emission from cold resonance positions contributes to the

measurements. This is clearly not valid for the SOL ECE channels of, e.g., scenario #31539 (c.f. Fig. 5.1 f)), where there is no significant contribution from the cold resonance position. For ECE measurements in the mid-plane it is expected that the generalized form of the reflection model of Ref. [102], as discussed in Appendix 2, results in a significantly smaller enhancement of T_{rad} than the infinite reflection model predicts. As the general form of this reflection model is computationally too demanding to find application in large scale data analysis it has, therefore, not yet been implemented into ECRad. Accordingly, a clear indicator that the wall reflection model is responsible for the mismatch between experiment and model in #31539 is still lacking and should be subject of future work.

5.2.3 O-mode emission during X-mode cutoff

The O-mode emission observed at ASDEX Upgrade is similar to the problematic measurements in Fig. 5.1 e), since its optical depth is low and most of the spectrum originates form the plasma core. An important distinction is the energy of the electrons responsible for the emission. For the down-shifted emission in Fig. 5.1 e) highly energetic electrons are responsible, while for the O-mode emission of thermal plasmas only electrons with low and medium energies contribute. In the following the time point $t = 3.298\,\mathrm{s}$ of the ASDEX Upgrade discharge #32934 will be investigated. The core n_{e} in this high confinement mode discharge is about ls $8.0 \times 10^{19}\,\mathrm{m}^{-3}$ which allows the assumption of a thermal distribution function for the interpretation of the O-mode emission. In this discharge the second harmonic X-mode emission is in right hand cut-off for most of the LFS, because the on axis magnetic field strength is 1.8 T. This is illustrated in Fig. 5.5, where $f_{\mathrm{RH}} > 2f_{\mathrm{c}}$ for all positions on the LFS. Ordinary polarized radiation can, however, propagate in the plasma. For example a measurement frequency of 98 GHz exceeds the plasma frequency f_{p} and the cold resonance position of the second harmonic is accessible. Hence, in this case all ECE measurements with resonance positions on the LFS are purely O-mode emission measurements.

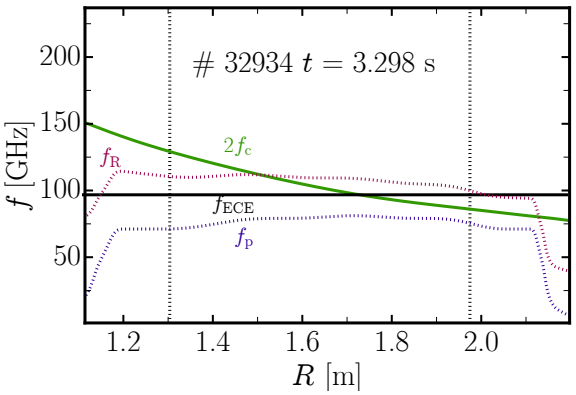

Figure 5.5: Radial dependence of the second harmonic of the cyclotron frequency f_{c}, the plasma frequency f_{p}, the right hand cut-off frequency f_{R} and a measurement frequency of 97 GHz.

As explained in Section 3.2.1 the profile radiometer at ASDEX Upgrade uses a

polarizing beam splitter that is aligned with the toroidal direction. This alignment is not ideal and a small amount of O-mode contributes to all ECE measurements, because the LOS of the diagnostic deviates slightly from a purely radial view and the magnetic field lines are slightly inclined in the toroidal direction due to the poloidal magnetic field. Consequently, the T_{rad} measured in discharge #32934 and $t = 3.298\,\mathrm{s}$ range from 200 eV to 700 eV despite the X-mode cut-off. Figure 5.6 compares the ECE measurements with the prediction of ECRad. How the T_{e} profile was obtained for this discharge and time point is described in detail in Section 5.3.2. The purple triangles in Fig. 5.6 indicate the polarizer efficiency $(\vec{e}_{\mathrm{X}} \cdot \vec{p})^2$ (right y-axis), i.e. 100 % corresponds to perfect X-mode polarization. It is about 92 %, meaning that only eight percent of the O-mode emission are detected by diagnostic. The effectiveness of the polarizer is included in the T_{rad} computed by ECRad. Nevertheless, the match between the synthetic $T_{\mathrm{rad,mod}}$ and $T_{\mathrm{rad,ECE}}$ in Fig. 5.6 is poor. There are three possible explanations.

1) Reflections at the metallic surface of the vessel are subject to mode conversion between the O and X-mode. Since the model assumes $T_{\mathrm{rad,mod,X}} = 0$ any mode conversion from O- to X-mode could greatly increase the observed T_{rad}, because the polarizing beam splitter has a much larger acceptance for X-mode radiation.

2) The calculation of the polarization vector $\vec{e}$ considers the plasma parameters of the last closed flux surface. This is common practice to obtain the optimal polarization for ECRH [103] and should also apply for ECE. However, the Faraday effect and the Cotton-Mutton effect could alter the polarization of the wave while it traverses the SOL [114]. This would then alter the efficiency of the polarizer and, consequently, change the measured T_{rad}. Unlike the influence of wall reflections, this effect is independent of the optical depth and could also affect scenarios in which the O-mode is optically thick.

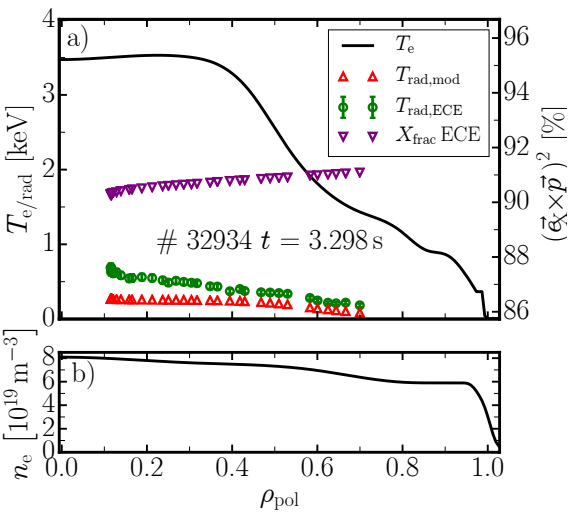

Figure 5.6: a) Measured and calculated $T_{\mathrm{rad,mod}}$ during X-mode cut-off. The purple triangles indicate $(\vec{e}_{\mathrm{X}} \cdot \vec{p})^2$, which is the acceptance of the polarization filter for X-mode (right y-axis). b) Density profile for discharge #32934 as inferred with IDA from the measurements of the lithium beam emission spectroscopy and the plasma interferometry diagnostic.

3) The optical depth of the ECE measurements depicted in Fig. 5.6 is in the range from 0.15 to 0.3. The optical depth of the measurements that cannot be described in Fig. 5.1 e) is also in the same range. Hence, the simple wall reflection model could

be the root cause for the poor performance of ECRad in both cases. It is, however, noteworthy that ECRad overestimates the T_{rad} with low optical depth in Fig. 5.1 e), while they are underestimated in Fig. 5.6. How this inconsistency could be possibly explained by an improved wall reflection model is not clear, yet.

To conclude ECRad cannot quantitatively predict the ECE of the second harmonic O-mode measured at ASDEX Upgrade.

5.2.4 Influence of O-mode for routine ECE measurements

Due to the toroidal alignment of the polarizing beam splitter a small fraction of the X-mode ECE is reflected and a corresponding fraction of O-mode emission can pass through (see Section 3.2.1 and Section 5.2.3). In the routine analysis it is assumed that only X-mode emission contributes but with 100 % of its intensity. The X-mode T_{rad} is typically much larger than the O-mode T_{rad} because of the rather low optical depth of the second harmonic O-mode ECE in ASDEX Upgrade plasmas. But still, assuming 100 % X-mode erroneously results in an overestimation of T_{rad}.

The modeling of the polarization filter shows that 5 % to 10 % of the O-mode ECE can pass through the filter. The fraction depends on the toroidal angle of the antenna (reminder: the profile ECE has several antennas) and the ratio between the poloidal and the toroidal magnetic field strength in the mid-plane. Correspondingly, the X-mode contribution is reduced by the same fraction. Wall reflections are expected to mitigate the rather small optical depth of the O-mode emission ($\tau_\omega < 0.2$). Assuming the infinite-reflection model the calculated T_{rad} spectra superposed by the O- and X-mode are at most 5 % smaller than the pure X-mode spectra. Neglecting reflections completely, results in T_{rad} of the combined O- and X-mode spectrum being 5 % to 10 % smaller than the pure X-mode spectrum. Although 5 % to 10 % overestimation of T_{rad} might be significant in special applications, for routine analysis it is considered to be negligible. Nevertheless, it is important to be aware that a certain percentage of the measured T_{rad} is O-mode emission, which is usually optically thin and, therefore, not as clearly localized as the second harmonic X-mode emission.

Even though ECRad allows one to optionally include the filter effect and the O-mode contribution at the cost of increased numerical effort the accuracy of the computed O-mode spectra is quite poor. (see Section 5.2.3).

5.3 Applications of electron cyclotron radiation transport modeling

In past work it was shown that radiation transport modeling can improve the determination of the plasma edge T_e profile in high n_e high confinement mode plasmas [11]. In this section two further situations are discussed, where radiation transport modeling yields improved T_e profiles.

5.3.1 "Pseudo radial displacement" in the plasma core

One speaks of a "pseudo radial displacement" if radiation transport effects cause the T_{rad} measured on the HFS to disagree with the T_{rad} measured at the same ρ_{pol} on the LFS [115]. Since T_e is constant on flux surfaces, this observation is inconsolable with classical ECE. The name originates from the fact that the asymmetry between the LFS and HFS ECE measurements can be resolved by shifting their cold resonance positions in the classical ECE analysis.

The "pseudo radial displacement" usually occurs in the vicinity of the magnetic axis in discharges with high T_e and low n_e. It has alredy been observed at ASDEX Upgrade [116, 117], JET [118], DIII-D [60] and Tore Supra [119]. Figure 5.7 a) shows ECE measurements from discharge #30907 at $t = 0.73\,\mathrm{s}$ with a large T_e gradient and a relatively low electron density of $n_e \approx 1.2 \times 10^{19}\,\mathrm{m}^{-3}$ in the plasma core. The measurements near the magnetic axis, where the T_e gradient is large, exhibit a loop structure which is due to the "pseudo radial displacement". ECRad is able to describe the measurements. The "pseudo radial displacement" is also intrinsically included in the radiation transport model of Ref. [11]. However, since the "pseudo radial displacement" is observed at ASDEX Upgrade only in high T_e discharges where the usage of a non-relativistic Maxwellian is inappropriate (see Section 5.1.3), only ECRad allows the consistent description of ECE measurements in scenarios exhibiting "pseudo radial displacement".

In Fig. 5.7 b) the measured and forward modeled T_{rad} are mapped to a signed ρ_{pol} axis, where position on the HFS (LFS) have a negative (positive) sign. With this coordinate system it is clear that T_{rad} on the HFS (LFS) is smaller (larger) than T_e at the cold resonance position.

The "pseudo radial displacement" is a shine-through effect, meaning that radiation shines through the plasma layer near the cold resonance position. The birthplace distribution functions for two measurement frequencies are shown in Fig. 5.8. For one of the frequencies the cold resonance position lies on the HFS and for the other one on the LFS. Both birthplace distributions are shifted away from the cold resonance positions

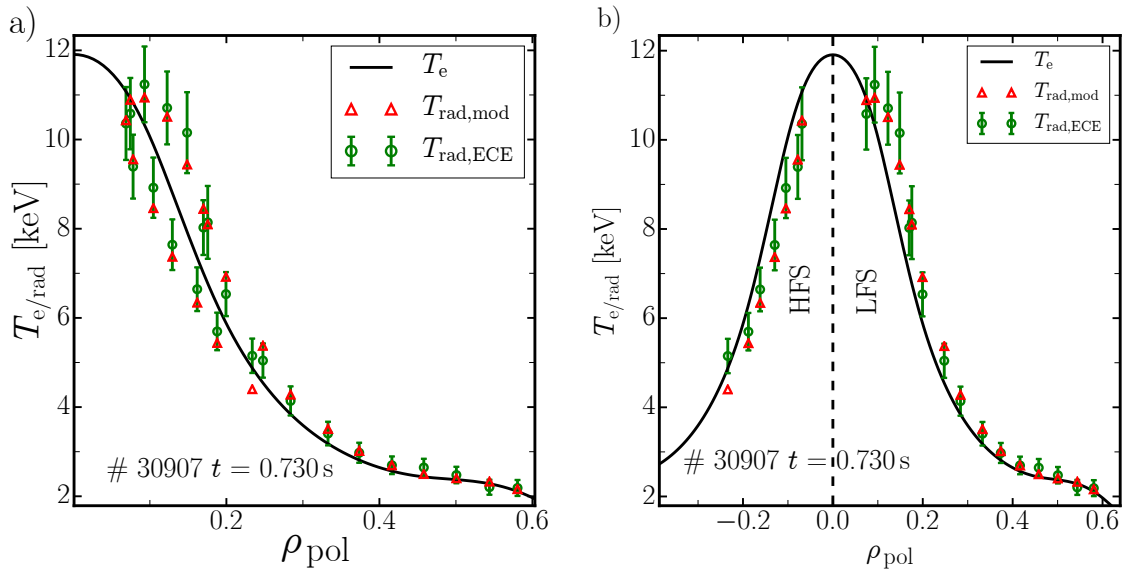

Figure 5.7: Loop structure of measured $T_{\mathrm{rad,ECE}}$ as a function of the magnetic coordinate and the T_e profile estimated using radiation transport modeling in the framework of IDA. In the right figure cold resonance positions on the HFS have negative normalized coordinates.

towards HFS. The relativistic mass increase is responsible for this. It reduces the average cyclotron frequency of the electrons. This also explains why the reabsorption at the cold resonance is weakened enough to allow a shine-through in the first place. For the cases discussed in Section 5.1.3 the shine-through was possible because T_e was very small at the cold resonance position resulting in locally weak absorption. For the ECE measurements affected by "pseudo radial displacement" in Fig. 5.7, T_e is large at the cold resonance position. Given sufficiently large T_e most electrons travel at relativistic speeds and, therefore, the mass shift inhibits them from fulfilling the resonance condition at the cold resonance position. In essence at large T_e the non-relativistic portion of the distribution function becomes depleted and the majority of the electrons exhibit a shifted electron cyclotron frequency. Consequently, absorption directly at the cold resonance position is reduced and radiation from flux surfaces further towards the HFS shines through the cold resonance position.

As the name already suggests the "pseudo radial displacement" can be compensated by introducing shifts to the measurements position of the ECE. If the birthplace distribution function of a measurement is known, it is possible to determine a *warm resonance position*. It is only meaningful if the birthplace distribution is unimodal and has low skewness. As demonstrated in Ref. [120] the warm resonance positions can also be supplemented by asymmetric error bars in the radial direction to indicate

the width of the birthplace distribution. Even, though the birthplace distributions in Fig. 5.8 a) are quite skewed, mapping to the measurements to warm resonance position still removes the "pseudo radial displacement" from the measurements as illustrated in Fig. 5.8 b).

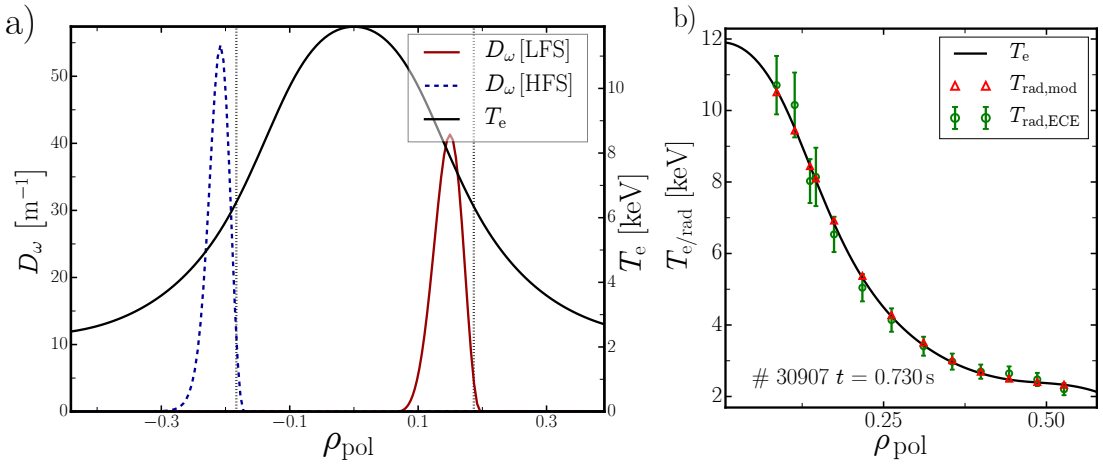

Figure 5.8: a) Birthplace distributions for two of the measurement frequencies shown in Fig. 5.7. One of which has the cold resonance position on the HFS the other on the LFS. b) shows the same data as Fig. 5.7 but the measured and the forward modeled T_{rad} are mapped to warm resonance positions.

Even though the loop structure in the ECE measurements in Fig. 5.7 a) can be explained by "pseudo radial displacement", a similar loop structure might also occur (and is observed) when the flux surfaces of the magnetic equilibrium are inaccurately estimated. For the present case the equilibrium was validated using tomographic reconstruction of the soft X-ray measurements [121]. The soft X-ray reconstruction confirmed the position of the magnetic axis with an upper uncertainty margin of 1 cm and shifting the magnetic axis by 1 cm in any direction affects the HFS-LFS asymmetry of the ECE measurements negligibly.

Generally, it is possible to distinguish the two possible sources of the loop with radiation transport modeling. While loop structures due to "pseudo radial displacement" can be described by radiation transport modeling any errors in the equilibrium reconstruction canno. They will appear as residual loop structures which provides valuable feedback for the improvement of the equilibrium reconstruction [122].

5.3.2 3rd harmonic emission and harmonic overlap

The application of ECE for high n_e operation is limited by cut-offs, which is expected to hamper the use of the ECE diagnostic in future fusion devices. One solution to this

problem is to measure the emission of higher harmonics. In the case of ASDEX Upgrade one can measure third harmonic instead of the second harmonic X-mode emission, which increases the cut-off density by a factor of 1.5 compared to the second harmonic emission. However, this approach is of limited applicability for two reasons. The first is that the absorption at the third harmonic in medium size devices like ASDEX Upgrade is small. This broadens the birthplace distribution significantly compared to second harmonic emission. The second challenge is harmonic overlap. Typically, the cold resonance position of third harmonic ECE lies on the LFS and it can be accompanied by an additional cold resonance position to the second harmonic on the HFS. The combination of the low optical depth of the third harmonic resonance with the harmonic overlap can cause the second harmonic emission from the HFS to shine through the absorption layer of the third harmonic [123]. Hence, in order to estimate the T_e profile the mixture of X2 and X3 emission needs to be modeled properly.

An example of harmonic overlap is illustrated in Fig. 5.9 for the ASDEX Upgrade discharge #32934 at $t = 3.298\,\mathrm{s}$ with a magnetic field of $B_t = 1.8\,\mathrm{T}$ and a plasma core density of $\approx 7.4 \times 10^{19}\,\mathrm{m}^{-3}$. Figure 5.9 shows the corresponding plasma frequency f_p, the right-hand cut-off frequency f_R, and the fundamental, second and third harmonic of the cyclotron frequency f_c. For the entire LFS ($R > 1.65\,\mathrm{m}$) the X-mode emission of the second harmonic is inaccessible, because the right-hand cut-off frequency $f_R > 2f_c$. In contrast, an increased measurement frequency of $f_{ECE} > 129\,\mathrm{GHz}$ (black solid line) is not in cut-off, but introduces the problem of harmonic overlap.

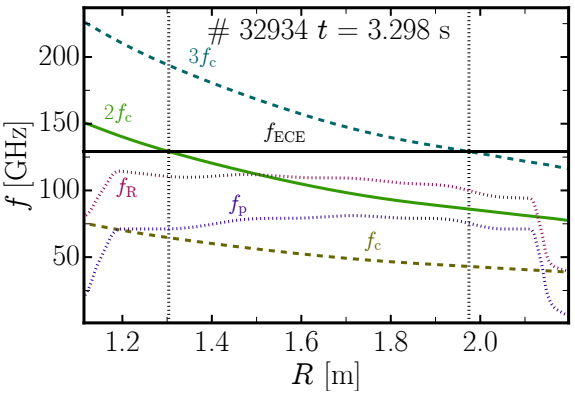

Figure 5.9: Radial dependence of the first, second, and third harmonic of the cyclotron frequency f_c, the plasma frequency f_p, the right hand cut-off frequency f_R, and a measurement frequency of 129 GHz.

At DIII-D the harmonic overlap has been addressed by calculating the optical depth of the X3 resonance and by evaluating T_{rad} from the mixture of X2 and X3 radiation under the assumption of $T_{rad} = T_e$ at the positions of both cold resonances [123]. Compared to the rigorous treatment employing radiation transport modeling, the DIII-D approach has two disadvantages. The first is that the method of Ref. [123] inherently requires Thomson scattering measurements to determine T_e at the cold resonance position of the second harmonic. The second disadvantage is that any kinetic broadening of either resonance is neglected.

The radiation transport model in the IDA framework allows one to determine the

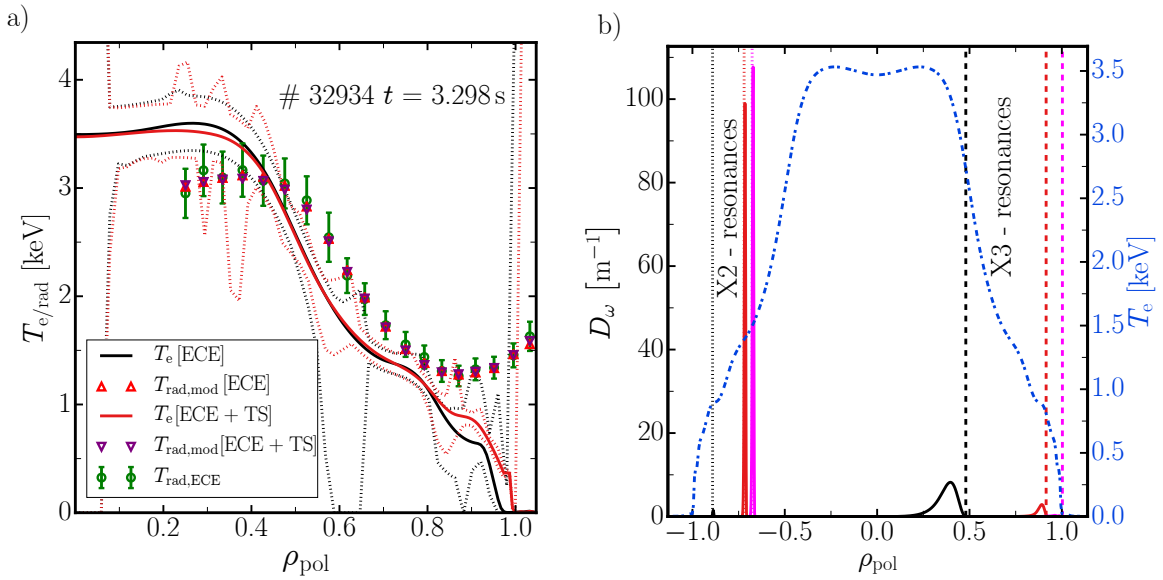

Figure 5.10: a) T_e profiles and their corresponding uncertainties (dashed lines) estimated from ECE measurements ($T_{rad,ECE}$) only (T_e[ECE]) and (T_e[ECE + TS]) which results from the combined analysis of ECE and Thomson scattering data ($T_{e,TS}$). The ECE measurements are mapped to the third harmonic cold resonance positions. Both sets of modeled ECE measurements $T_{rad,mod}$[ECE] and $T_{rad,mod}$[ECE + TS] agree reasonably well indicating a lack of information in the ECE data for $\rho_{pol} > 0.8$. b) T_e profile and the birthplace distributions for three of the channels shown in a) with cold resonance ρ_{pol} of the 3rd harmonic at 0.48 (black), 0.90 (red) and 1.01 (magenta). The vertical lines show the 2nd (dotted) and 3rd harmonic cold resonance positions (dashed).

T_e profile by only considering T_e information from ECE measurements. This works for any plasma region provided that significant local T_e information is supplied by the ECE measurements. Figure 5.10 a) shows discharge #32934 at $t = 3.298$ s where harmonic overlap has to be considered for nearly all channels. In contrast to the previous figures, the measured $T_{rad,ECE}$ are mapped to the cold resonance position of the third harmonic. The black line depicts the T_e profile estimated from ECE measurements only. The black dashed lines indicate the upper and lower error band of the T_e profile. Although for all measurement channels $T_{rad,ECE}$ is matched very well, T_e is only reliable in the region of $\rho_{pol} < 0.8$. The T_e profile has large upper and lower uncertainties for $\rho_{pol} > 0.8$, because the ECE measurements do not provide significant information on the T_e profile in this region. Figure 5.10 b) shows the birthplace distributions for three selected channels. The black line corresponds to a channel for which the cold resonance positions to the second harmonic lies at $|\rho_{pol}| = 0.88$ on the HFS. The cold resonance position of third harmonic of the same channel lies at $\rho_{pol} = 0.48$ on the LFS. Only

the strongly broadened emission by the third harmonic contributes significantly to the measured intensity. The red line corresponds to a channel with cold-resonance positions $|\rho_{\mathrm{pol}}| = 0.71$ on the HFS (second harmonic) and at $\rho_{\mathrm{pol}} = 0.90$ on the LFS (third harmonic). Both harmonics contribute to the measured intensity. The magenta line corresponds to a channel with cold resonance positions at $|\rho_{\mathrm{pol}}| = 0.66$ on the HFS (second harmonic) and in the SOL ($\rho_{\mathrm{pol}} = 1.01$, third harmonic). Although mapped in figure 5.10 a) to the third harmonic resonance position only, the emission of the second harmonic contributes to the measurement. Hence, on the LFS the contribution by the third harmonic $|\rho_{\mathrm{pol}}| > 0.90$ is very small. Simultaneously, the second harmonic emission from the HFS with $|\rho_{\mathrm{pol}}| > 0.90$ is reabsorbed by the resonance with the third harmonic (c.f. the birthplace distribution depicted by the black line in Fig. 5.10 b)). Consequently, the ECE does not provide any information about T_{e} in this region.

Although the method intrinsically works without additional diagnostics, improved results in regions with poor ECE coverage can be obtained if the ECE measurements are supplemented with Thomson scattering data. The red line in Fig. 5.10 a) depicts the T_{e} profile of the combined analysis $T_{\mathrm{e}}[\mathrm{ECE} + \mathrm{TS}]$ and the red dashed line the corresponding upper and lower error margins. For $\rho_{\mathrm{pol}} < 0.8$ Thomson scattering does not provide significant additional information. It only confirms the ECE measurements. For $\rho_{\mathrm{pol}} > 0.8$ the lack of information from ECE is compensated by Thomson scattering. The modeled values $T_{\mathrm{rad,mod}}[\mathrm{ECE}]$ and $T_{\mathrm{rad,mod}}[\mathrm{ECE} + \mathrm{TS}]$ agree very much indicating that the large error bars for $\rho_{\mathrm{pol}} > 0.8$ in the T_{e} profile considering ECE only is indeed resulting from missing information.

5.4 Cross calibration of oblique ECE diagnostics

The typical hot-cold-calibration technique [85] is not possible for all ECE diagnostics. An example is the ASDEX Upgrade collective Thomson scattering system, here used as an oblique ECE (see Section 3.2), where a dependence of the calibration coefficient on the orientation of the last mirror in the beam line was identified. This mirror is responsible for the poloidal angle of the LOS and consequently the calibration would have to be a function on the poloidal angle, which is too labor-intensive to be feasible. Absolute measurements of T_{rad} can still be performed if the diagnostic is cross-calibrated against another diagnostic. For oblique ECE diagnostics classical ECE analysis is inappropriate because of the LOS is subject to strong refraction and up-shifted emission contributes to the measurement because of the Doppler-effect. Hence, radiation transport modeling is required for the cross-calibration as will be demonstrated in this section. Furthermore, the details of the cross-calibration method are explained in Section 5.4.2. In the last subsection the cross-calibrations of the discharges considered in the non.thermal electron

studies are discussed.

5.4.1 Interpretation of oblique ECE diagnostics

Figure 5.11 a) shows the refractive index parallel to the magnetic field $N_\parallel$ ($N_\parallel \equiv N_\omega \cos\theta$ see Section 2.2) for the radial oblique ECE and discharge #33000 at $t = 6.011\,\mathrm{s}$. Generally $N_\parallel$ for the oblique ECE is eight times larger than for the radial ECE. The corresponding birthplace distribution for the two diagnostic configurations are compared in Fig. 5.11 b). For the radial ECE the distribution is sharply peaked and displaced only slightly from the cold resonance to the HFS by the relativistic mass increase. For the oblique ECE it is shifted significantly to the LFS because of the Doppler effect (see Eq. (2.20)).

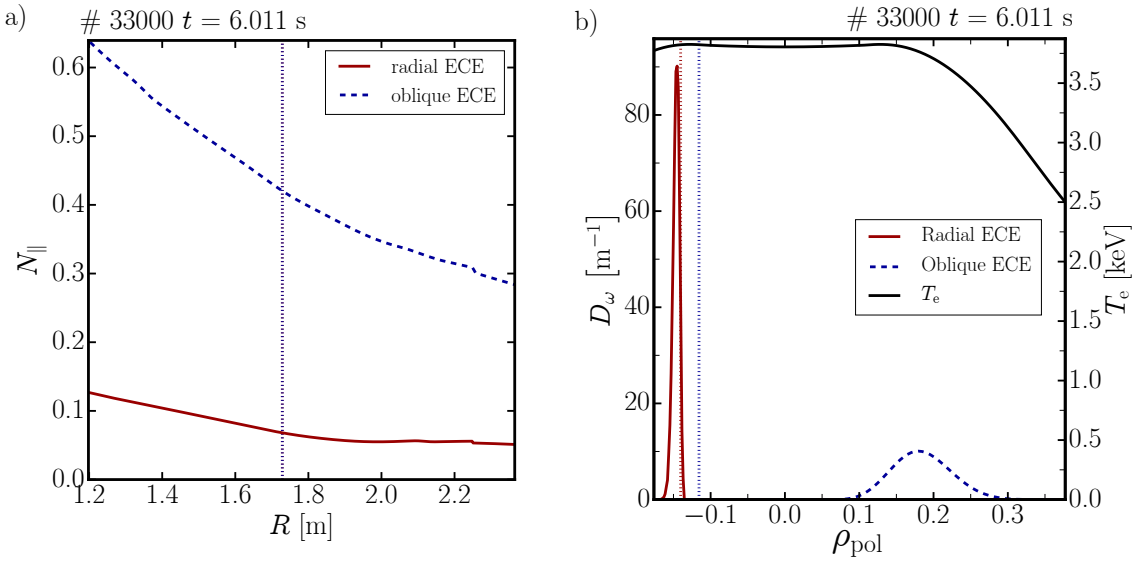

Figure 5.11: a) shows the refractive index parallel to the magnetic field for the radial and the oblique ECE. The cold resonance positions of both diagnostics are indicated by the vertical line. Figure b) compares the birthplace distributions of the two configurations.

Additional to the enhancement of the Doppler shift for oblique ECE diagnostics the large angle between magnetic field and LOS also increases the importance of refraction. Figure 5.12 compares the refracted LOS of the oblique ECE with its straight counterpart for discharge #33000 at $t = 6.011\,\mathrm{s}$) from the side in a) and with a top view b). Large deviations between the two LOSs occur. The refracted ray (green solid) deviates significantly from the straight line (purple dashed). In a) the cold resonance positions of the two rays are displaced vertically by 4.5 cm. The toroidal distance between the resonances in b) is about 10 cm.

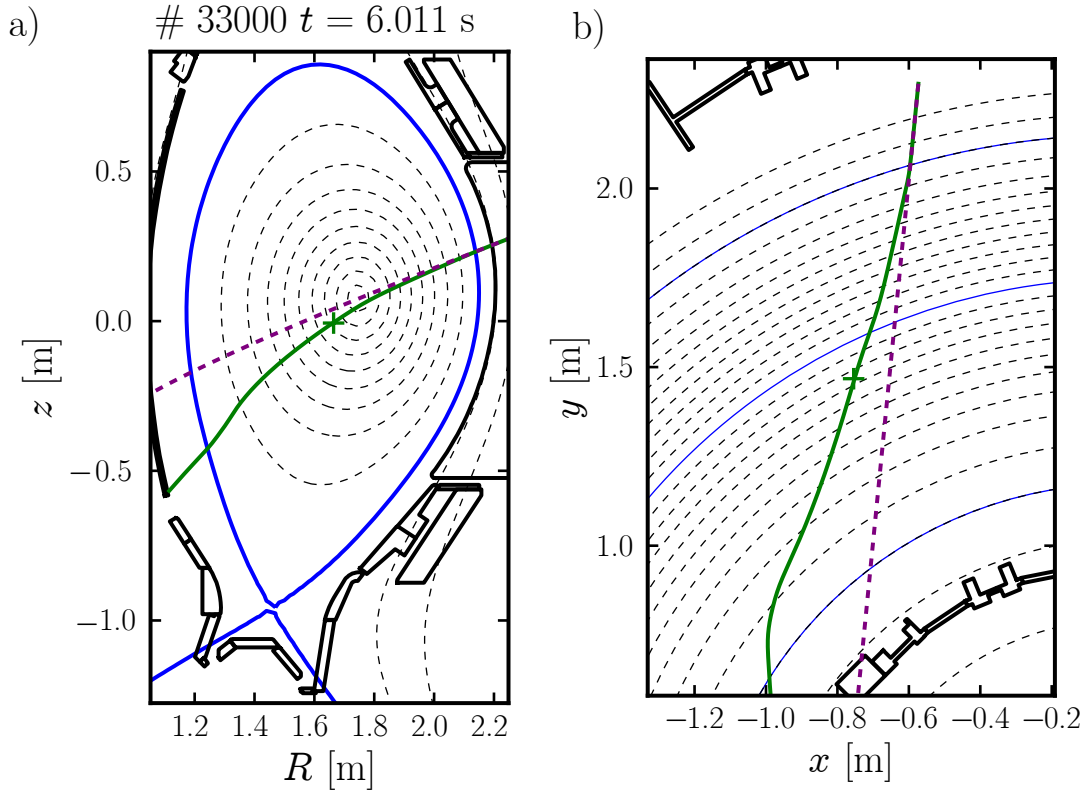

Figure 5.12: The vacuum LOS of the oblique ECE (dashed purple) is compared to the ray obtained with geometrical optics ray tracing (solid green). The cold resonance position on the ray is indicated by the green cross. a) shows the poloidal view and in b) the torus is viewed from the top.

5.4.2 Cross-Calibration method

As explained in 3.2.2 the oblique ECE cannot be easily calibrated and has, therefore, to be cross calibrated on a discharge to discharge basis. As explained in the previous section classical ECE analysis is inapplicable for oblique ECE, which means that radiation transport modeling is required to perform the cross-calibration. The goal of the cross-calibration is to obtain the calibration coefficient C and its estimated uncertainty for each channel. As an intermediate quantity $c(t)$ is introduced which is the time resolved calibration factor defined by

$$T_{\mathrm{rad,mod}}(t) = c(t)\hat{H}(V_{\mathrm{diag}}), \tag{5.1}$$

where V_{diag} is the signal measured by the diagnostic in arbitrary units within a 1 ms window around t. The signal processing is denoted as the functional $\hat{H}$ which produces a single value for all measurements within this time window. The functional $\hat{H}$ consists of three individual steps. First any offset is removed from V_{diag}, then a median filter with kernel size of three is applied and, finally, the signal is averaged. The processed signal shall be denoted as $V^*_{\mathrm{diag}} := \hat{H}(V_{\mathrm{diag}})$. In the ideal case $c(t)$ is time independent and identical to C, but in the experiment this not the case. Because of that the cross calibration coefficient C is obtained through linear regression of $V^*(T_{\mathrm{rad,mod}}) = C_0 + \frac{1}{C} T_{\mathrm{rad,mod}}$. Accordingly, the cross-calibration coefficient C is then the inverse of the slope a of the regression. The statistical error of C is obtained via Gaussian error propagation

$$\Delta C_{\mathrm{stat}} = C^2 \Delta a_{\mathrm{stat}}, \tag{5.2}$$

where Δa_{stat} is the statistical error of a.

The linear regression also yields the offset of the cross-calibration C_0. From C_0 the radiation temperature $T_{\mathrm{rad},0}$ corresponding to $V^* = 0$ can be computed, which should, obviously, be zero. The systematic uncertainty ΔC_{sys} is approximated by the standard-deviation of $c(t)$. The main sources of the systematical uncertainties are propagated uncertainties from the T_{e}, n_{e} profile and the equilibrium. Hence, all channels are affected equally. Accordingly $\Delta C_{\mathrm{sys}}/C$ is averaged over all channels and the resulting average, relative systematic uncertainty is assumed for all channels.

5.4.3 Examples

In the following the cross-calibration for the discharges #33697, #33705 and #34663, which will discussed in detail in the next chapter, is presented. These three discharges were introduced in Section 3.3.

Discharge #33697

The temporal evolution of the cross calibration coefficient $c(t)$ of channel 39 is shown in Fig. 5.13 a). Calibration coefficients were calculated during phases where the plasma current is constant and the radial ECE measurements indicate thermally distributed electrons. For $t > 6.5\,\mathrm{s}$ systematic errors affect the cross calibration significantly. The only remarkable events during this time are the addition of the NBI and a slow decrease of the magnetic field. Since both occur simultaneously it is not clear which of the two is responsible for the temporal evolution of the cross calibration coefficient $c(t)$.

The purpose of the cross calibration is to enable the measurement of absolute T_{rad} during the phases with non-thermal electrons. Of particular interest in this discharge is

a 0.8 s time window around $t = 4.8$ s. Hence, the time window for the cross calibration should be chosen such that the plasma conditions are similar to the ones at $t = 4.8$ s. Since there is no NBI, nor any change of the toroidal magnetic field in this phase it is reasonable to ignore all calibration coefficients for $t > 6.5$ s. Furthermore, the short Ohmic phase before 3 s is also ignored, because it lacks the ECRH present during the non-thermal phase from $t = 3.0$ s to 5.8 s. The remaining time window of the cross-calibration is 5.8 s to 6.5 s. It is shaded green in Fig. 5.13 a).

The linear fit of the calibration coefficient is shown in Fig. 5.13 b). Only the brown calibration factors $c(t)$ lie in the targeted time window and enter into the fit. Including the light blue measurements changes the calibration factor by 30 % which simultaneously introduces a large offset C_0. For the fit with only the brown measurements the offset is zero within the uncertainties of the linear fit ($T_{\mathrm{rad},0} = (45 \pm 4)$ eV).

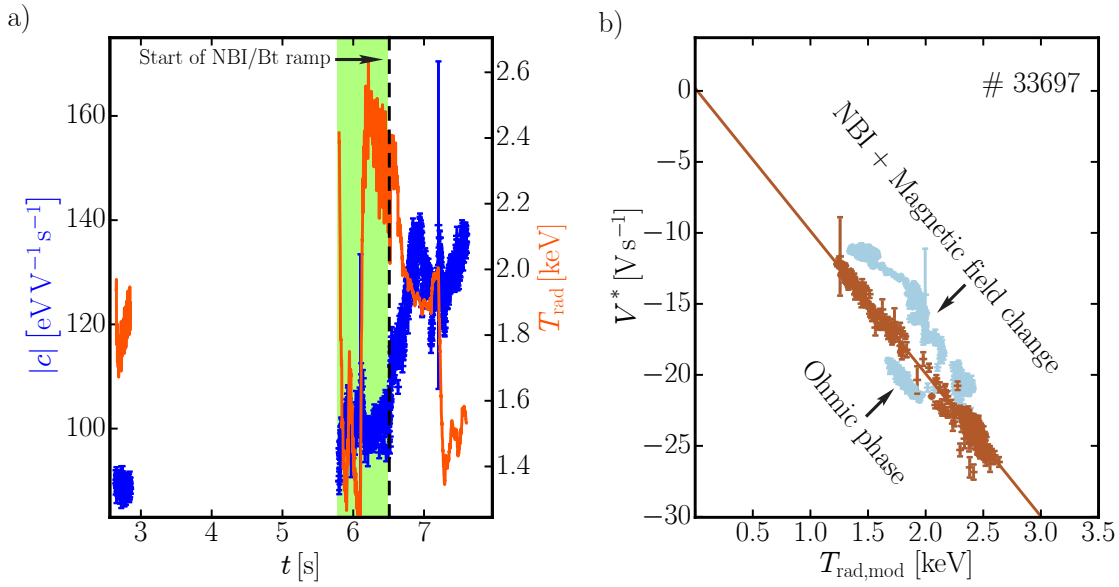

Figure 5.13: a): Temporal evolution of the calibration coefficient $c(t)$ (blue) and the forward modeled $T_{\mathrm{rad,mod}}$ (red). The time points inside the green shaded region are considered in the cross-calibration. b): The processed signal of the diagnostic V^* as a scatter plot and function of $T_{\mathrm{rad,mod}}$. The linear fit (solid line) indicates that the diagnostic response is linear. Only the brown data points (5.8 s to 6.5 s) are considered for the fit.

Discharge #33705

Again the 39th channel is chosen as the representative. The temporal evolution of the cross-calibration is depicted in Fig. 5.14 a). The early phase of the discharge $t < 1.2$ s is not suitable for cross-calibration, because the shape of the plasma still

changes quickly, which reduces the quality of the equilibrium reconstruction. Once the plasma reaches its final shape at $t = 1.2\,\mathrm{s}$ the systematic changes of the cross-calibration coefficient become small. The variation of the cross-calibration coefficients correlates with the switch from a NBI heated to a purely Ohmically heated plasmas as indicated in Fig. 5.14 a). Nevertheless, the changes are small enough to allow a reasonable linear fit of the diagnostic signal against the forward modeled $T_{\mathrm{rad,mod}}$ with a small offset of $T_{\mathrm{rad},0} = (76 \pm 2)\,\mathrm{eV}$. The fit is illustrated in Fig. 5.14 b).

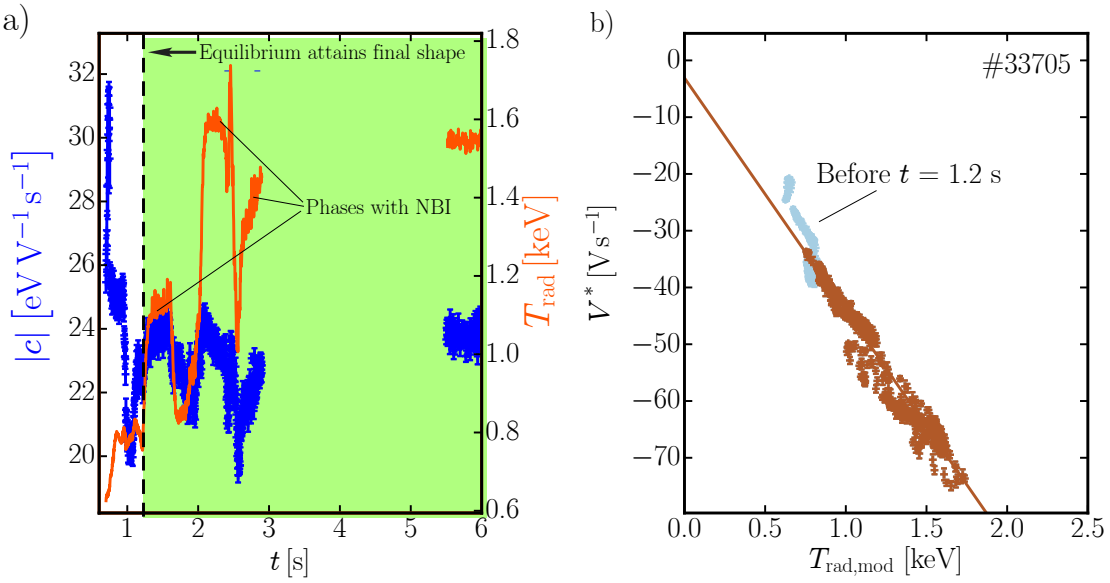

Figure 5.14: Figure a) shows the temporal evolution of the calibration coefficient c (blue) and the forward modeled $T_{\mathrm{rad,mod}}$ (red). The time points inside the green shaded region are considered in the cross-calibration. In Figure b) the signal of the diagnostic U is drawn as a scatter plot and function of $T_{\mathrm{rad,mod}}$. The linear fit (solid line) indicates that the diagnostic response is linear. Only the signals in brown are considered in the fit.

Discharge #34663

This shot features a calibration phase before $< t = 2.9\,\mathrm{s}$ and after $> t = 6.2\,\mathrm{s}$ the phase with active generation of fast electrons. The attenuation of the diagnostic was chosen to be quite high, which means that the signal to noise ratio of the measurements is low. This could not be avoided, because dangerously high microwave intensities due to parametric decay events were observed in the two previous discharges and a safe operation of the diagnostic at lower attenuation could not be guaranteed.

For this shot channel 40 has the best signal-to-noise ratio and was chosen for the illustration of the cross calibration. The cross-calibration factors increase strongly

during the short pulse of a 92 kV NBI beam from 1.35 s to 1.66 s, which can be seen in Fig. 5.15 a). Heating with two beams with a lower acceleration voltage of 35 kV does not produce a large variation of the cross-calibration coefficients. A possible explanation for this behavior could be the generation of a non-thermal distribution due to the high voltage NBI beam, which couples a large fraction of its energy to the electrons. The two beams with the lower voltage are expected to still deposit the majority of their heating power onto the ions. Non-thermal ECE measurements in NBI heated plasmas have been reported at multiple experiments in the past [124]. An alternative explanation could be an erroneous equilibrium reconstruction. This seems less likely since the fast ion distribution induced by NBI was computed with the TRANSP code [107], validated against fast-ion D-alpha measurements [125] and the corresponding fast ion pressure was included in the IDE equilibrium reconstruction.

Except for the time window from 1.35 s to 1.66 s all time points dedicated for the cross calibration are useful. This includes the time window from 6.4 s to 7.0 s, where the toroidal magnetic field strength is decreased from 2.36 T to 2.24 T. Although the data, shown in Fig. 5.15 b), behaves linearly and is well described by the linear fit the systematic error of the calibration factor of 14 % is quite large and so is the offset $T_{\mathrm{rad},0} = (175 \pm 3)$ eV.

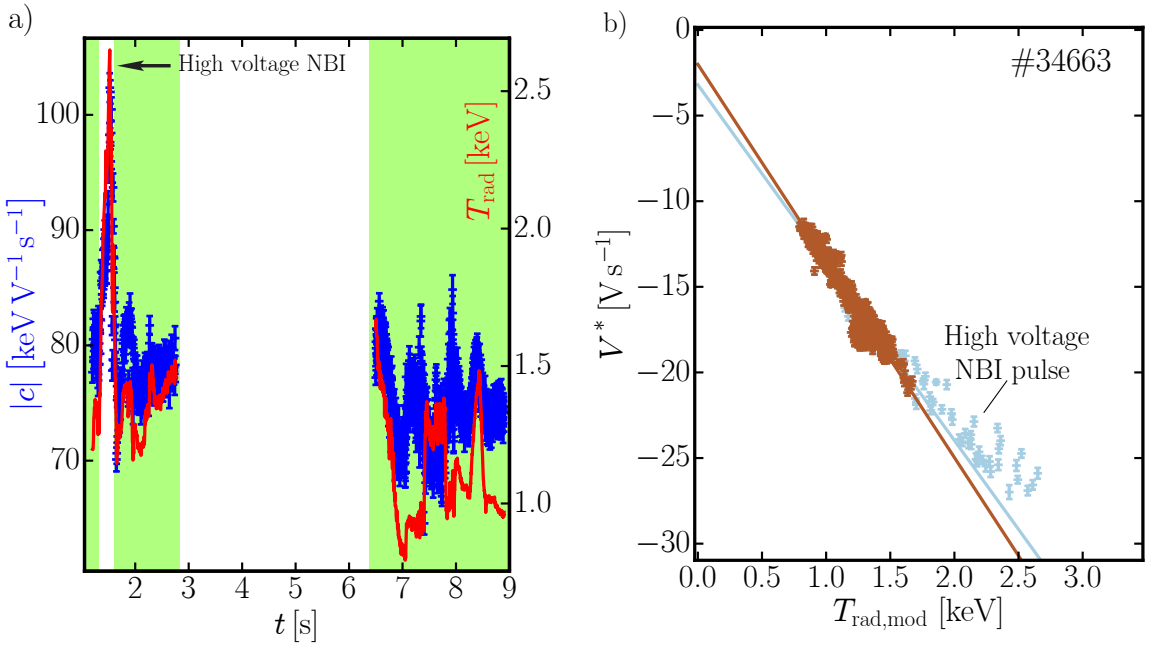

Figure 5.15: Same as Fig. 5.13 but for discharge #34663.

5.5 Further applications of ECRad

One of the main benefits provided by ECRad are the birthplace distributions and the warm resonance positions. This information was particular valuable for the imaging ECE at ASDEX Upgrade. An imaging ECE works like a normal radial ECE but it has many LOS with which is it possible to resolve poloidal structures like MHD modes. For the imaging ECE at ASDEX Upgrade there can be significant deviations between cold and warm resonance positions [112, 126]. Only by mapping to the warm resonance positions, it was possible to determine the poloidal and toroidal mode number of ideal MHD modes during externally applied magnetic perturbations [126, 127].

Furthermore, the T_e profiles reconstructed from ECE measurements with IDA and ECRad were essential to determine the plasma boundary displacement due to magnetic perturbations [128] and for the stability analysis of a field localized ballooning MHD mode [129].

With the synthetic T_rad computed by ECRad it was shown that the imaging ECE at ASDEX Upgrade is sensitive to n_e fluctuations near the plasma edge [130, 131]. Consequently, it can be quite difficult to discern if a modulation of T_rad measured by the imaging ECE is due to n_e or T_e fluctuations [130, 131]. Lastly, by studying the influence of T_e oscillations on the synthetic T_rad it was investigated under which circumstances the radial ECE allows the discrimination between an ideal MHD mode and a neoclassical tearing mode [132].

With conventional ECE diagnostics it is not possible to resolve the T_e fluctuations caused by turbulence due to thermal noise. This limitation can be overcome by correlating the ECE measured at two slightly different frequencies. In this case one speaks of correlation ECE. With correlation ECE, it is possible to validate the turbulent T_e fluctuations predicted by gyrokinetic calculations performed with codes like the GENE code [133]. To compare the fluctuations predicted by GENE with measurements of the correlation ECE, a synthetic ECE diagnostic is needed[13]. Currently, the synthetic ECE diagnostic of the GENE code does not consider radiation transport and, therefore, the radial resolution of the diagnostic has to be obtained with codes like ECRad [13]. Attempts were made to pair ECRad with GENE, but numerical issues with the GENE electron distribution functions arising at high electron velocities halted these efforts. Lastly, ECRad guided an ensuing upgrade of the ASDEX Upgrade correlation ECE diagnostic [13, 134].

5.6 Conclusions

The code ECRad was compared to a previous electron cyclotron radiation transport model used for standard plasma scenarios at ASDEX Upgrade. Only ECRad is capable of describing the ECE measurements in the plasma edge and SOL region correctly for plasmas with a core temperature of $T_e > 7\,\mathrm{keV}$. Further benefits of ECRad over the previous model were highlighted for two plasma scenarios and the limitations of ECRad arising at very low optical depth were discussed. ECRad extends the pool of plasma scenarios that can be evaluated reliably within the routine IDA.

As described in Section 4.2, ECRad includes cold plasma geometrical optics raytracing and a fully relativistic absorption coefficient considering cold plasma dispersion for wave polarization and the refractive index. The relativistic Maxwell-Jüttner distribution is the most important new ingredient for describing properly the shine-through of heavily down-shifted emission from relativistic electrons in the plasma core. In addition, the effect of the radiation reaction force on the high-energy tail of the electron distribution function and its consequence for the ECE measurement was investigated analytically and numerically. No significant effect on the modeled T_{rad} was found for the scenarios discussed. The influence of wall reflections was identified as a plausible explanation for the residual discrepancy which remains between measured and modeled T_{rad} at extremely low optical depth. It was investigated if second harmonic O-mode emission can be used to determine T_e in discharges where the X-mode is in cut off. This is found to be not feasible because of the large influence of wall reflections on the measurements which arise due to the low optical depth of second harmonic O-mode emission at ASDEX Upgrade. The influence of O-mode emission on the routine ECE measurements at ASDEX Upgrade was investigated. Assuming that only X-mode emission contributes to the ECE spectra overestimates the modeled T_{rad} by 5 % to 10 % at ASDEX Upgrade.

The improved radiation transport model is applied to two plasma scenarios which constitute special cases from the perspective of ECE. The "pseudo-radial displacement" observed for large core T_e gradients is correctly accounted for by the model. The successful reconstruction of T_e profiles from ECE measurements containing a mixture of second and third harmonic emission is demonstrated. Supplementing the ECE data with Thomson scattering data in the IDA framework helps to recover regions which are not covered properly by the ECE data alone.

The challenges in the analysis of oblique ECE caused by refraction and the Doppler shift were discussed. With ECRad these challenges can be overcome and it is possible to cross-calibrate an oblique ECE diagnostic. The results of the cross-calibration were discussed for three scenarios.

Aside of the inference of T_e and the cross-calibration of oblique ECE diagnostics ECRad is also a useful tool in the study of MHD and turbulent fluctuations. For MHD

fluctuations ECRad assists in the precise localization of the mode and the discrimination between ideal MHD modes and magnetic islands. For turbulent studies ECRad provides the birthplace distribution which is essential for the benchmark between the results of gyrokinetic calculations and correlation ECE measurements.

In summary, ECRad considerably improves the accuracy of T_e profile reconstruction and extends the overall operational space of ECE diagnostics. Due to the robust and fast implementation ECRad is applicable for routine analysis in the everyday ECE data interpretation.

6 Analysis of non-thermal ECE spectra during ECCD

In the last chapter thermal electron distribution functions were assumed for the interpretation of the ECE measurements. This approximation is appropriate for the majority of the discharges performed with ASDEX Upgrade. However, in low n_e experiments ECE spectra arise occasionally, which cannot be explained by a thermal distribution function. Particularly interesting are cases where microwave heating is applied at low n_e, because there the non-thermal features in the ECE spectra can be reproduced reliably.

For the interpretation of non-thermal ECE spectra, where any possible, unanticipated problem of ECRad can hardly be identified, the careful validation of ECRad against the ECE spectra of thermal plasmas is very valuable. For these verification-tests the IDA framework provides the ideal platform. It allows a redundant set of measurements to be considered, which greatly assists the detection of possible errors or limitations of the synthetic diagnostic. Furthermore, the automation allows to use large data sets and, therefore, a wide variety of scenarios to be considered. Since no inconsistencies were found, aside of the difficulties arising at low optical depth due to wall reflections, it is expected that ECRad is suitable for the first quantitative analysis of non-thermal ECE spectra.

The distribution functions discussed in this chapter are modeled with the bounce-averaged Fokker-Planck code RELAX [135], a state-of-the-art tool for the assessment of the current drive efficiency of ECCD. This approach is quite usual. In past work the Fokker-Planck codes CQL3D [34], LUKE [33], and RELAX [135] were used to explain ECE measurements during intense ECCD (e.g. Refs. [6, 7, 136]). The present work is the first study where oblique ECE measurements are considered in the validation of Fokker-Planck calculations of ECCD. Furthermore, as presented in the previous chapter, the ECRad code has been extensively verified against the experimentally observed ECE of thermal plasmas, which was not done for the radiation transport codes employed in previous studies [6, 7, 137].

In past work conducted at the TCV tokamak it was shown that radial particle and heat transport have a strong influence on the electron distribution function [138]. A smaller, but still non-negligible influence of radial transport on the distribution function was detected at DIII-D [37]. In this work it is investigated to what extent

ECE measurements can contribute to the quantification of radial diffusion.

This chapter is structured into five sections. First, the benchmark scenarios are discussed and the validity of RELAX and ECRad is demonstrated for the case of low levels of ECRH power. Then it is shown that for the present experiments the agreement between actual and synthetic ECE measurements is poor if the same simplifications as in Ref. [6, 7] are made, i.e. that the ECRH absorption only occurs on a single harmonic and the observed ECE spectrum is approximated as pure X-mode. To understand the discrepancies, the phase space sensitivity of the ECE measurements is investigated in Section 6.3. It is explained that the finite width of the VOS, ECRH absorption at the third harmonic and O-mode emission can be important for the interpretation of the ECE due to non-thermal distribution functions. In section 6.4 the loop voltage and the radiation reaction force are incrementally added to the Fokker-Planck calculations to test the sensitivity of ECE on these effects. Section 6.5 shows a sensitivity study of ECE on an empirical radial diffusion model. The most important results are summarized in Section 6.6.

6.1 Preparation and validity check of the RELAX and ECRad calculations

Extensive information on the plasma and the ECRH waves is required to compute the non-thermal distribution with RELAX (see Section 2.6). Since these input quantities critically affect the result, great care is required in obtaining them. To compute the trajectory of the ECRH beam and the linear power deposition profile, the T_e and n_e-profiles and the magnetic equilibrium are required. The first part of this section addresses how these quantities are computed and it is discussed why the particular approach is chosen. In the second part of this section the validity of the RELAX calculations is demonstrated in case of low ECRH power, where the distribution remains thermal. This allows the direct comparison of RELAX against linear ECRH beam tracing codes like TORBEAM [45]. Furthermore, it is verified that ECRad performs correctly for the numerical distribution function data provided by RELAX.

6.1.1 Kinetic profiles as input for RELAX

While, the T_e cannot fully describe the distribution in non-thermal plasmas, a T_e profile that represents the bulk of the distribution function, is nevertheless, required for the computation of the truncated collision operator (see Section 2.6). This approach is sensible for the discussed scenarios, where only a minority of the electrons are non-thermal, while the majority of the electrons follows a thermal distribution for

which the T_e profile is still meaningful. The T_e and n_e profiles are determined with the IDA method. For n_e lithium beam emission spectroscopy, plasma interferometry and Thomson scattering measurements are considered. For T_e ECE and Thomson scattering measurements are taken into account. As will be explained later, the ECE measurements with cold resonance positions $\rho_{pol,res} > 0.6$ could be contaminated by the down-shifted emission from non-thermal, highly energetic electrons and, consequently, only ECE measurements with $\rho_{pol,res} < 0.6$ are considered. In the following the T_e profiles of the three scenarios introduced in Section 3.3 are briefly discussed. The focus in Section 3.3 was on the time traces of the discharges. This section presents the analysis of the profiles of a single time window for each discharge.

Discharge #33697 at $t = 4.8\,s$

Discharge #33697 features a steady state phase which lasts 0.8 s centered around $t = 4.8\,s$. During this phase the ECE measurements do not change significantly except for a small modulation due to an ideal kink mode located in the plasma center ($\rho_{pol} > 0.25$). The modulation of the ECE measurements caused by the mode is treated as an uncertainty, since the mode cannot be included in the computations with RELAX. For the profiles, measurements within a time window of 1 ms around $t = 4.8\,s$ are considered for all diagnostics, except for the Thomson scattering diagnostic where all measurements during the entire 0.8 s time window are taken into account. The T_e and n_e profiles and the considered ECE and Thomson scattering measurements care illustrated in Fig. 6.1. Good agreement between T_e profile and Thomson scattering measurement is found in the region where ECE and Thomson scattering overlap. The forward modeled $T_{rad,mod}$ match the measured T_{rad}.

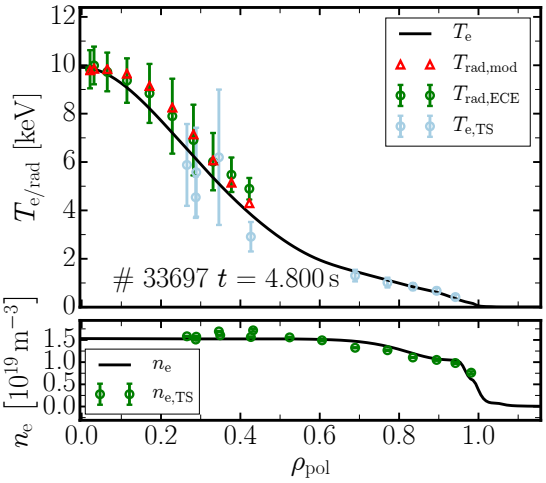

Figure 6.1: The figure shows the T_e and n_e profiles attained with the IDA method for #33697, $t = 4.8\,s$. The ECE and Thomson scattering measurements considered for the profiles and the forward modeled $T_{rad,mod}$ are also depicted.

To calculate the electron-ion collision term the effective ion charge Z_{eff} is required. It can be determined from the bremsstrahlung measured with charge exchange recombination spectroscopy. For this discharge and the time window considered here $Z_{eff} = 3.2$.

For ASDEX Upgrade this is quite large, which is most likely due to the poor condition of the upper divertor at the time of the experiment.

Discharge #33705 at $t = 4.9\,\mathrm{s}$

In this discharge n_e decays continuously in the phases with significant amounts of fast electrons (c.f. Fig. 3.6 a)). However, since the change in n_e occurs slowly it is adequate to assume that the distribution is in equilibrium at each time point. Because of the change of the plasma parameters, the time window of useful Thomson scattering measurements is just 50 ms around $t = 4.9\,\mathrm{s}$. Like in #33697, there is an ideal kink mode in this discharge. Its modulation of T_rad is again interpreted as a source of uncertainty. The T_e and n_e profile from IDA are shown in Fig. 6.2 a). The effective ion charge in this discharge is $Z_\mathrm{eff} = 2.0$. This experiment were executed on the day after discharge #33697 was carried out. In between discharges #33697 and #33705 several other USN discharges were executed leading to a much better condition of the upper divertor and, consequently, a lower impurity content of the plasma.

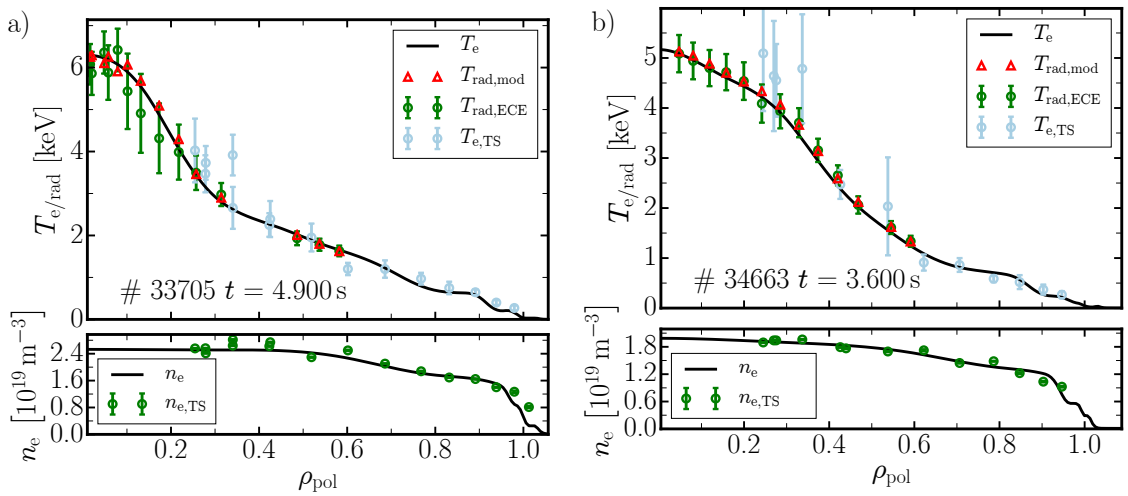

Figure 6.2: Figure a) shows the T_e and n_e profile attained with the IDA method for #33705 $t = 4.9\,\mathrm{s}$. The ECE and Thomson scattering measurements considered for the profile and the forward modeled $T_\mathrm{rad,mod}$ are also depicted. Figure b) shows the same, but for #34663 $t = 3.6\,\mathrm{s}$.

#34463 $t = 3.6\,\mathrm{s}$

Similar to #33705 this discharge does not have a long steady state phase due to a continuous change of n_e (c.f. Fig. 3.6 b)) and it has to be assumed that the distribution

Discharge #	time window [s]	core T_e [keV]	core n_e [$\times 10^{19} m^{-3}$]	Z_{eff}
33687	4.0 to 5.6	10.0	1.5	3.2
33705	4.85 to 4.95	6.2	2.4	2.0
34663	3.2 to 4.0	5.2	2.1	2.0

Table 6.1: The most important parameters of the three discussed time slices are listed.

function reaches equilibrium despite the increase of n_e. The increase of n_e during the phase of co-ECCD is slow enough to allow the inclusion of the Thomson scattering measurements within a 400 ms time window centered around $t = 3.6$ s in the IDA. The resulting profiles are depicted in Fig. 6.2 b). Here the effective ion charge is also $Z_{eff} = 2.0$. In Table 6.1 the most important parameters of the three discussed scenarios is listed.

6.1.2 Geomtrical vs. quasi-optical beam tracing

The evaluation of the quasi-linear diffusion operator requires the trajectory and wave vector spectrum of the ECRH beam. Since RELAX does not have an internal ray tracing code, this information has to be provided by a linear beam tracing code. In this work the quasi-optical linear beam tracing code Gray [46] was chosen for this purpose. Unlike the geometrical optics approach discussed in Section 2.2 the quasi-optical method includes diffraction additionally to refraction.

For the highly focused, millimeter wavelength beams of gyrotrons diffraction is an important effect as it limits the beam waist to a finite width of about 2 cm in case of vacuum dispersion. In the geometrical optics approach diffraction is neglected and the beam waist is zero at the focus point and as a direct consequence the power density diverges. This poses a serious problem for the quasi-linear calculation of the power deposition which has to be solved by artificially defocusing the ECRH beam, similarly to the approach used in ECRad. By using a quasi-optical ECRH beam tracing code the beam width is computed consistently.

As discussed in Ref. [139], the $N_\parallel$ spectrum of the beam also plays an important role for ECCD. As explained in Chapter 2, $N_\parallel$ determines the region in which the wave and the electrons are resonant. A finite beam divergence means that the $N_\parallel$ spectrum has a finite width. Accordingly, the resonance line in momentum space for a single radial position (c.f. Fig. 2.3) is in reality a resonance band. While the beam width cannot be treated consistently with geometrical optics, the computed $N_\parallel$ spectrum is correct. For quasi-optical codes, on the other hand, the beam is perfectly paraxial at the beam waist and the $N_\parallel$ spectrum is a Dirac delta function [46]. Accordingly, there is no resonance broadening. This is incorrect, because even at the beam waist a Gaussian beam still

has a finite divergence [139]. As demonstrated in Ref. [139] the $N_{||}$ spectrum can be directly adjusted/corrected in RELAX, which is why Gray [46] was chosen over a ray tracing code like TORAY-FOM [47, 48].

6.1.3 Configuration and validation of the GRAY calculations

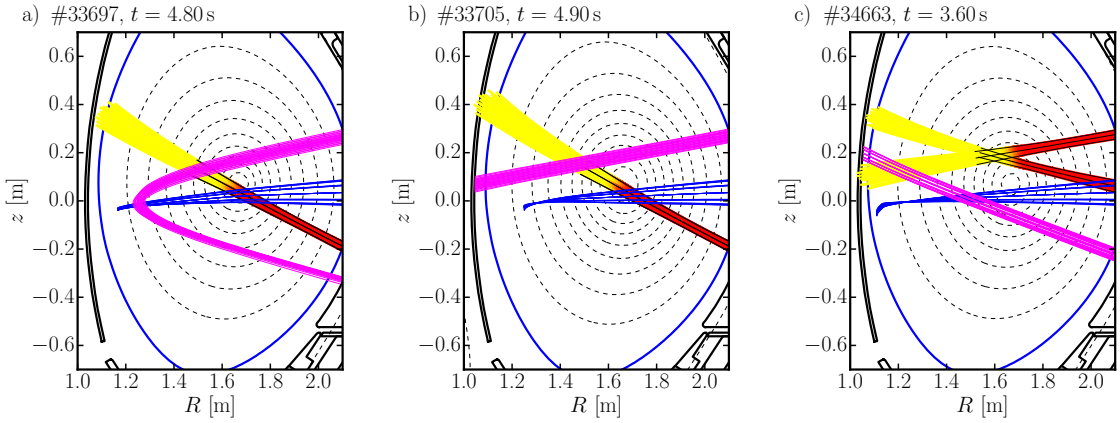

Figure 6.3: Trajectory of the ECRH beams and the volume of sight geometry of the radial (blue) and oblique ECE diagnostic (magenta) as computed by ECRad for the three scenarios: a) #33697, b) #33705 and c) #34663. The path of the ECRH beams is calculated twice, once by TORBEAM and once by Gray, The beam shape computed by Gray is illustrated using a red to yellow color map, where red means the individual ray is at its initial power and yellow corresponds to no power. The TORBEAM central and peripheral rays are indicated via the black lines.

Since new methods for the management of the input data for the GRAY and RELAX calculations had to be developed, the beams obtained from Gray are benchmarked against the beams obtained with TORBEAM [45], the latter being already well-established at ASDEX Upgrade. TORBEAM is a linear, quasi-optical code like GRAY. However, unlike GRAY, TORBEAM uses an expansion of the eikonal equations [45], which greatly reduces the computational cost, since only one central ray and two beam widths describing the elliptical beam shape need to be considered. Nevertheless, GRAY and TORBEAM are expected to deliver the same results.

The configuration of the ECRH launchers and the launcher used for the oblique ECE is summarized in Tables 6.2 to 6.4. The resulting poloidal and toroidal projection of the ECRH beams and the volume of sight of the radial and oblique ECE diagnostic for the discharges #33697, #33705, and #34663 are shown in Figs. 6.3 to 6.5. The dashed black lines depict the central and peripheral rays computed by TORBEAM and the peripheral rays indicate the $1/e^2$ beam width. The rays from Gray are color

	Launcher no.	Power [MW]	pol. angle θ [°]	tor. angle ϕ [°]
Gyrotron 1	7	0.66	25.0	19.9
Gyrotron 2	8	0.65	25.0	19.8
Oblique ECE	6	–	-10.1	29.9

Table 6.2: Configuration of the launchers for the ECRH and the oblique ECE for #33697 at $t = 4.8\,\mathrm{s}$. The launcher number and the toroidal and poloidal launch angle follow the default convention used in ASDEX Upgrade.

coded according to the intensity of the rays. Red means the power of the ray is at its initial value and yellow means all power has been absorbed. The beams in Gray are discretized into rays using polar coordinates for the beam cross-section. For the calculations in this work seven radial times 25 angular grid points are considered for the beam cross section, which sums up to a total of $6 \times 25 + 1 = 151$ rays per beam. The large ray number is necessary to avoid aliasing effects when calculating the power deposition, the driven current profile and the distribution function with RELAX. The rays are distributed such that the outermost rays lie at the $1/e^2$ power density of the beam. This assures high resolution in the region of the highest power densities and also eases the comparison of the beam shapes between Gray and TORBEAM. Widening the grid beyond $1/e^2$ increases aliasing without causing significant broadening of the power deposition or ECCD profile. The beam trajectories and shapes agree very well with each other. The comparison of the power deposition and ECCD profiles calculated Gray and TORBEAM can be found in Fig. 6.6. Additional to the ECRH beams the volumes of sight of the oblique and radial ECE are shown in Figs. 6.3 and 6.5. The volumes of sight are discretized into a rectangular, five by five grid. The blue rays depict the LOS of the radial ECE and the magenta rays correspond to the oblique ECE.

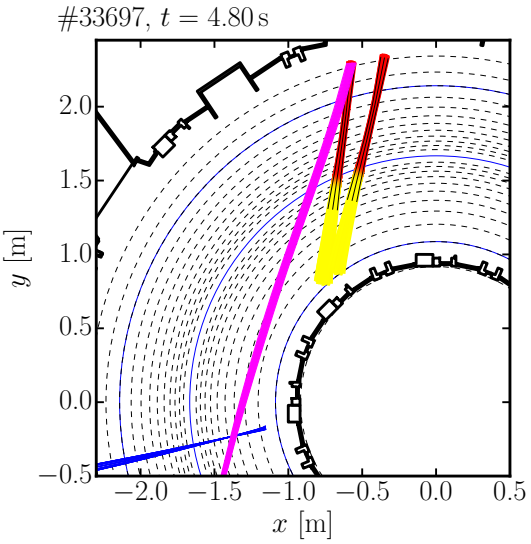

Figure 6.4: Same as Fig. 6.3, but for a top view and #33697 only.

	Launcher no.	Power [MW]	pol. angle θ [°]	tor. angle ϕ [°]
Gyrotron 1	7	0.54	25.0	19.9
Gyrotron 2	8	0.64	25.0	19.8
Oblique ECE	6	–	-10.1	-19.9

Table 6.3: Same as Table 6.2 but for #33705 and $t = 4.9\,\mathrm{s}$.

	Launcher no.	Power [MW]	pol. angle θ [°]	tor. angle ϕ [°]
Gyrotron 1	2	0.52	11.4	-19.9
Gyrotron 2	5	0.52	-9.1	-19.9
Oblique ECE	6	–	19.0	20.0

Table 6.4: Same as Table 6.2 but for #34663 and $t = 3.6\,\mathrm{s}$.

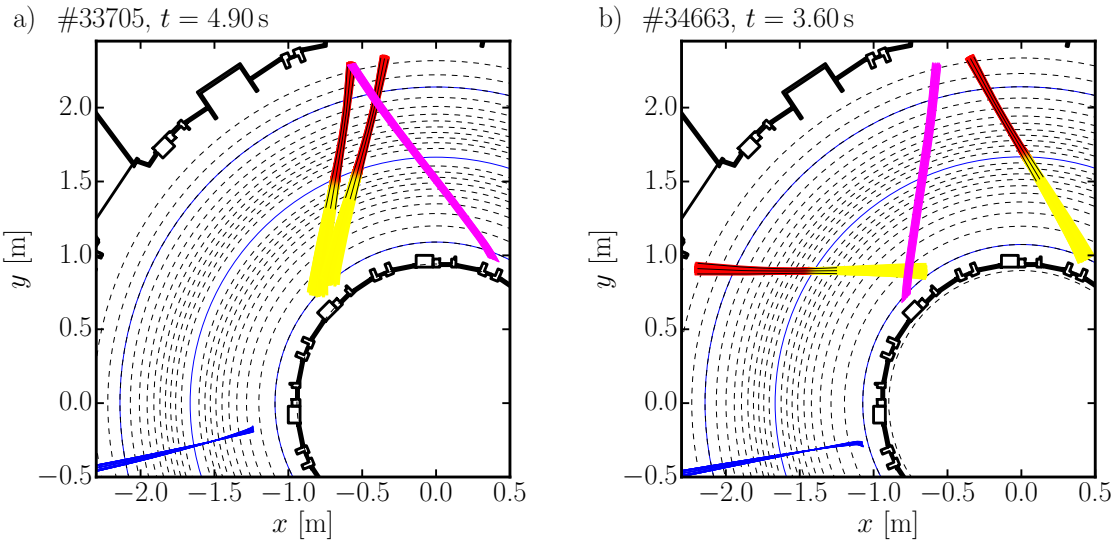

Figure 6.5: Same as Fig. 6.4, but for #33705 and #34663.

6.1.4 Validation of RELAX and ECRad in case of linear damping

Once the beam trajectory and wave vectors are obtained it needs to be correctly communicated to RELAX. To validate the information transfer and check the validity of a quasi-linear Fokker-Planck code it is common practice to benchmark the results against a linear code in the case of low ECRH power, where any deformation of the distribution function is too small to affect the electron cyclotron damping process and the linear treatment is expected to yield the same results as a quasi-linear calculation.

For the test run 1 kW of power was distributed evenly across the two beams used in discharge #34663. In the top graph of Fig. 6.6 the power deposition and driven current profiles obtained from Gray, RELAX and TORBEAM are shown. As expected, the power deposition profile calculated by RELAX lies very close to the GRAY profile. The TORBEAM and Gray power deposition profiles also match. Interestingly, the profiles of the driven current do not agree perfectly. RELAX predicts the largest driven current and Gray the smallest. The mismatch in the driven current between TORBEAM and Gray is especially peculiar, because the two codes use two different implementations of the same momentum conserving model for the driven current [140, 141] and were benchmarked against each other numerously, e.g. in Ref. [142]. The discrepancies between Gray/TORBEAM and RELAX are also difficult to understand since the linearized current drive models used in Gray and TORBEAM should yield the same results as the full Fokker-Planck treatment in case of low input power. An exception to this is trapping of electrons caused by the ECRH which is not accounted for in the linear models. However, trapping should only cause a reduction of the driven current for the discussed scenario and can, therefore, be ruled out as an explanation for the discrepancies, here. Since the accuracy of the linear models is not relevant for the present work and, out of the three codes, RELAX provides the most sophisticated treatment for the ECCD, it is assumed that the driven current predicted by RELAX is accurate and the observed discrepancy will be subject to future work.

The bottom graph of Fig. 6.6 compares the initial T_e and n_e profiles with the "non-thermal" $T_\mathrm{e,RELAX}$ and $n_\mathrm{e,RELAX}$ profiles derived from the RELAX distribution function profile. These two quantities are defined as the norm of distribution function times the initial n_e profile ($n_\mathrm{e,RELAX}$) and

$$T_\mathrm{e,RELAX} := \frac{c_0^2 m_\mathrm{e}}{3 n_\mathrm{e,non\text{-}th}} \iint \frac{\sqrt{u_\perp^2 + (u_\parallel - \langle u_\parallel \rangle)^2}}{\gamma} f(u_\perp, u_\parallel) 2\pi u_\perp \mathrm{d}u_\perp \mathrm{d}u_\parallel \tag{6.1}$$

which is analogous to the definition of T_e for thermal distributions. The parallel drift

velocity $\langle u_\parallel \rangle$ is

$$\langle u_\parallel \rangle := \frac{1}{n_{\mathrm{e,RELAX}}} \iint u_\parallel f(u_\perp, u_\parallel) 2\pi u_\perp \mathrm{d}u_\perp \mathrm{d}u_\parallel. \tag{6.2}$$

All quantities use the same notation as in Chapter 2.

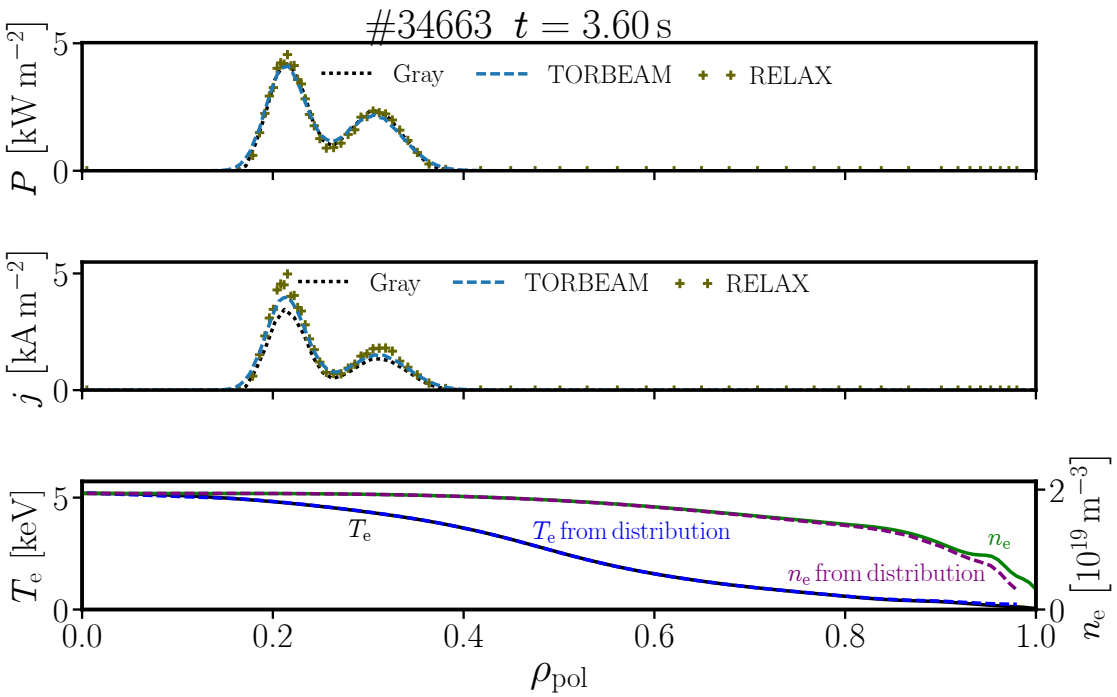

Figure 6.6: Power deposition profiles calculated by Gray, RELAX and TORBEAM (top) and driven current profiles (middle) for an injected power of 1 kW. Bottom graph: Initial T_e and n_e profiles and $T_\mathrm{e,RELAX}$ and $n_\mathrm{e,RELAX}$ obtained from the RELAX distribution function.

With the distribution function profile from RELAX the forward modeled T_rad can be calculated with ECRad. In the case of just 1 kW of injected power it is of course expected that the forward modeled $T_\mathrm{rad,mod}^\mathrm{RELAX}$ computed with the RELAX distribution do not deviate significantly from $T_\mathrm{rad,mod}^\mathrm{therm.}$ derived from the thermal distributions. This is also a verification test, because the distribution function profile computed by RELAX is given on a grid which ECRad has to interpolate.

Figure 6.8 a) compares $T_\mathrm{rad,mod}^\mathrm{RELAX}$ with $T_\mathrm{rad,mod}^\mathrm{therm.}$ for #34663 and $t = 3.60\,\mathrm{s}$. Only synthetic measurements with an optical depth $\tau_\omega > 0.1$ are depicted. The relative deviation between the two T_rad is indicated by the olive (radial ECE) and gray (oblique ECE) crosses. All deviations are below 3 %, which is much smaller than the estimated uncertainties of the measurements.

6.2 Basic calculations with RELAX and ECRad

Starting point of the analysis of the non-thermal ECE spectra are the methods presented in Refs. [6, 7]. For the Fokker-Planck modeling this means that only a single harmonic $n = 2$ is taken into account in the quasi-linear diffusion operator. Furthermore, radial transport, the loop voltage and the radiation reaction force are neglected. This is slightly different from the approach of Ref.[6], where the loop voltage was included despite being suspected to be irrelevant for the non-thermal ECE.

The resulting power deposition, driven current, $T_{\mathrm{e,RELAX}}$ and $n_{\mathrm{e,RELAX}}$ profiles shown in Fig. 6.7 for discharge #34663. In this calculation the experimentally measured ECRH power of 1.0 MW is considered. The shape of the power deposition and driven current profiles computed by TORBEAM and Gray are unaffected by the increase in power, because both codes have a linear power response. Also the power deposition profile computed by RELAX is only insignificantly affected. The driven current computed by RELAX is, however, much larger indicating that the electron cyclotron absorption is non-linear. Since n_{e} is fixed in the RELAX calculation the initial n_{e} and $n_{\mathrm{e,RELAX}}$ match,except for the outermost radial point, where the boundary condition of RELAX introduces some discrepancies. There is a considerable difference between $T_{\mathrm{e,RELAX}}$ and the initial T_{e} inside the region of significant power deposition. This is another indicator that ECRH renders the distribution function non-thermal.

For the ECE modeling it is assumed that the measured spectrum is pure X-mode ECE and the volume of sight can be represented by a single ray, which are the same assumptions as in [6, 7]. In the ECE modeling the harmonics $n = 2$ to 5 are considered. Figures 6.8 b) and 6.9 compare the synthetic T_{rad} in case of a thermal and the RELAX distribution to the measurements of the radial and the oblique ECE for the three scenarios from Section 6.1.1. For the oblique ECE the dark cyan error bars indicate the standard deviation obtained from the averaging over a 1 ms interval. For every fifth measurement the estimated systematic uncertainty of the calibration is indicated by the light blue error bars. The quality of the match between forward modeled T_{rad} and the measurements varies among the three scenarios. In case of #33697 the model can explain neither the measurements of the radial ECE for $\rho_{\mathrm{pol,res}} > 0.5$ nor any of the oblique ECE measurements. The synthetic T_{rad} always underpredict these measurements. For discharge #33705 the agreement between synthetic and measured T_{rad} is reasonable for the oblique ECE, but for the radial ECE discrepancies arise for $\rho_{\mathrm{pol}} > 0.5$. The synthetic T_{rad} again tend to be smaller than the measurements. For #34663 the systematic uncertainty of the oblique ECE measurements is quite large and the synthetic T_{rad} fall within one standard deviation of the measurements. Unlike in the two previous cases the synthetic T_{rad} matches the measurements of the radial ECE surprisingly well near the plasma edge.

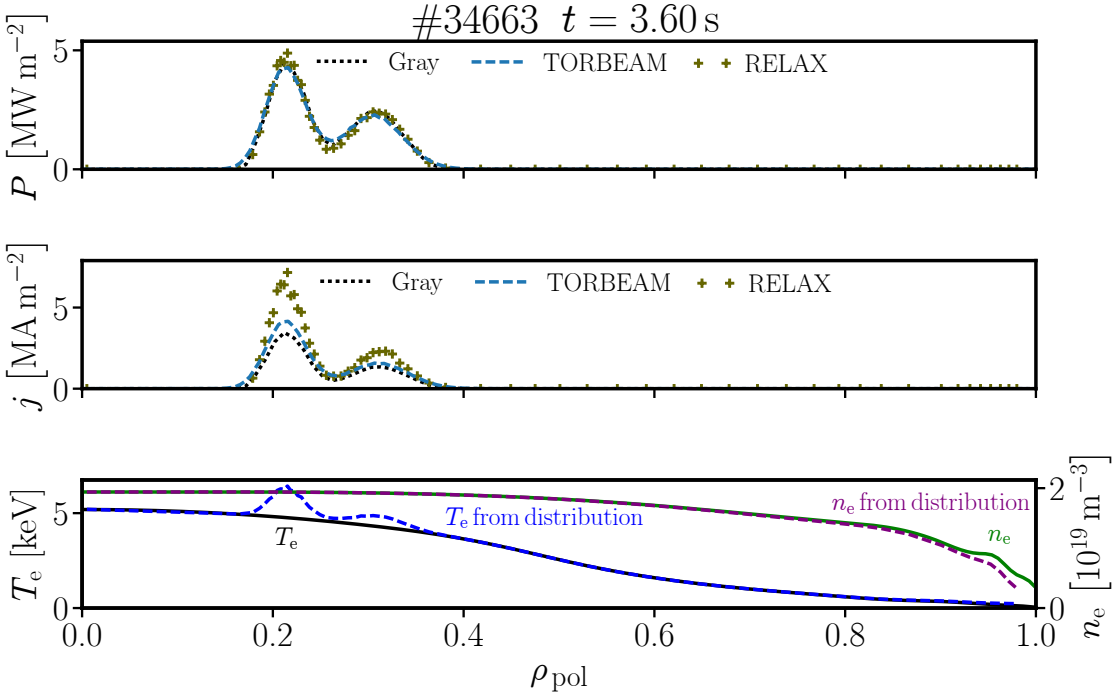

Figure 6.7: Same as Fig. 6.6 but for the experimentally applied power of 1 MW.

6.3 Phase space sensitivity of ECE

To identify the insufficiencies in the modeling it is necessary to determine the phase space sensitivity of the two diagnostics. With this knowledge it is possible to identify the regions in phase space, where the distribution function modeled by RELAX deviates from the experimentally observed distribution function.

6.3.1 Oblique ECE

One advantage of the oblique ECE diagnostic at ASDEX Upgrade is the great flexibility of the viewing geometry. This allowed measurements directly at the site where the ECRH deposits its power and slightly outside this region.

Measurement at the deposition site of the ECRH

In #34663 the ECRH and the oblique ECE diagnostic were optimized such that their resonances in phase space lay as close together as technically feasible. In Fig. 6.11 a) the power deposition of the individual beams and the power deposition of both beams as computed by RELAX are shown. These profiles are compared to two birthplace

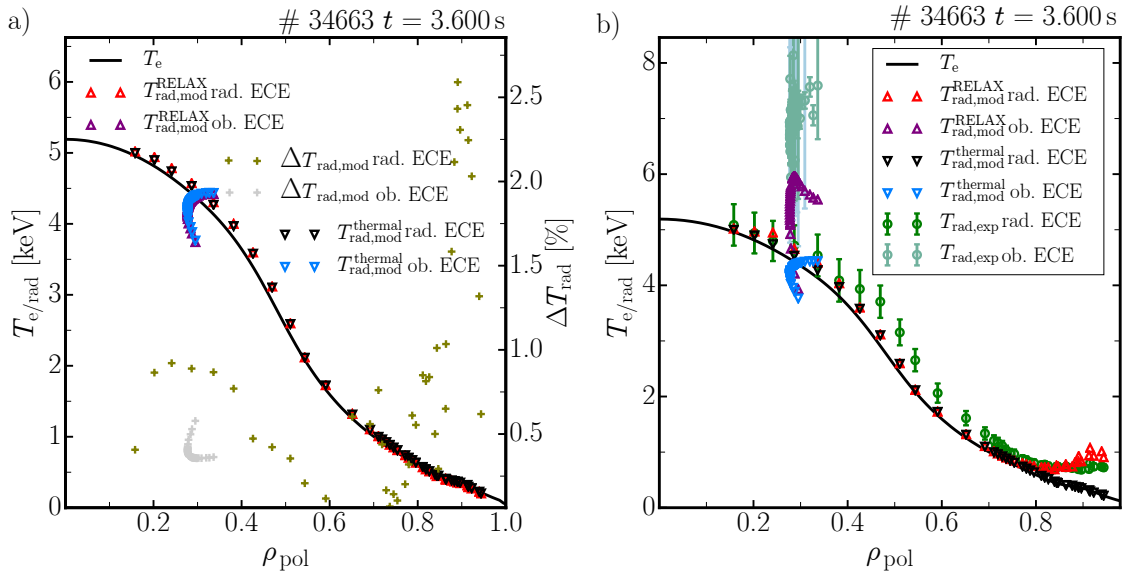

Figure 6.8: a) Comparison of the $T^{f_{\mathrm{RELAX}}}_{\mathrm{rad,mod}}$ (red/purple triangles for the radial/oblique ECE diagnostic) derived from the RELAX distribution function profile for an injected power of 1 kW with the $T^{f_{\mathrm{MJ}}}_{\mathrm{rad,mod}}$ (black/light blue upside-down triangles for the radial/oblique ECE diagnostic) for the T_e profile (black line). The relative deviation $\Delta T_{\mathrm{rad,mod}}$ between the two T_{rad} is indicated by the right y-axis (olive/grey crosses for radial/oblique ECE diagnostic). b) Comparison of $T^{f_{\mathrm{RELAX}}}_{\mathrm{rad,mod}}$ derived from the RELAX distribution profile given realistic ECRH power and $T^{f_{\mathrm{MJ}}}_{\mathrm{rad,mod}}$ for a thermal distribution with the ECE measurements. The measurements of the radial ECE and their error bars are indicated by the green markers. For the oblique ECE the measurements and its statistical error are depicted by cyan markers. For every fifth measurement the systematical uncertainty due to the cross-calibration is indicated by a light blue error bar.

distributions of observed intensity for a channel of the oblique ECE diagnostic. The birthplace distribution indicated by the blue line is computed for a singular ray, while a rectangular bundle of 5×5 rays is considered for the birthplace distribution depicted by the blue crosses in Fig. 6.11 a). The discontinuities in the birthplace distribution considering the ray bundle are an aliasing effect. To remove them, it would be necessary to strongly increase the number of rays considered in ECRad from 25 to probably around 151 rays which are required in Gray to achieve smooth power deposition profiles.While the aliasing is visible in the birthplace distribution, increasing the number of rays slightly to 36 has no significant effect on the forward modeled T_{rad}. Hence, the large computational effort required to produce smooth birthplace distributions is omitted, here.

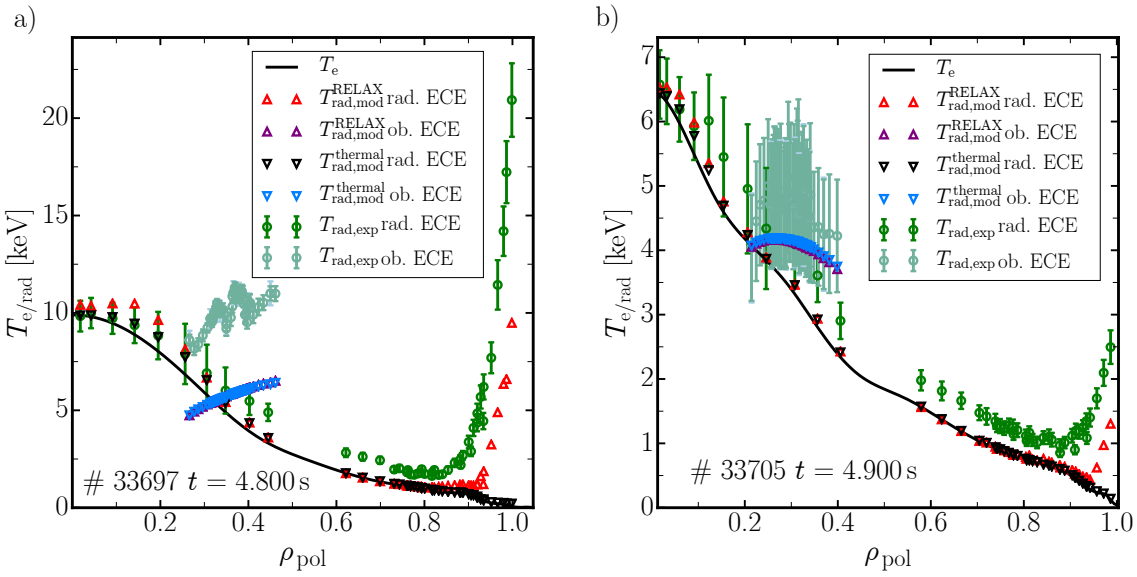

Figure 6.9: Same as Fig. 6.8 b) but for a) #33697 at $t = 4.8\,\mathrm{s}$, and b) #33705 at $t = 4.9\,\mathrm{s}$

The overlap of the ECRH deposition and the oblique ECE sensitivity in momentum space is illustrated in Fig. 6.11 b). The blue to green color shaded lines indicate three cuts of the two-dimensional birthplace distribution of the oblique ECE. The three chosen radial positions are indicated in a) by the blue vertical, dot dashed lines. Only two vertical lines are visible since two of them overlap. The two-dimensional power deposition profiles of the two ECRH beams are indicated similarly in b), but a pink to yellow color map is used instead. The radial positions considered for each cut of the 2D power deposition profile are marked by pink/red vertical dotted lines. The 2D power deposition profiles and the birthplace distribution ECE have their maxima at very similar momenta. Consequently, the oblique ECE diagnostic is sensitive to the area in momentum space, where the ECRH is de-

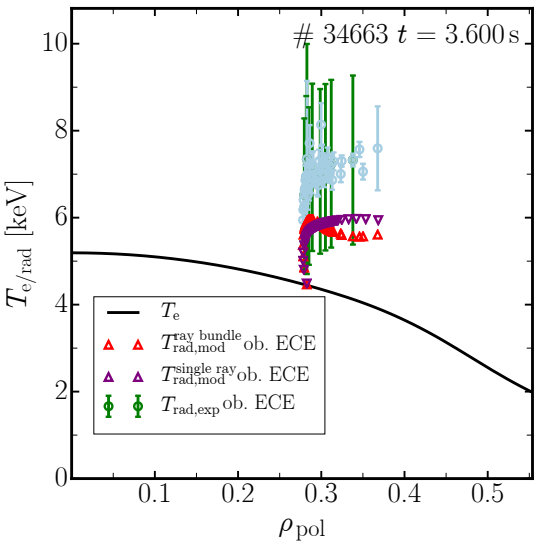

Figure 6.10: Comparison of T_{rad} without (red triangles) and with a finite width VOS (purple upside down triangles) for the oblique ECE and discharge #34663.

positing its power. The contours in b) correspond to the decadic logarithm of the distribution function at the radial location where the birthplace distribution in a) has its maximum. The distribution function is identical to the one considered for the T_{rad} shown in Fig. 6.9 b). The contours are slightly elliptical, indicating that the distribution function is non-thermal.

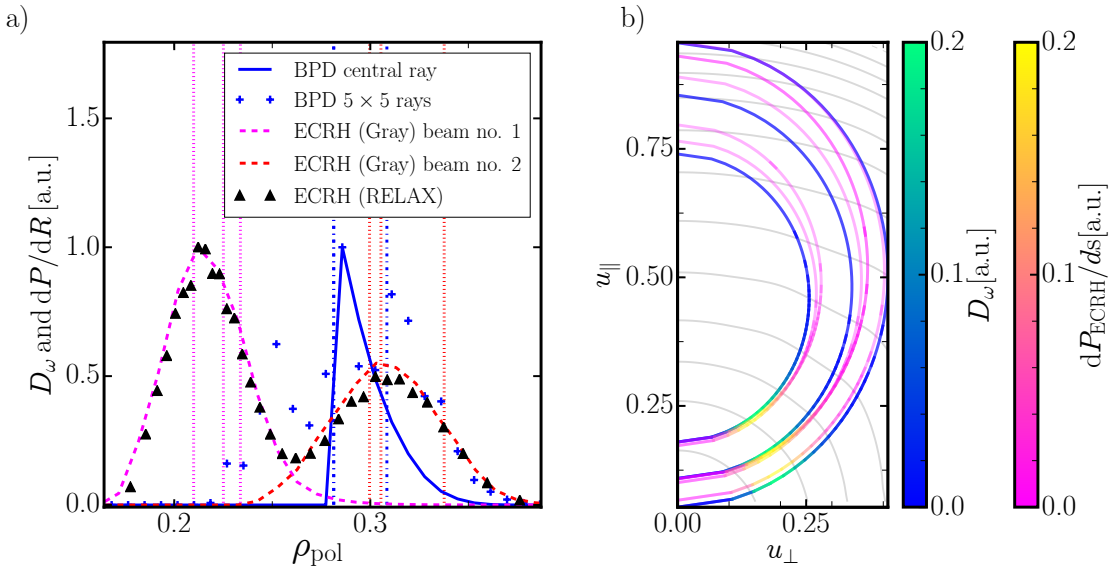

Figure 6.11: a) shows the power deposition profile of the two individual ECRH beams and the one computed by RELAX given the combined power of both beams. Furthermore, the birthplace distribution function for the central ray of the oblique ECE (blue solid line) and the birthplace distribution that results if the finite width of the volume of sight is included (blue crosses), are shown. b) shows resonance lines in momentum space. The green to blue color coded resonance lines correspond to the oblique ECE while the pink to yellow resonance lines are for the ECRH. The color indicates the magnitude of the two-dimensional birth place distribution or power deposition profile. The position of the resonance lines of the ECRH (oblique ECE) are marked by the vertical pink/red dotted (blue dash-dotted) lines. b) also shows the contours (black, thin lines) of the distribution function at the maximum of the birthplace distribution.

The birthplace distribution accounting for the ray bundle in Fig. 6.11 a) is wider and extends further inward as its counter part that considers only a singular ray. It also has a larger overlap with the power deposition profiles of both beams. While the finite width of the volume of sight could be disregarded in the ECE analysis of thermal plasmas, this is not the case here. In Fig. 6.10 the oblique ECE measurements for $t = 3.60\,\mathrm{s}$ and two sets of forward modeled T_{rad} are shown. The shape of the forward modeled T_{rad} agrees much better with the measurements if the finite width of the volume of sight is

considered. Since the shape of the synthetic and measured spectrum agree very well with each other it is likely that the residual discrepancy is due to a systematic error in the cross-calibration. Since there is a clear distinction between LOS and VOS here, the 5×5 ray bundle is considered for all scenarios discussed in the following.

Measurement outside the deposition range of the ECRH

In #33697 and #33705 the oblique ECE was aligned such that it measured at positions slightly outside of the deposition site of the ECRH (c.f. Fig. 6.3). The radial and momentum space sensitivity of the diagnostic is shown in Fig. 6.12 for discharge #33705. The radial birthplace distributions are very similar in the two discharges, but the resonance lines in phase space differ greatly. In Fig. 6.12 b) the resonance lines of the ECRH and the oblique ECE lie close together. Despite that, there is no actual overlap in phase space as the radial displacement between birthplace distribution and power deposition profile in Fig. 6.12 a) indicates. Hence, here the oblique ECE diagnostic is sensitive to non-thermal electrons that diffused radially outwards from the deposition site of the ECRH.

In discharge #33697, as depicted in Fig. 6.13 b), the oblique ECE diagnostic is sensitive to the second harmonic emission of electrons with $u_{\parallel} > 0$, while electrons with $u_{\parallel} < 0$ are resonant to the ECRH. Hence, the two resonances lie on opposite sides of the $u_{\parallel}$ plane. Additional to the resonance lines corresponding to the second harmonic, also the resonance lines of the third harmonic are drawn for the ECRH in Fig. 6.13 b). The resonance line of the second harmonic of the oblique ECE intersects with the third harmonic resonance line of the ECRH. Hence, the oblique ECE could be sensitive to the non-thermal electrons created by third harmonic absorption, which has been neglected so far. Of course to be visible to the diagnostic the electrons affected by third harmonic absorption have to first diffuse outside of the deposition site into the region where the oblique ECE is sensitive (c.f. Fig. 6.13 a)).

6.3.2 Radial ECE

For the radial ECE one has to distinguish between channels that do have a cold resonance position inside the plasma and those that do not. The former might be sensitive to shine-through of non-thermal emission originating from the plasma core some of which is reabsorbed near the cold resonance. For the latter there is no reabsorption at the cold resonance and all observed intensity is non-thermal shine-through.

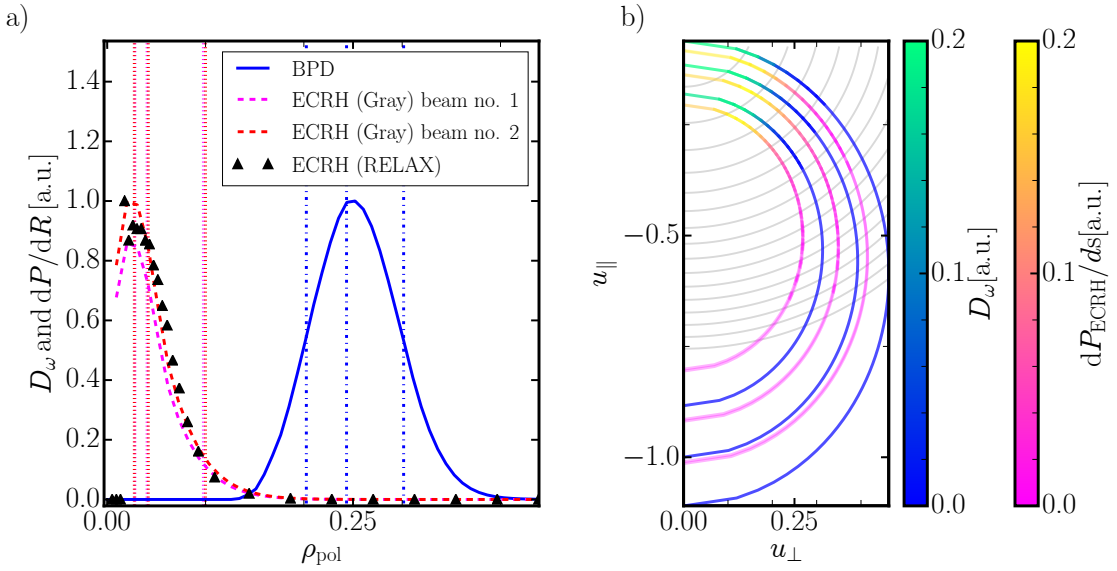

Figure 6.12: Same as Fig. 6.11, but for #33705.

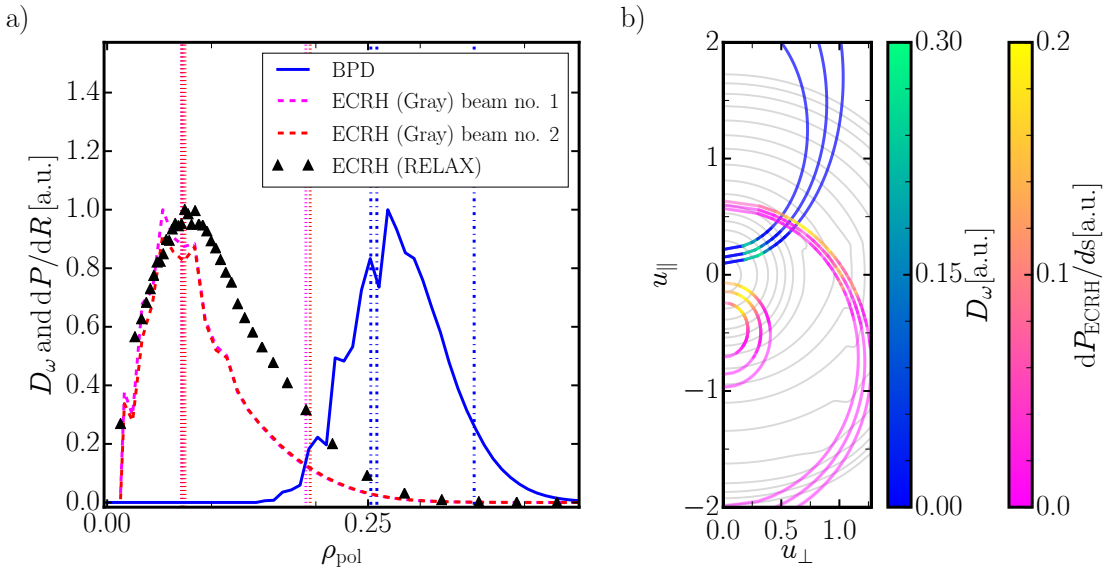

Figure 6.13: Like Fig. 6.11, but for #33697. Figure b) also shows the resonance lines corresponding to third harmonic absorption/emission.

Cold resonance position outside the confined region

Figure 6.14 a) shows a one dimensional birthplace distribution. Despite aforementioned aliasing of the distribution it is clear that all emission is due to the non-thermal electrons located in the plasma core, where the ECRH deposits its power. There is no direct overlap of the ECRH and the radial ECE in phase space, as is shown in Fig. 6.14 b). The resonance line of the ECE lies at much large momenta than the one of the ECRH. This means that the ECE is only indirectly sensitive to the ECRH, because of the generation of a highly energetic tail in the distribution function.

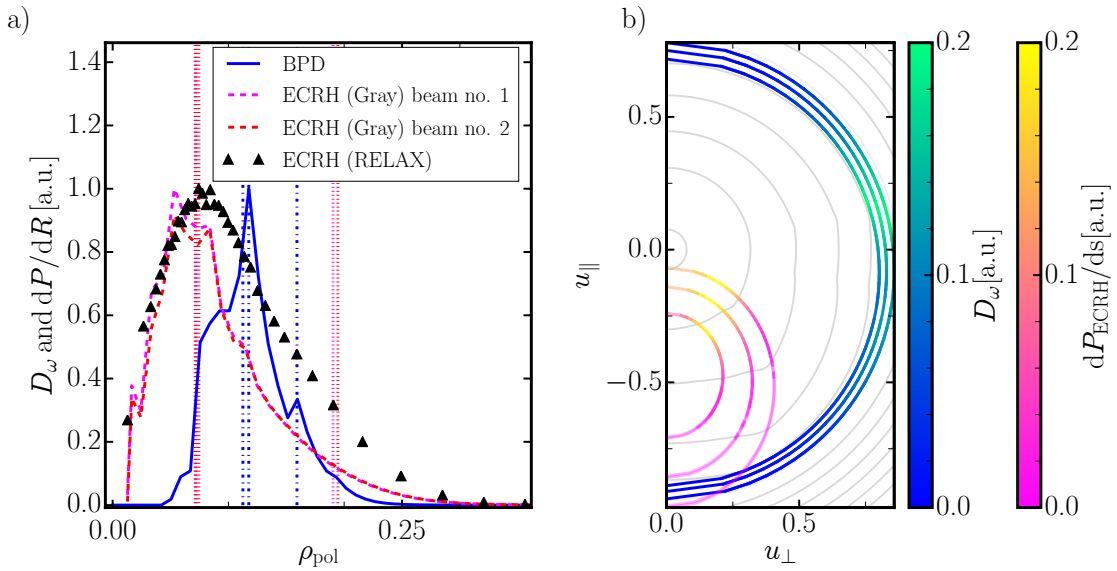

Figure 6.14: Like Fig. 6.11 but for discharge #33697 and the radial ECE. The considered ECE channel is highlighted in Fig. 6.9 a).

This picture changes drastically if absorption at the third harmonic is considered in the RELAX calculation. In Fig. 6.15 a) three cuts of the resulting, two dimensional birthplace distribution are shown for the three radial positions marked by vertical, dash-dotted, blue in Fig. 6.14 a). The $n = 3$ resonance lines of the ECRH, depicted in Fig. 6.15 a), intersect with the second harmonic resonance lines of the ECE. The maximum of the birthplace distribution lies at momenta different from the ones in Fig. 6.14 b). As shown by the distorted contours in Fig. 6.15 a), the distribution function is strongly non-thermal near the $n = 3$ absorption site.

Given the two-dimensional power deposition profile for the third harmonic it is also expected that the inclusion of the third harmonic absorption reduces the total driven current slightly. Simultaneously it increases the radiation temperatures measured by

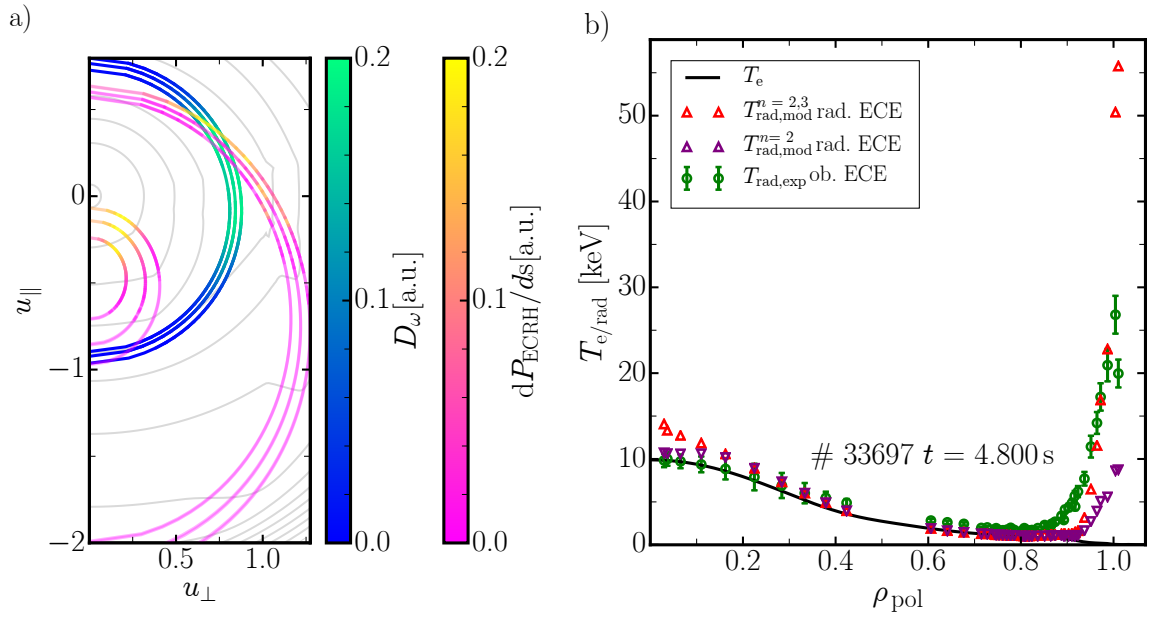

Figure 6.15: a) Same as Fig. 6.11 b) for discharge #33697 but the third harmonic absorption of the ECRH is included and the radial ECE is considered. b) Comparison of the radiation temperatures with and without absorption at the third harmonic in the RELAX calculation.

the radial ECE with cold resonance positions near the plasma edge. This is illustrated in Fig. 6.15 b), where the synthetic radiation temperatures shown in Fig. 6.9 a) are compared to the T_{rad} profiles that result if third harmonic absorption is included.

Interestingly, the addition of third harmonic absorption in RELAX also increases T_{rad} at cold resonance positions near the plasma center. As will be shown in the next subsection, second harmonic emission that originates from the immediate vicinity óf the cold resonance position is emitted by low energetic electrons. At these energies the distribution function predicted by RELAX is very close to thermal equilibrium. Simultaneous to the second harmonic emission there is, however, also third harmonic emission, which is caused by highly energetic electrons. With the inclusion of third harmonic absorption in RELAX the third harmonic emission affects the synthetic measurements.

This is in conflict with the assumption made in the beginning of this chapter which says that the ECE measurements near the plasma core can be interpreted as thermal emission and, therefore, allow the determination of T_e. This can be reconciled when a low level ($< 0.1\,m^2/s$) of radial diffusion is included in the RELAX calculations which reduces the synthetic T_{rad} of the radial ECE near the magnetic axis back to the level expected from a thermal plasma. Hence, the increase of T_{rad} near the plasma core in

Fig. 6.15 b) is just an artifact of the simplified calculations.

Cold resonance position inside the confined region

Inside the confined region reabsorption near the cold resonance is strong for X-mode emission at ASDEX Upgrade. This is indicated in Fig. 6.16 a), where the X-mode transmissivity is plotted as a function of the cold resonance position assuming a thermal plasma for #33697. For $\rho_{\mathrm{pol,res}} < 0.8$ the total transmisivity $T = 0$, because the plasma layer enclosing the cold resonance is optically thick and any X-mode emission that occurs at positions that lie further away from the antenna is reabsorbed. Contribution of X-mode emission due to non-thermal electrons located in the plasma core is only possible for the channels with $\rho_{\mathrm{pol,res}} > 0.8$, for which $T > 0$. However, large discrepancies between the T_e profile inferred from the Thomson scattering diagnostic and the ECE measurements occur for $\rho_{\mathrm{pol,res}} > 0.6$ in #33697 (c.f. Fig. 6.9 a)). In the following three hypotheses for this are proposed and their merits are discussed:

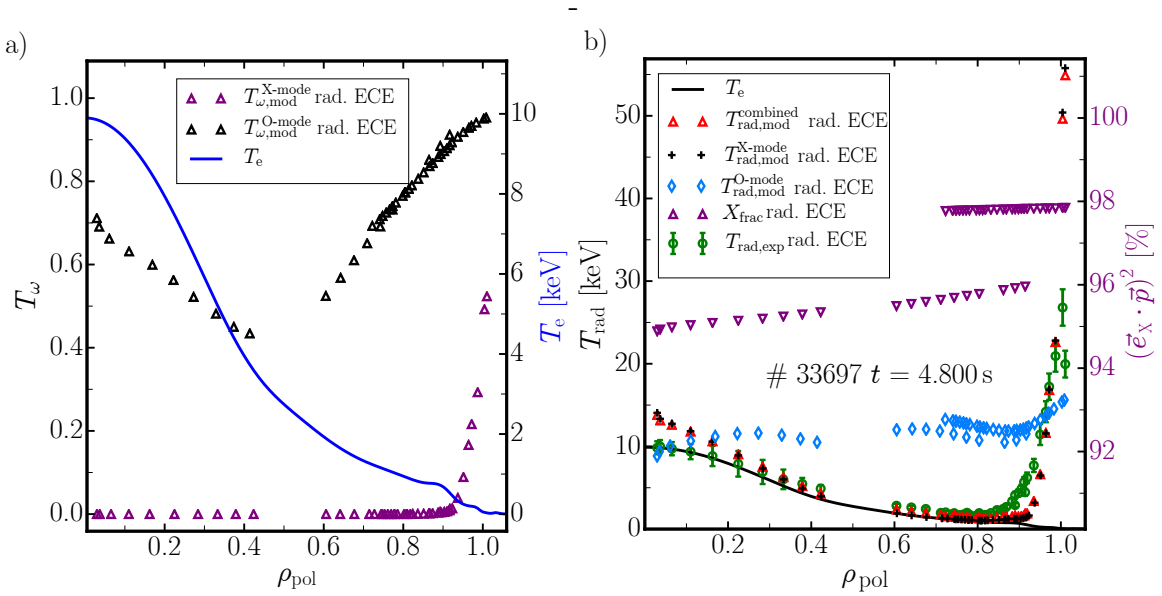

Figure 6.16: a) The X- and O-mode transmissivity T_ω are compared for the radial ECE and #33697 at $t = 4.80\,\mathrm{s}$. b) Simulated O-mode, X-mode and the corresponding,superimposed radiation temperatures are compared. The efficiency of the polarizer is indicated by the purple triangles.

1: Momentum space sensitivity near the cold resonance

Since the calculations in Section 6.2 were carried out without any radial diffusion and the

amount of power deposited by the ECRH is negligible for $\rho_{\mathrm{pol,res}} > 0.45$ (c.f. Fig. 6.14 a)) a thermal distribution is assumed in the calculations for $\rho_{\mathrm{pol,res}} > 0.45$. Figure 6.17 a) shows the two-dimensional birthplace distribution as contours (c.f. Section 2.5) for #33697 and the ECE channel with $\rho_{\mathrm{pol,res}} = 0.62$. Second harmonic X-mode emission is assumed. Here, unlike in Section 2.5, ρ_{pol} is chosen as the radial coordinate. For this channel, mode and harmonic all observed emission is caused by low energetic electrons ($u < 0.2$). Hence, in order for hypothesis 1 to be correct the distribution has to be non-thermal at low energies. This, however, is very unlikely because of the extremely high collisionality in this energy range and the lack of any driving force towards a non-thermal distribution at this position. While highly energetic electrons generated in the core diffuse outwards [42], their energy is insufficient to affect the distribution significantly at low energies. To conclude: Hypothesis 1 is unlikely, because of the large amount of power necessary to sustain any deformation of the distribution at small electron velocities.

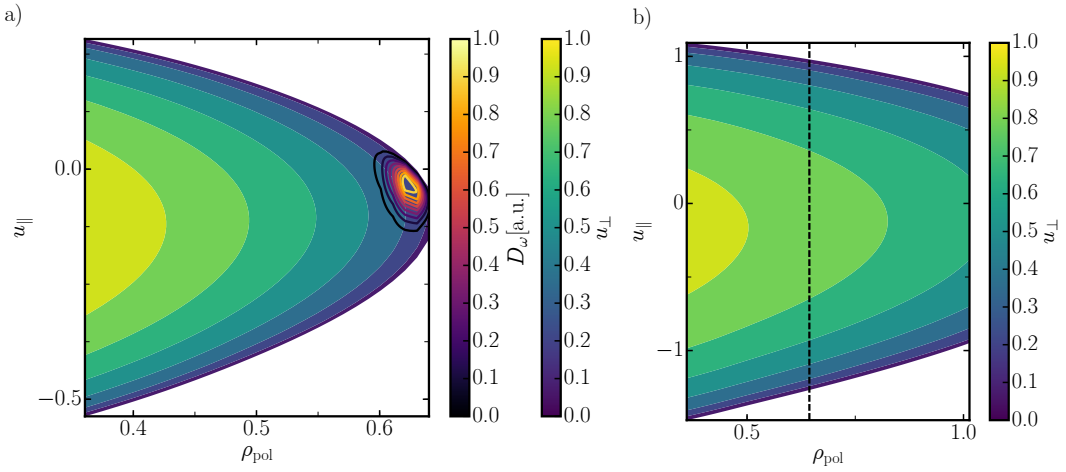

Figure 6.17: a) The figure shows the 2D birthplace distribution for discharge #33697 and a channel with $\rho_{\mathrm{pol,res}} = 0.6$. b) Like a) but for third harmonic emission.

Hypothesis 2: Third harmonic emission near the plasma edge

The tip of the cone in Fig. 6.17 a) at $\rho_{\mathrm{pol}} = 0.64$ marks the radial point closest to the antenna at which electrons can still fulfill the resonance condition for the second harmonic. The resonance plain for the third harmonic is shown in Fig. 6.17 b). It extends across $\rho_{\mathrm{pol}} > 0.64$, which means that emission at higher harmonics is possible at these positions. Since there is no resonance to the second harmonic for $\rho_{\mathrm{pol}} > 0.64$ the radiation due to higher harmonics is not subject to reabsorption if it occurs on the LFS and $\rho_{\mathrm{pol}} > 0.64$. To contribute to the measurements the electrons need to have

large momenta $u > 0.6$ as indicated in Fig. 6.17 b).

Hence, a hypothetical high energy tail near the plasma edge could affect the measured T_{rad}. Non-thermal electron experiments conducted at TCV did not indicate the presence of such a tail [42]. Nevertheless, if radial diffusion is included a small tail tends to form in the distribution functions computed by RELAX. Hence, in ECRad emission and absorption of harmonics $n \in \{2, 3, 4, 5\}$ are included in the calculations.

Hypothesis 3: Non-thermal O-mode emission
The O-mode has a much smaller absorption coefficient than the X-mode, especially at low T_{e} [43]. Figure 6.16 a) shows the transmisivity of the O-mode given thermally distributed electrons and the scenario #33697. Reabsorption is extremely small for all channels meaning that almost the entire non-thermal O-mode emission from the core reaches the antenna. Figure Fig. 6.16 b) shows the O-mode, X-mode and the superimposed T_{rad} spectrum as well as the efficiency of the polarizer. Here the distribution function is the same as in Fig. 6.15. The O-mode T_{rad} is much larger than the X-mode T_{rad} for $0.6 < \rho_{\mathrm{pol}} < 0.9$ which increases the T_{rad} of the combined spectrum slightly. Since reabsorption is negligible for O-mode emission at ASDEX Upgrade the O-mode spectrum contains information that is not accessible through the radiometry of the X-mode emission. Simultaneously the low optical depth renders the O-mode ECE very susceptible to wall reflections.

In conclusion. even in case of a thermal plasma it was not possible to interpret the O-mode emission with ECRad (see Section 5.2.3). Hence, in the more complex case of non-thermal plasmas the only reasonable option is to discard all measurements where a significant contribution by O-mode emission is suspected. This affects all measurements of the radial ECE and $\rho_{\mathrm{pol,res}} > 0.6$ in #33697 and #33705, as they show signs of a significant O-mode contribution. For the radial ECE measurements in #34663 the O-mode contributions seem negligible, most likely because the off-axis deposition of the ECRH in #34663 yields only a much smaller amount of highly energetic electrons than the on-axis deposition in #33697 and #33705.

6.4 Parallel electric field and radiation reaction force

So far the only drive towards a non-thermal distribution was electron cyclotron damping. In the following the importance of the parallel electric field and the radiation force for the equilibrium distribution function and the resulting ECE is discussed.

Discharge	I_{exp} [kA]	$I_{\mathrm{ECCD+E_{\parallel}}}$ [kA]	$I_{\mathrm{E_{\parallel}}}$ [kA]	I_{ECCD} [kA]	I_{syn} [kA]
#33967	524	520	648	−224	96
#33705	488	487	620	−172	39
#33721	375	376	249	111	16

Table 6.5: Table summarizing the experimentally measured current minus the bootstrap current I_{exp}, $I_{\mathrm{ECCD+E_{\parallel}}}$, $I_{\mathrm{E_{\parallel}}}$, I_{ECCD} and I_{syn} for the three discussed scenarios.

6.4.1 Parallel electric field

Depending on whether co- or ctr-ECCD is used the parallel electric field that sustains the plasma current either synergizes or anti-synergizes with the quasi-linear electron cyclotron diffusion. In the following the influence of the parallel electric field on the co-ECCD in discharge #34663 at $t = 3.60\,\mathrm{s}$ is discussed. Since an accurate measurement of the loop voltage profile is difficult, a flat loop voltage profile has to be assumed. The parallel electric field used as input in RELAX is given by the loop voltage divided by the major radius of the outer most point of the flux surface. The loop voltage given to RELAX is varied until the measured plasma current of the experiment is reproduced. The currents achieved with only ECCD (I_{ECCD}), with ECCD and the parallel electric field ($I_{\mathrm{ECCD+E_{\parallel}}}$) and with only the parallel electric field ($I_{\mathrm{E_{\parallel}}}$) are compared to the experimentally measured plasma current in Table 6.5. Since the bootstrap current is not computed by RELAX the values for the plasma current listed in Table 6.5 are the measured plasma current minus the bootstrap current estimated by IDE. The last column in Table 6.5 shows $I_{\mathrm{syn}} \equiv I_{\mathrm{ECCD+E_{\parallel}}} - I_{\mathrm{E_{\parallel}}} - I_{\mathrm{ECCD}}$, which indicates the magnitude of the non-linear interaction between parallel electric field and ECCD. For counter ECCD a positive I_{syn} means anti-synergy and, accordingly, for co-ECCD this indicates synergy. In all three scenarios the interaction between ECCD and the parallel electric field is non-negligible. In #33697 the anti-synergy is especially strong and the parallel electric field reduces the ECCD efficiency by about 40 %.

Figure 6.18 a) compares T_{rad} corresponding to the RELAX distribution with and without loop voltage for #34663. Near the plasma edge the synthetic ECE measurements are slightly larger in the case that includes the loop voltage. This is expected since in discharge #34663 parallel electric field and ECCD synergize. As Fig. 6.18 a) shows the parallel electric field has an important effect on the ECE measurements and, therefore, it is included in all scenarios discussed in the following.

6.4.2 Radiation reaction force

Even though the radiation reaction force had a negligible influence effect on the ECE measurements of thermal plasmas, it is possible that it is relevant for non-thermal distributions, where a large contribution by highly energetic electrons is expected. This hypothesis is tested by including the radiation reaction force into the RELAX calculation presented in the previous section, i.e. ECRH absorption at the second and third harmonic plus the loop voltage. Figure 6.18 b) compares T_{rad} that include the radiation reaction force to the case where it is neglected. The effect of the radiation reaction force is negligibly small for all measurements. Nevertheless, it will be included in the calculations presented in the following section.

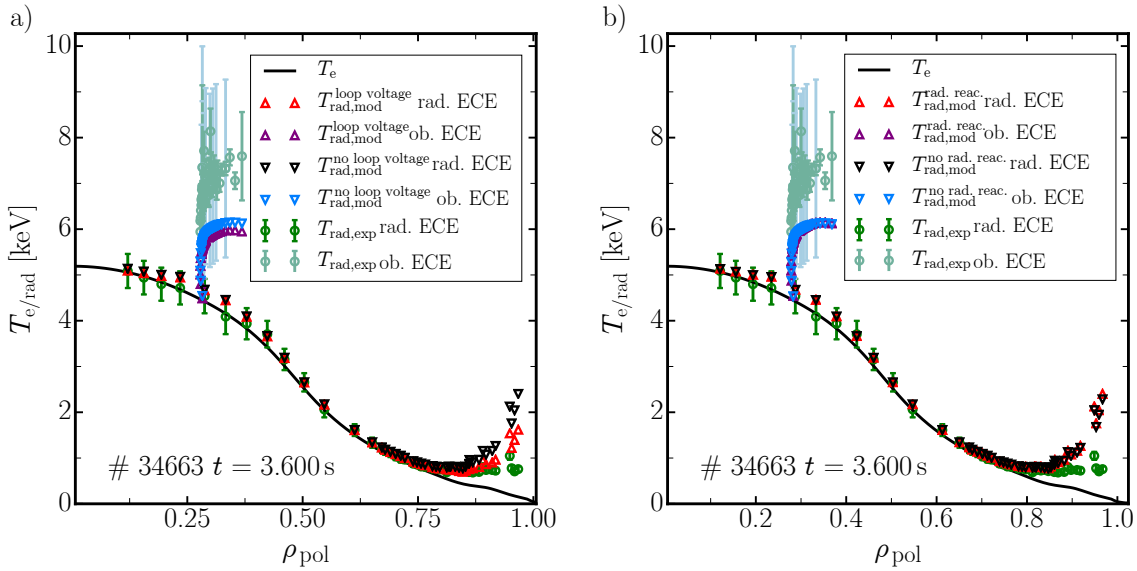

Figure 6.18: a) RELAX calculation with $V_{\mathrm{loop}} = -0.11\,\mathrm{V}$. The loop voltage has little effect onto the plasma core $T_{\mathrm{rad,mod}}$. Near the plasma edge the $T_{\mathrm{rad,mod}}$ are slightly smaller if the loop voltage is taken into account. b) The inclusion of the radiation reaction force has no significant effect on the synthetic measurements.

6.5 Radial diffusion with ECE

Even with the extensions of the physics model discussed in the last two sections there are significant residual discrepancies between the measured and the synthetic T_{rad} values. Radial transport has been identified as a major contributor to the distribution in multiple experiments [7, 36, 37] and it has, so far, been neglected in the calculations.

Aside of the magnetic flutter model [143] and a single numerical study of the radial diffusion coefficient in momentum space for International Thermonuclear Experimental Reactor plasmas [39], little information on the velocity dependence of the radial diffusion coefficient is available. Accordingly, the study presented in the following has to rely on empirical models for the radial diffusion coefficient $D(u)$::

1. Uniform: $D_a(u) = a$
2. Diffusion of predominately fast electrons: $D_b(u) = bu^2$
3. Diffusion of bulk electrons: $D_{c,d}(u) = c\mathrm{e}^{-\frac{u^2}{du_{\mathrm{th}}^2}}$ with u_{th} the thermal momentum.

Because of its simplicity, the first model has been used universally in all previous studies of non-thermal ECE due to ECCD (e.g. Refs. [7, 37, 144]), except for Ref. [40], where a step function was used to divide the diffusion coefficient into two velocity regimes. The second model is somewhat similar to the magnetic flutter model, which scales with $u_{\parallel}$. The changes with respect to the magnetic flutter model are motivated by two factors. A sensitivity study, independent of the study discussed in the following, showed that the ECE measurements available are insensitive to the pitch angle dependence of the radial diffusion coefficients. Hence, it does not matter much whether the radial diffusion model scales with u or $u_{\parallel}$. Furthermore, the model with a linear dependence on u produces almost the same T_{rad} as model 1. For these two reasons the u^2 dependence was chosen. The last model is motivated by the results from Ref. [39]. They show with gyrokinetic calculations that at mid-radius in International Thermonuclear Experimental Reactor plasmas the radial diffusion is dominant for bulk electrons with small $u_{\parallel}$, which are not expected to contribute to the ECCD significantly. As a direct consequence the authors expect that ECCD is not as strongly affected by radial diffusion as predicted in [35].

The numerical data from the study of Ref. [39] does not apply for the experiments investigated in this section. Even though the International Thermonuclear Experimental Reactor scenario has similar T_{e} values, it has at least five times higher densities and $\frac{T_{\mathrm{e}}}{T_{\mathrm{i}}} \approx 1$ which is very different from $\frac{T_{\mathrm{e}}}{T_{\mathrm{i}}} \approx 10$ present in the scenarios discussed in this chapter. Furthermore, for the scenarios investigated here, radial transport near the magnetic axis is the most relevant, while the radial diffusion coefficients computed for the International Thermonuclear Experimental Reactor scenario of Ref. [39] apply only for mid-radius.

Fortunately, a similar calculation was performed with the GENE code [133] for the plasma core of a discharge performed at the TCV tokamak [145]. This scenario is qualitatively very similar to the experiments discussed here. It has a large T_{e} gradient near the plasma core, low n_{e}, and a large $\frac{T_{\mathrm{e}}}{T_{\mathrm{i}}}$ ratio. While, the exact radial diffusion coefficients as shown in Ref. [39] are not available for this calculation, the momentum

space behavior as observed in the International Thermonuclear Experimental Reactor case could be confirmed by the gyrokinetic calculation of the TCV plasma [146]. Since the ECE measurements are insensitive to the pitch dependence of the radial diffusion coefficient, model 3 qualitatively represents the radial diffusion coefficient of the two gyrokinetic studies.

A parameter scan of a, b, c, d has been performed. The values considered are listed in Table 6.7. Each parameter is varied individually while the others are kept fixed to zero unless otherwise specified. In the following the effect of the three radial diffusion models on the ECE measurements is discussed. The parameters for the comparison are picked from the parameter scan such that the respective model produces the best match with the measurements. These values are listed in Table 6.6.

$a[\mathrm{m^2\,s^{-1}}]$	$b[\mathrm{m^2\,s^{-1}}]$	$c[\mathrm{m^2\,s^{-1}}]$, $d = 1.5$	d, $c = 1.0\,\mathrm{m^2\,s^{-1}}$
0.1	0.1	0.5	1.0
0.5	0.5	1.0	1.5
1.0	1.0	2.5	2.0
5.0	5.0	5.0	3.0
10.0	10.0	10.0	5.0

Table 6.6: Table summarizing the coefficients considered in the sensitivity study.

#	$a\,[\mathrm{m^2\,s^{-1}}]$	$b\,[\mathrm{m^2\,s^{-1}}]$	$c\,[\mathrm{m^2\,s^{-1}}]$	d
33697	1.0	1.0	0.5	1.5
33705	1.0	5.0	2.5	1.5
34663	0.5	0.5	0.5	1.5

Table 6.7: Table summarizing the radial diffusion coefficients of three models that yield the best results for the individual discharges.

Radial diffusion in #34663

In figure Fig. 6.19 a) the synthetic T_{rad} computed without diffusion and with according to Table 6.7 are compared to the oblique ECE measurements. None of the three radial diffusion models produces a significant difference in T_{rad}. Hence, in this scenario the oblique ECE cannot provide any information on the velocity dependence of radial diffusion. Figure 6.19 b) shows the same as Fig. 6.19 a) but for the radial ECE near the plasma edge. Since the contribution by O-mode or third harmonic emission near plasma edge is expected to be small in #34663 the ECE measurements in the range $0.75 < \rho_{\mathrm{pol,res}} < 0.97$ deliver useful information on the distribution function. For

$\rho_{\mathrm{pol,res}} > 0.97$ the optical depth of the X-mode is too small for the measurements to deliver useful results. The T_{rad} predicted by model 1 and model 3 are almost identical and the symbols representing the two models in Fig. 6.19 overlap. In the range $0.75 < \rho_{\mathrm{pol,res}} < 0.97$ model 2 delivers the best agreement with the measurements. This is, however, not entirely conclusive because it is possible that a value slightly smaller than 0.5 for a or c could produce a similar agreement.

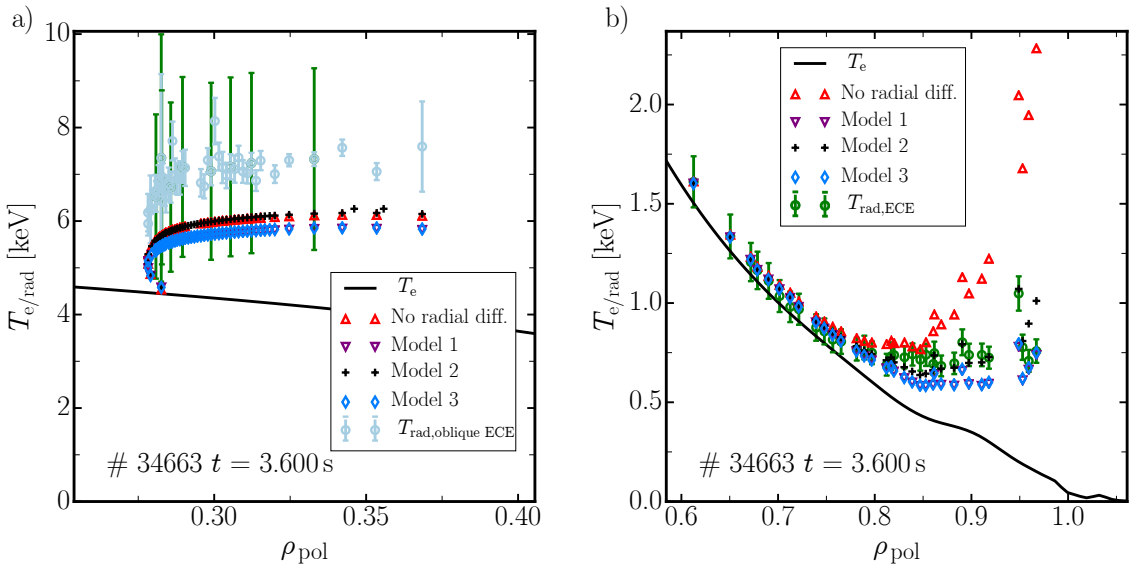

Figure 6.19: Comparison between no radial diffusion, the three different radial diffusion models and the measurements: The red triangles represent $T_{\mathrm{rad,mod}}$ without radial diffusion, the purple upside down triangles correspond to model 1, the black crosses to model 2 and the light blue diamonds to model 3. The values of the parameters are listed in Table 6.7. The symbols corresponding to model 1 and model 3 overlap which makes them difficult to differentiate in a) and b). The measurements of the oblique ECE and their statistical uncertainty are shown in green in a). The additional systematic uncertainty of the measurements is indicated by the light blue error bars for every fifth measurement. In b) the measurements of the radial ECE and their error bars are indicated by the green markers.

Radial diffusion in #33705 and #33697

As discussed previously large uncertainties arise in the modeled T_{rad} if the optical depth is low. For X-mode this affects all channels outside the confined region in #33705 and #33697. Furthermore, optically thin O-mode emission is expected to contribute significantly to the measurements in these two cases. Accordingly, the radial ECE does not deliver any information on the distribution function that can be interpreted with ECRad. Therefore, only the oblique ECE measurements are discussed in the following.

In Fig. 6.20 the T_{rad} measured by the oblique ECE are compared to the case of no radial diffusion and the three different radial diffusion models for #33697 and #33705. There is a noticeable difference between with and without radial diffusion in both cases. The individual velocity dependencies deliver very similar T_{rad}. In #33705 the agreement between measurements and synthetic T_{rad} with radial diffusion is very good, but due to the large statistical errors of the measurements it is not even possible to clearly distinguish between with and without radial diffusion. Accordingly, the measurements do not allow any differentiation between the three different radial diffusion models.

In #33697 on the other hand the theoretical prediction is 25 % smaller than the measurements. The oblique ECE measurements in #33697 are unique because they are sensitive to the electrons that stream in the direction opposite to the ECCD. Hence, it is possible that the electrons causing the observed ECE adversely affect the current drive efficiency. Unfortunately, it is not possible to give a decisive answer given only the measurements from 97. For example, it cannot be ruled out that the discrepancy between modeling and experiment is caused by an unexpectedly large error systematic error in the cross-calibration.

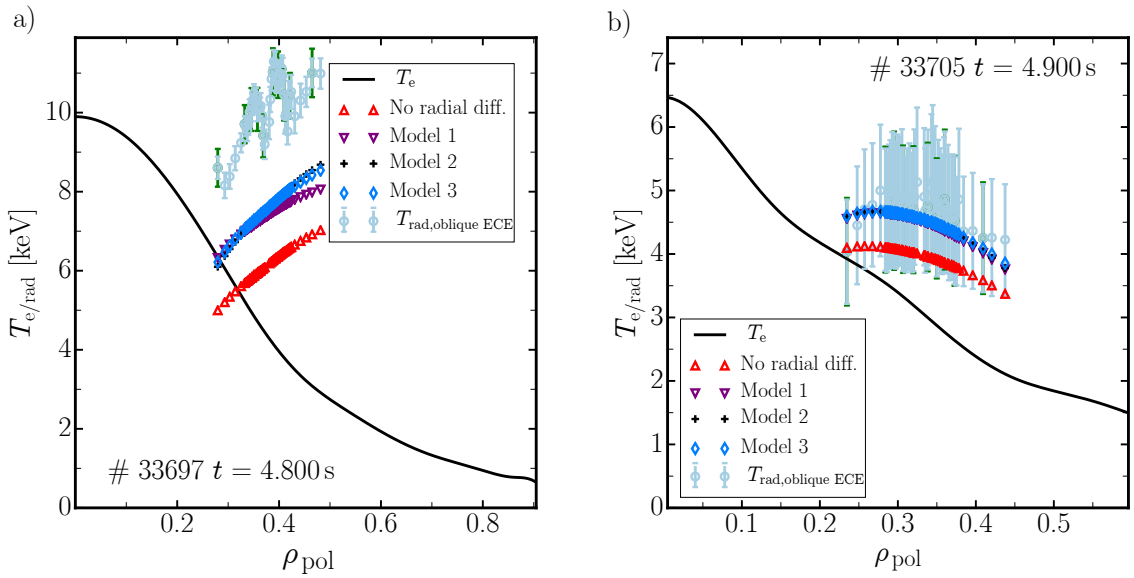

Figure 6.20: As Fig. 6.19 a) but for a) #33697 and b) #33705.

6.6 Conclusions

The non-thermal distributions of three low density discharges with intense ECCD were computed with the RELAX code and the resulting synthetic measurements

were compared against the experimental observations of a radial and an oblique ECE diagnostic. For two discharges, #33705 and #34663 a reasonable agreement between experiment and the theoretical predictions is found, if radial diffusion is included in the calculation of the distribution function (c.f. Fig. 6.20 b) and 6.19). For one of the experiments large discrepancies between model and measurements occur in case of the oblique ECE (c.f. Fig. 6.20 a)).

The details of the validation method of the RELAX and ECRad calculations were presented. Afterwards it was demonstrated that the approach used in previous works does not produce satisfactory results for the ECE measurements at ASDEX Upgrade. To understand the insufficiencies of the modeling the phase space coverage of the radial and the oblique ECE was discussed. It was shown that the finite width of the volume of sight and absorption of the ECRH at the third harmonic has a critical influence on the synthetic ECE measurements of the radial ECE. Furthermore, O-mode emission can influence the measured T_{rad} of the radial ECE critically. The O-mode emission is optically thin and, therefore, strongly affected by wall reflections. Consequently, any ECE measurements with significant O-mode contributions cannot be interpreted with the techniques available in the present work. The parallel electric field was found to have a small, but non-negligible effect on the synthetic ECE measurements and the radiation reaction force is irrelevant for the interpretation of ECE in the present scenarios.

The sensitivity of ECE on the velocity dependence of the radial diffusion coefficient was tested with three empirical models. It was found that ECE cannot differentiate between the three models in the investigated scenarios. Through appropriate choice of the magnitude of the radial diffusion coefficient the measurements of the radial ECE could be described by the modeling. For the oblique ECE the model and the experiment agree in the cases, where the oblique ECE views the electrons streaming in the direction of the ECCD. In the opposite case, where the oblique ECE is mainly sensitive to the half-plain unaffected by the second harmonic deposition of the ECRH, the modeled T_{rad} values are 25 % smaller than the measurements. Unfortunately, this particular alignment of ECRH and oblique ECE was used only in one single discharge and without further experiments a possible error in the cross-calibration cannot be excluded. In the case that this is not an artifact this could be important for the current drive efficiency estimated by codes like RELAX.

7 Summary and Outook

The electron temperature (T_e) is one of the most fundamental properties of a fusion plasma. It can be determined with high spatial and temporal resolution by the Electron Cyclotron Emission (ECE) diagnostic. A calibrated ECE diagnostic measures the radiation temperatures (T_rad) for a set of measurement frequencies ω. Most frequently the radiometer is optimized such that the second harmonic extraordinary mode (X-mode) is the main contributor to the observed T_rad. Often it is possible to infer T_e from T_rad via the Rayleigh-Jeans law. In this case, the position of the measurement is the cold resonance position, where ω is equal to either the fundamental or an harmonic of the electron cyclotron frequency [5]. This ubiquitous approach to interpret the ECE measurements becomes inadequate if (I) emission from plasma layers other than the cold resonance position contributes either due to relativistically down-shifted emission or due to Doppler shifted emission in case of oblique lines of sights. The same applies if (II) the optical depth of the measurement is low, if (III) harmonic overlap occurs or if (IV) the distribution function is non-Maxwellian. With radiation transport modeling [11, 52, 99, 100, 112] applied in the framework of Integrated Data Analysis (IDA) [96] it is possible to overcome the limitations I-III of classical ECE. This was first demonstrated in Ref. [11] for high confinement mode plasmas, by reconstructing the T_e profile from ECE measurements considering shine-through emission and Doppler broadening for second harmonic X-mode spectra at relatively high electron density (n_e) and moderate T_e.

However, the model presented in Ref. [11] is not generally applicable. For example, it overestimates the T_rad mapped to the scrape-off layer (SOL) immensely for plasmas with elevated temperatures ($T_\mathrm{e} > 7\,\mathrm{keV}$) in the plasma core. In this thesis the radiation transport model of Ref. [11] was generalized and the resulting improved radiation transport code was named the Electron Cyclotron radiation transport model for Advanced Data analysis (ECRad). The most important improvements are the addition of geometrical optics raytracing and the implementation of the absorption coefficient presented by Ref. [55]. This absorption coefficient is fully relativistic except for the wave polarization and refractive index which are obtained considering the cold plasma dielectric tensor. The simplification of the wave dispersion is essential to allow a fast and robust implementation of the absorption coefficient. The upgraded absorption coefficient was supplemented with an analogously derived emissivity. Furthermore,

ECRad can simulate the polarization filters used in most ECE diagnostics. The benefits of ECRad over the original electron cyclotron forward model are:

1. Modeling of oblique ECE diagnostics, which is only possible if the improved absorption coefficient and raytracing are included.

2. With the improved absorption coefficient it is possible to model ECE of any harmonic $2 \leq n \leq 5$.

3. The improved absorption coefficient combined with the polarization filter allows the contribution of ordinary mode (O-mode) emission to ECE measurements to be estimated.

4. Electron cyclotron emission due to non-Maxwellian distribution functions can be investigated with ECRad, since the absorption coefficient and emissivity can be calculated individually without relying on Kirchhoff's law.

Another advantage of ECRad is that it provides the birthplace distribution of observed intensity which shows how much each point on the line of sight of the diagnostic contributes to a measurement.

By comparing ECRad with the previous forward model for three discharges with $T_\mathrm{e} > 7\,\mathrm{keV}$ performed at the ASDEX Upgrade tokamak, it was shown that the relativistic mass increase has to be retained in the distribution function to describe the ECE measurements at the plasma edge and in the near SOL. Furthermore, ECRad in conjunction with IDA can treat spectra affected by the so-called "pseudo radial displacement" [115] consistently, and the T_e profiles can even be recovered from ECE spectra subject to harmonic overlap. The latter achievement is especially valuable since it allows ECE measurements of the third harmonic to be performed at high density, where the second harmonic emission is in cut-off and, therefore, unusable. It was also investigated if a similar result can be achieved by measuring the second harmonic O-mode spectrum of the plasma, but it was found that the strong influence of wall reflections inhibits an interpretation of the measurements with ECRad. Another application of ECRad is the cross-calibration of ECE diagnostics against known T_e profiles. Lastly, the birthplace distribution provided by ECRad allows the precise localization of the measurements, which is especially valuable for the study of magneto-hydro-dynamic modes and turbulent T_e fluctuations with correlation ECE .

The capability of ECRad to predict ECE spectra for non-Maxwellian plasmas was exploited to study the effect of electron cyclotron current drive (ECCD) on the distribution function with a radial and an oblique ECE diagnostic. The theoretical predictions for the distribution function where provided by the bounce averaged, quasi-linear Fokker-Planck code RELAX. To describe the ECE measurements at the ASDEX Upgrade

tokamak it is necessary to include third harmonic absorption of the electron cyclotron resonance heating (ECRH) in the RELAX calculations even though almost the entire power is absorbed at the second harmonic. Furthermore, it was shown that O-mode emission can have a strong impact on the ECE measurements of non-thermal plasmas. It was studied to which extent ECE measurements can quantify the influence of radial transport on the steady-state distribution. On the one hand the ECE measurements sensitive to the electrons contributing positively to the driven current could be explained by the model if radial diffusion coefficients between 0.5 and$1.0\,\mathrm{m^2\,s^{-1}}$ were considered. The velocity space dependence of the radial diffusion coefficient could not be resolved with the ECE measurements. On the other hand the ECE measurements sensitive to the electrons streaming in the direction opposite to the driven current were underpredicted by the model by 25 %.

In summary, with ECRad a robust and versatile tool has been developed, that, when paired with IDA, considerably improves the accuracy of T_e profile reconstructions and extends the operational space of the ECE diagnostic. Furthermore, ECRad allows ECE measurements of non-thermal plasmas to be interpreted quantitatively for the first time, allowing the verification of codes like RELAX with ECE.

Outlook

If current models for ECCD truly underestimate the fraction of electrons streaming in the direction opposite to the current drive, they also would overestimate the current drive efficiency. This could be a critical problem since the current drive efficiency frequently enters the design of plasma scenarios and even entire reactors. An example of the latter would be the ECRH system at International Thermonuclear Experimental Reactor, which was optimized to be just powerful enough to allow the stabilization of magnetic islands via ECCD. To confirm or refute the underprediction of counter-streaming electrons further experiments, featuring the simultaneous usage of two oblique ECE diagnostics, were planned. Unfortunately, these experiments were first delayed due to technical difficulties of the oblique ECE system and problems with the ECRH launchers, and then canceled when a major water leak ended the experimental campaign of ASDEX Upgrade prematurely. Consequently, it was not possible to complete these experiments within the framework of this thesis, and they will have to remain subject of future work.

Appendix

1 Upper limit estimate for the absorption coefficient

The upper-limit estimate is based on the approach given by Hutchinson [5], which uses the following approximations:

- The electrons are thermally distributed.
- The refractive index is $N_\omega = 1$.
- The propagation is quasi-perpendicular.
- The "polarization factor" is approximated in the non-relativistic limit. Hence, all factors $\gamma \approx 1$, which implies that $\beta_{\perp/\parallel} = u_{\perp/\parallel}$. Of course to have any relativistic broadening this approximation must not be applied to the resonance condition, where γ is fully retained.

The two distinctions to the treatment given by Hutchinson are that the fully relativistic distribution function is retained and that dimensionless momentum is used as the coordinate system. In the following expression the integration over $u_\perp$ is already carried out:

$$\alpha_{\omega,n,\mathrm{approx}} \approx \alpha_0 \int_{u_{\parallel,-}}^{u_{\parallel,+}} f(u_\perp(u_\parallel), u_\parallel) \left(\frac{u_\perp(u_\parallel)}{2} \right)^{2n+1} \mathrm{d}u_\parallel \tag{1}$$

$$\alpha_0 := \frac{(e\omega_{\mathrm{c},0})^2 n_\mathrm{e}}{8\pi\epsilon_0 c_0} \frac{n^{2(n-1)}}{(m-1)!} (\sin\theta)^{2m-1} (\cos^2\theta + 1)$$

$$u_\perp(u_\parallel) := \sqrt{\left(\frac{n}{\varpi} - \cos\theta \right)^2 - u_\parallel^2 - 1}$$

$$u_{\parallel,\pm} = \frac{\frac{n}{\varpi}\cos\theta \pm \sqrt{\frac{n^2}{\varpi^2} + \cos^2\theta - 1}}{1 - \cos^2\theta}$$

Since the distribution function can be expressed as a simple exponential function in $u_\parallel$ the equation above has an analytical solution that can be obtained by repeatedly applying integration by parts. Although the expression obtained after the integration in $u_\parallel$ is quite lengthy, the computational cost is still small since numerical integration is not necessary and no Bessel function needs to be evaluated.

This formula works very well as an upper limit for the absorption coefficient. This is demonstrated in Fig. 1, where the approximation (dashed lines) is compared to the absorption coefficient given by Eq. (2.12) (solid lines). For the comparison the two absorption coefficients are shown as functions of the measured frequency $f = \frac{\omega}{2\pi}$ and the cyclotron frequencies $f_c = \frac{\omega_{c,0}}{2\pi}$. Figure 1 a) shows the two absorption coefficients for a measured frequency f =140 GHz and n_e = 10.0, 8.0 and 6.0 $\times 10^{19}$ m^{-3}. In Fig. 1 b) f =110 GHz and n_e=6.0, 4.0 and 2.0 $\times 10^{19}$ m^{-3}. For the low frequency case smaller densities are necessary to avoid cut-off. For these calculations T_e=8 keV and θ =80° are considered. For all the combinations of n_e, f and $\frac{\omega}{\omega_{c,0}}$ Eq. (1) show in Fig. 1 delivers an upper limit for the absorption coefficient given by Eq. (2.12).

The criterion which is used to decide, if Eq. (2.12) has to be evaluated is:

$$\tau_{\text{crit}} < \tau_{\text{approx}} = 2\Delta s \sum_{n=2}^{3} \alpha_{\omega,n,\text{approx}} \tag{2}$$

The Δs is the local step size. In practice a $\tau_{\text{crit}} = 1.0 \times 10^{-8}\,\text{m}^{-1}$ has proven to not alter the forward modeled T_{rad} of the test cases while improving the performance of the model considerably.

2 Wall reflection model assuming isotropic back ground

Assuming there is a layer of homogeneous and isotropic radiation with intensity $I_{\omega,0}$ in between the plasma and the vessel wall, as illustrated by Fig. 2, one can formulate a

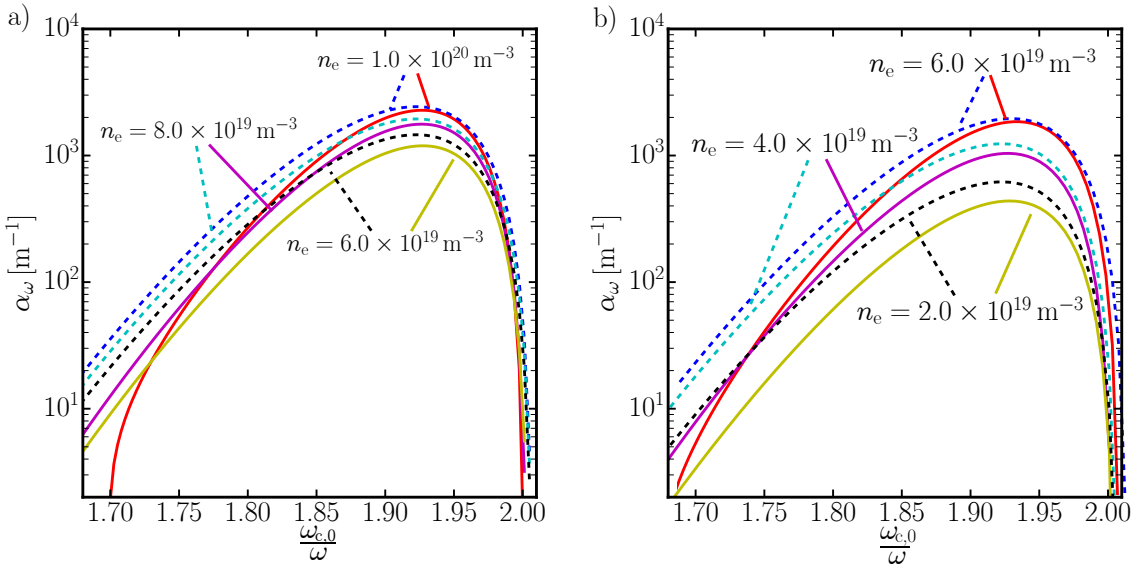

Figure 1: The absorption coefficient given by Eq. (2.12) (sold lines) is compared to the absorption coefficient given by the crude approximation (c. f. Eq. (1)) (dashed lines) for six n_e and two different measured frequencies f_{ECE} =140 GHz (Fig. 1 a)) and f_{ECE} =105 GHz (Fig. 1 b)) as a function of the measured frequency normalized by the cyclotron frequency. For all frequency- and density combinations the upper limit estimation is larger than the absorption coefficient given by Eq. (2.12).

power balance between the energy flowing in and out of this layer [147]:

$$
\begin{aligned}
&I^{\sigma}_{\omega,0}\int_P\int_{\vec{n}(\vec{x})\cdot\vec{k}<0}\vec{n}(\vec{x})\cdot\vec{k'}\,\mathrm{d}\Omega_{\vec{k'}}\mathrm{d}S + I^{\sigma}_{\omega,0}\int_W\int_{\vec{n}(\vec{x})\cdot\vec{k}>0}\vec{n}(\vec{x})\cdot\vec{k'}\,\mathrm{d}\Omega_{\vec{k'}}\mathrm{d}S = \\
&I^{\sigma}_{\omega,0}\int_P\int_{\vec{n}(\vec{x})\cdot\vec{k}>0}\mathrm{e}^{-\tau^{\sigma}(\vec{x},\vec{k'})}\vec{n}(\vec{x})\cdot\vec{k'}\,\mathrm{d}\Omega_{\vec{k'}}\mathrm{d}S + \\
&I^{\sigma}_{\omega,0}\int_W\int_{\vec{n}(\vec{x})\cdot\vec{k}<0}\boldsymbol{R}(\vec{n}(\vec{x}),\vec{k'})\vec{n}(\vec{x})\cdot\vec{k'}\,\mathrm{d}\Omega_{\vec{k'}}\mathrm{d}S + \\
&\int_P\int_{\vec{n}(\vec{x})\cdot\vec{k}>0}I_{\omega}(\vec{x},\vec{k'})\vec{n}(\vec{x})\cdot\vec{k'}\,\mathrm{d}\Omega_{\vec{k'}}\mathrm{d}S
\end{aligned}
\tag{3}
$$

In Eq. (3) it is assumed that there is no plasma at the boundary of the layer of isotropic radiation. Hence, the direction of the energy flow is identical to the wave vector $\vec{k}$. The integrals are over the solid angle, plasma surface P and the wall surface W. The direction of the energy flow is indicated by the sign of $\vec{n}(\vec{x})\cdot\vec{k}$. The first term on the l.h.s. is the energy flow of the isotropic radiation $I_{\omega,0}$ into the plasma volume- The second term is on the l.h.s. is the energy flow of $I_{\omega,0}$ to the machine wall. Both terms are energy sinks which have to be balanced by the sources given on r.h.s. The first term

on the r.h.s. is the shine-through of $I_{\omega,0}$ through the plasma. Since the layer containing the isotropic radiation surrounds the plasma any shine-though is able to reenter said layer. The second term on the r.h.s. is the radiation that is reflected by the vessel wall. The last term on the r.h.s. is the radiation emitted by the plasma.

Equation 3 is coupled to the geometrical optics equation through the shine-through term and the emission of the plasma, which depend on the trajectory of the waves. Furthermore, the emission term is also coupled to the radiation transport equation and the shine-through term requires the integral of the absorption coefficient along the path of the wave.

Hence, to solve the integrals given by the first and third term on the r.h.s. it is necessary solve the geometrical optics equations and the radiation transport equation. Furthermore, Eq. (3) is actually a set of two coupled equations, because of the polarization state σ which can either be X-mode or O-mode. The equations are coupled through the wall reflection tensor $\boldsymbol{R}$ which includes polarization scrambling. The cross polarization terms depend on the orientation of the wall tiles and the polarization vector of the wave with wave vector $\vec{k}$. Hence, this term implicitly depends on the plasma parameters at the separatrix, because of the connection to the polarization state of the wave. In practice, it is possible to obtain the intensity emitted by the plasma I_ω, the optical depth τ_ω and the polarization state of the wave with one single computation for each $\vec{x}$ and $\vec{k}$. Nevertheless, the solution of Eq. (3) requires immense computational resources, especially because Eq. (3) has to be solved numerically if the dependence of the wall reflection tensor on $\vec{k}$ and $\vec{n}(\vec{x})$ is considered. Furthermore, it is not sufficient to solve Eq. (3) just once, but rather it has to be solved for each measured frequency independently. Hence, without further simplifications Eq. (3) is too cumbersome to be useful for data analysis purposes.

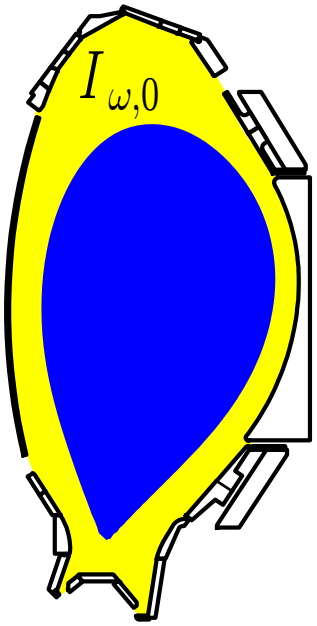

Figure 2: Illustration of an isotropic and homogeneous layer of radiation between plasma and vessel wall. The layer is marked in yellow and the plasma is colored blue.

3 Output of ECRad

At the time of this writing the output of ECRad is stored in a large amount of ASCII encoded files, which are not optimally organized. This is compensated by the Graphical user interface (GUI) of ECRad that automatically reads the ASCII output and stores

them as a single binary file using the Matlab [148] formatting ".mat". Within the ".mat" file the dimensions are arranged according to the C convention, hence:

- First dimension is time
- Second dimension is channel number
- Third dimension is ray number
- Forth dimension is ray line of sight index

For many quantities there is either a "_comp" or secondary counter part. These quantities are derived from the secondary absorption coefficient, which is either the fully relativistic treatment in case of thermal plasmas, or according to a thermal distribution in case of non-thermal plasmas.

Table 1 and Table 2 summaries the fields of the ".mat"-file that contain the results. The results file also contains all information on the configuration used for the calculation. Furthermore, there is some information that is not listed in the section on the configuration file (see Table 3):

4 Most important parameters of the RELAX calculations

Table 4 summarizes the most important parameters that were used for the RELAX calculations.

"time"	time of the calculations [s]
"edition"	Edition of the output file
"Trad"	Radiation temperatures of the primary model [keV]
"tau"	Optical depth primary model (dimensionless)
"Trad_comp"	Radiation temperatures of the secondary model [keV]
"tau_comp"	Optical depth of secondary model
"s_cold", "R_cold", "z_cold", "rhop_cold"	Cold resonance (LOS, R,z, ρ_{pol})
"s_warm", "R_warm", "z_warm", "rhop_warm"	Warm resonance (LOS coordinate, R,z, ρ_{pol})
"s_warm_secondary", "R_warm_secondary", "z_warm_secondary", "rhop_warm_secondary"	Warm resonance secondary model (LOS coordinate, R,z, ρ_{pol})
"launch_x", "launch_y", "launch_z"	Launching point [cm]
"launch_f"	frequency [Hz]
"launch_pol_ang", "launch_tor_ang"	launching angles (TORBEAM convention) [°]
"BPDX", "BPD_secondX", "BPDrhopX"	Birthplace distribution binned to HFS/LFS ρ_{pol} X-mode
""BPDX", "BPD_secondO", "BPDrhopO"	Birthplace distribution binned to HFS/LFS ρ_{pol} O-mode
"sX", "xX", "yX", "zX" "rhopX"	LOS of each ray s is best for interpolation/remapping first ray is central ray X-mode
"sO", "xO", "yO", "zO" "rhopO"	Same as above O-mode

Table 1: Fields containing results of the ECRad calculation.

"HX"	Hamiltonian from ray tracing if absolute value larger 1.0×10^{-4} the ray tracing calculation might be erroneous X-mode
"HO"	Same as above O-mode
"NX", "NcX"	Ray refractive index and refractive index from cold dispersion relation
"thetaX"	$\theta := \arccos\left(\frac{\vec{B}\cdot\vec{N}}{\lvert\vec{B}\rvert\lvert\vec{N}\rvert}\right)$ [rad] X-mode
"thetaO"	Same as above O-mode
"TeX"	T_e [eV] X-mode
"TeO"	T_e [eV] O-mode
"ray_BPDX", "ray_BPD_secondX"	Birthplace distribution along ray, primary and secondary model X-mode
"ray_BPDO", "ray_BPD_secondO"	Same as above O-mode
"calib"	calibration factors [keV $\mathrm{V}^{-1}\,\mathrm{s}^{-1}$] requires the GUI
"rel_dev"	relative deviation of calibration [%] requires the GUI
"calib_mat"	calibration factors time dependent [keV $\mathrm{V}^{-1}\,\mathrm{s}^{-1}$] requires the GUI
"std_dev_mat"	std. deviation of signal time dependent [V s] requires the GUI

Table 2: Continuation of Table 1.

"dstf"	Mode of the calculation Options are "TB" for thermal "LU" for distribution from LUKE "Re" for distribution from RELAX
"used_diags"	Considered diagnostics
"used_diags"	Considered diagnostics
"Diags_exp" "Diags_diag" "Diags_ed"	Diagnostic information irrelevant for TCV at this time
"Extra_arg_1", "Extra_arg_2", "Extra_arg_3",	extra arguments for diag diagnostic specific (used in GUI)
"Ext_launch_geo"	Launch of external diagnostic
"rhop", "Te", "ne"	ρ_{pol}, T_{e}, n_{e} Profiles from external data
"eq_R", "eq_z", "eq_Psi" "eq_rhop", "eq_Br", "eq_Bt" "eq_Bz", "eq_special"	R, z, $\mathbf{\Psi}$ ρ_{pol}, B_{r}, B_{t} B_{z}, array with magn. axis position, ect. From external data

Table 3: Fields containing the configuration of the ECRad calculation.

Parameter	Value
nsurf	60
iya	96
ixa	192
xmax	3.0
tstep	1.0×10^{-5} or 1.0×10^{-6} in case of strong radial diffusion
nfcga	0
nlcheb	False
nlfixn	True
kdneg	0
nltrun	True
nlcofi	False
nlrnaw	False
model_ecdiff	2
quick	True
ndispr	10000
ncoecd	500
nhmin	2
nhmax	3
PDNPAR	0.001
PDOCO	0.001
PDPHI	0.01
nltorx	False
temedg	0.07
denedg	0.33×10^{13}

Table 4: Summary of the most important RELAX parameters used for all RELAX calculations.

Glossary

ASDEX Upgrade The Axial Symmetric Divertor EXperiment Upgrade is a medium sized tokamak operated at the Max-Planck-Institute for Plasma physics in Garching bei München. 3, 4, 6, 7, 10, 11, 14, 16–18, 22, 31, 33–36, 39, 40, 43, 45, 46, 48, 52, 53, 56, 61, 67–70, 72, 73, 75, 81–83, 85, 87, 90, 91, 96, 103, 106, 112, 116, 117

Angle between wave vector and magnetic field $\theta = \arccos\left(\frac{\vec{k}\cdot\vec{B}}{|\vec{k}|\cdot|\vec{B}|}\right)$. 12

Birthplace distribution of observed intensity The birthplace distribution function of observed intensity quantifies how much each point within the volume of sight of the diagnostic contributes to the measurement. Depending on the application it can be binned to a magnetic flux coordinate system or be represented at a function in three dimensional space. 21

Black body intensity $I_{\omega,\mathrm{bb}} = \frac{8\pi^3 c_0^2}{\omega^2 k_\mathrm{b} T_\mathrm{e}}$. 10

Edge localized mode In most H-mode plasmas the edge transport barrier is not stable and breaks down periodically. This break down is caused by the edge localized modes, which are magneto hydrodynamic modes that occur at the very edge of the plasma. 40

Electron cyclotron frequency $\omega_\mathrm{c} = \frac{eB}{m_\mathrm{e}}$. 4

Electron plasma frequency $\omega_\mathrm{p} = \sqrt{\frac{e^2 n_\mathrm{e}}{\epsilon_0 m_{\mathrm{e},0}}}$. 12

high confinement mode In diverted plasmas an edge transport barrier forms if sufficient heating power is provided. This edge transport barrier gives rise to steep density and temperature gradients. 40, 41, 67, 69, 115

International Thermonuclear Experimental Reactor ITER, Latin for "the way", is a tokamak currently under construction. When finished it will be the largest tokamak ever built. The goal of ITER is to demonstrate that the fusion reactions in a tokamak can produce ten times more energy than the energy needed to ignite and control the plasma. 5, 6, 33, 108, 109, 117

Larmor radius $\rho \mathrm{l} = \frac{v_\perp m_\mathrm{e}}{eB}$. 4

Lorentz factor $\gamma = \frac{1}{\sqrt{1-\beta^2}} = \frac{1}{\sqrt{1-(\beta_\perp^2+\beta_\parallel^2)}} = \sqrt{1+u^2} = \sqrt{1+u_\perp^2+u_\parallel^2}$. 15

Normalized electron cyclotron frequency $Y = \frac{\omega_{\mathrm{c},0}}{\omega}$. 12

Normalized electron plasma frequency $X = \frac{\omega_\mathrm{p}^2}{\omega^2}$. 12

Parallel refractive index $N_\parallel := N_\omega \cos\theta$. 12

Perpendicular refractive index $N_\perp := N_\omega \sin\theta$. 12

Pitch angle $\zeta = \frac{u_\parallel}{u}$. 30

rho poloidal

$$\rho_\mathrm{pol} := \sqrt{\frac{\Psi_\mathrm{pol} - \Psi_\mathrm{pol,ax}}{\Psi_\mathrm{pol,sep} - \Psi_\mathrm{pol,ax}}}$$

Where Ψ_ax is the poloidal flux through the ring defined by the magnetic axis, the center of the plasma. Similarly Ψ_sep is the flux through the ring formed by the boundary of the confined plasma. 10

Total dimensionless velocity $\beta = \sqrt{\beta_\perp^2 + \beta_parallel^2}$. 18

Two dimensional birthplace distribution of observed intensity The birthplace distribution can be extended to the phase space spanned by real space and momentum space. Two acquire a simple two dimensional representation only a single line of sight, harmonic and frequency is considered. In this case the resonance conditions combined with the line of sight coordinate yields the two dimensional birthplace distribution which represents the contribution of each point in phase space. 23

Wave vector normalized to the value of the refractive index $\boldsymbol{N} := \frac{c_0 \boldsymbol{k}}{\omega}$. 11

Acronyms

B absolute value of the ambient magnetic field. 4

I_ω spectral intensity of the wave. 10

N_{ray} ray refractive index. 13

T_{e} electron temperature. i, 3–7, 10, 11, 18, 19, 22, 30, 34, 35, 38–42, 44–47, 49, 50, 53, 54, 57, 59, 61–64, 68–71, 73–75, 78, 82, 83, 86–88, 93–95, 97, 103, 104, 106, 109, 115–117, 120

T_{rad} radiation temperatures. 10, 18, 22, 38, 46–55, 57, 61, 63–70, 72, 73, 75, 82, 83, 87, 88, 94, 95, 97–99, 102, 103, 105–111, 113, 115, 121

Z_{eff} effective ion charge. 31

α_ω absorption coefficient. 13

$\boldsymbol{B}$ ambient magnetic field. 11

$\boldsymbol{e}$ Polarization vector normalized by the Poynting flux. 15

$\boldsymbol{k}$ wave vector. 11

ϵ_0 vacuum permittivity. 12

ω (angular) wave frequency. 4

c_0 vacuum speed of light. 10

e elementary charge. 4

j_ω emissivity. 13

k_{b} Boltzmann constant. 16

m_{e} elementary charge. 4

n harmonic number. 4

n_e electron density. 10, 11, 29, 39–43, 45–48, 50, 52, 54, 61, 63, 64, 67, 69, 70, 72, 78, 82, 85–88, 93–95, 109, 115, 120

s arc length. 11

$u_\parallel$ dimensionless momentum parallel to the magnetic field. 15

$u_\perp$ dimensionless momentum perpendicular to the magnetic field. 15

$v_\perp$ velocity perpendicular to the magnetic field. 4

CPO Consistent Physical Object. 57

ECCD electron cyclotron current drive. ii, 5–7, 24–26, 29, 31, 38, 40, 41, 43, 44, 54, 56, 85, 86, 88–94, 96, 98, 100, 102, 104, 106–113, 116, 117

ECE Electron Cyclotron Emission. i, ii, 3–7, 9–14, 16–26, 30, 31, 33–42, 45–48, 50–55, 57, 59–78, 80–83, 85–88, 90–92, 94–113, 115–117

ECFM electron cyclotron forward model. 59–63

ECRad Electron Cyclotron radiation transport model for Advanced Data analysis. i, ii, iv, 6, 7, 46, 49–53, 57, 59–70, 81–83, 85, 86, 89, 90, 94, 95, 97, 105, 106, 111, 112, 115–117, 122, 124, 126

ECRH electron cyclotron resonance heating. ii, 5–7, 22, 24–29, 33–35, 37, 40–43, 50, 57, 61, 68, 78, 86, 89–91, 93, 95–100, 102–104, 106, 107, 112, 113, 117

GUI Graphical user interface. 52, 56, 57, 122

HFS high-field side. 4, 5, 36, 51, 63, 70–72, 74, 75

ICRH ion cyclotron resonance heating. 34, 35

IDA Integrated Data Analysis. 6, 7, 45, 46, 54, 56, 59, 61, 62, 71, 73, 82, 83, 85–88, 115–117

IDE Integrated Data analysis Equilibrium. 56, 81, 107

LFS low-field side. 4, 5, 35, 36, 63, 67, 70–75, 105

LOS line of sight. 5, 9–11, 20, 22, 35, 38, 46, 50, 55, 60, 63, 67, 75–77, 81, 91, 100

LSN Lower Single Null. 33

MHD Magnetohydrodynamic. 40, 56, 81–83

NBI Neutral Beam Injection. 33–35, 40, 42, 78–81

O-mode ordinary mode. i, 7, 11, 36, 50, 64, 67–69, 83, 86, 104, 106, 110, 113, 116, 117

SOL scrape-off layer. 49, 61, 63–66, 68, 82, 115, 116

USN Upper Single Null. 33, 41, 43, 88

VOS volume of sight. 23, 86, 98, 100

X-mode extraordinary mode. 11, 36, 38, 48, 50, 60, 64, 67–69, 72, 73, 83, 86, 95, 103, 104, 106, 110, 115

Bibliography

[1] A. M. Weinberg et al. “Limits to the Use of Energy: The limit to population set by energy is extremely large, provided that the breeder reactor is developed or that controlled fusion becomes feasible”, *American Scientist* 58, 4 (1970), pp. 412–418.

[2] G. Federici et al. “European DEMO design strategy and consequences for materials”, *Nuclear Fusion* 57, 9 (2017), p. 092002.

[3] L. El-Guebaly et al. “Current challenges facing recycling and clearance of fusion radioactive materials”, *University of Wisconsin Fusion Technology Institute Report* (2005).

[4] F. F. Chen. *Introduction to plasma physics*. Springer Science & Business Media, 2012.

[5] I. Hutchinson. *Principles of Plasma Diagnostics*. Cambridge University Press, 1987. ISBN: 9780521326223.

[6] R. W. Harvey et al. “Electron cyclotron emission from nonthermal tokamak plasmas”, *Physics of Fluids B: Plasma Physics* 5, 2 (1993), pp. 446–456. eprint: https://doi.org/10.1063/1.860530.

[7] S. Coda et al. “The effect of ECRH on the electron velocity distribution function”, *Plasma Physics and Controlled Fusion* 48, 12B (2006), B359.

[8] E. d. l. Luna et al. “Electron cyclotron emission radiometer upgrade on the Joint European Torus (JET) tokamak”, *Review of Scientific Instruments* 75, 10 (2004), pp. 3831–3833.

[9] S. Schmuck et al. “Electron cyclotron emission measurements on JET: Michelson interferometer, new absolute calibration, and determination of electron temperature”, *Review of Scientific Instruments* 83, 12 (2012), p. 125101.

[10] C. Sozzi et al. “Optical design of the oblique ECE antenna system for JET”, *Fusion engineering and design* 74, 1-4 (2005), pp. 691–696.

[11] S. K. Rathgeber et al. “Estimation of edge electron temperature profiles via forward modelling of the electron cyclotron radiation transport at ASDEX Upgrade”, *Plasma Physics and Controlled Fusion* 55, 2 (2013), p. 025004.

[12] I. G. J. Classen et al. “Dual array 3D electron cyclotron emission imaging at ASDEX Upgrade”, *Review of Scientific Instruments* 85, 11D833 (2014).

[13] S. J. Freethy et al. “Validation of gyrokinetic simulations with measurements of electron temperature fluctuations and density-temperature phase angles on ASDEX Upgrade”, *Physics of Plasmas* 25, 5 (2018), p. 055903. eprint: `https://doi.org/10.1063/1.5018930`.

[14] M. E. Austin et al. “Electron cyclotron emission radiometer upgrade on the DIII-D tokamak”, *Review of Scientific Instruments* 74, 3 (2003), pp. 1457–1459. eprint: `https://doi.org/10.1063/1.1530387`.

[15] B. Tobias et al. “Commissioning of electron cyclotron emission imaging instrument on the DIII-D tokamak and first data”, *Review of Scientific Instruments* 81, 10 (2010), p. 10D928.

[16] A. White et al. “A correlation electron cyclotron emission diagnostic and the importance of multifield fluctuation measurements for testing nonlinear gyrokinetic turbulence simulations”, *Review of Scientific Instruments* 79, 10 (2008), p. 103505.

[17] S. Schmuck et al. “Design of the ECE diagnostic at Wendelstein 7-X”, *Fusion Engineering and Design* 84, 7-11 (2009), pp. 1739–1743.

[18] Y. Nagayama et al. “Electron cyclotron emission diagnostics for helical plasma in Large Helical Device,” *The 30th International Conference on Plasma Science, 2003. ICOPS 2003. IEEE Conference Record - Abstracts.* 2003, pp. 271–.

[19] A. Mase et al. “Electron cyclotron emission imaging on a Large Helical Device”, *Review of scientific instruments* 74, 3 (2003), pp. 1445–1448.

[20] Y. Kogi et al. “Development of multichannel intermediate frequency system for electron cyclotron emission radiometer on KSTAR Tokamak”, *Review of Scientific Instruments* 79, 10 (2008), 10F115.

[21] G. Yun et al. “Development of KSTAR ECE imaging system for measurement of temperature fluctuations and edge density fluctuations”, *Review of Scientific Instruments* 81, 10 (2010), p. 10D930.

[22] G. Bekefi. *Radiation processes in plasmas*. Wiley series in plasma physics. Wiley, 1966.

[23] D. Wagner et al. “Status of the new multi-frequency ECRH system for ASDEX Upgrade”, *Nuclear Fusion* 48, 5 (2008), p. 054006.

[24] J. Lohr et al. “The Electron Cyclotron Resonant Heating System on the DIII-D Tokamak”, *Fusion Science and Technology* 48, 2 (2005), pp. 1226–1237. eprint: https://doi.org/10.13182/FST05-A1073.

[25] Y. Ikeda et al. “The 110-GHz Electron Cyclotron Range of Frequency System on JT-60U: Design and Operation”, *Fusion Science and Technology* 42, 2-3 (2002), pp. 435–451. eprint: https://doi.org/10.13182/FST02-A239.

[26] G. Lee et al. “The KSTAR project: An advanced steady state superconducting tokamak experiment”, *Nuclear Fusion* 40, 3Y (2000), p. 575.

[27] H. Takahashi et al. “Extension of high Te regime with upgraded electron cyclotron resonance heating system in the Large Helical Device”, *Physics of Plasmas* 21, 6 (2014), p. 061506. eprint: https://doi.org/10.1063/1.4884365.

[28] J.-P. Hogge et al. “Preliminary results of top launch third harmonic X-mode electron cyclotron heating in the TCV tokamak”, *Nuclear Fusion* 43, 11 (2003), p. 1353.

[29] V. Erckmann et al. “Electron Cyclotron Heating for W7-X: Physics and Technology”, *Fusion Science and Technology* 52, 2 (2007), pp. 291–312. eprint: https://doi.org/10.13182/FST07-A1508.

[30] C. Karney et al. “Currents driven by electron cyclotron waves”, *Nuclear Fusion* 21, 12 (1981), p. 1549.

[31] R. L. Haye et al. “Prospects for stabilization of neoclassical tearing modes by electron cyclotron current drive in ITER”, *Nuclear Fusion* 49, 4 (2009), p. 045005.

[32] E. Westerhof et al. *RELAX: A Computer Code for the Study of Collisional and Wave Driven Relaxation of the Electron Distribution Function in Toroidal Geometry*. Rijnhuizen report. FOM-Instituut voor Plasmafysica "Rijnhuizen", 1992.

[33] J. Decker et al. “DKE: a fast numerical solver for the 3-D relativistic bounce-averaged electron drift kinetic equation”, (2005).

[34] R. Harvey et al. “The cql3d fokker-planck code”, *IAEA TCM, Montreal* (1992).

[35] N. Bertelli et al. “Consequences of finite transport on the effectiveness of ECCD for neoclassical tearing mode stabilization in ITER”, *Nuclear Fusion* 49, 9 (2009), p. 095018.

[36] R. Harvey et al. “Radial transport and electron-cyclotron-current drive in the TCV and DIII-D tokamaks”, *Physical review letters* 88, 20 (2002), p. 205001.

[37] C. Petty et al. "Effect of Particle Transport on the Measured Electron Cyclotron Current Drive Profile at High Relative Power Density", *Fusion Science and Technology* 57, 1 (2010), pp. 10–18.

[38] S. Coda et al. "The effect of ECRH on the electron velocity distribution function", *Plasma Physics and Controlled Fusion* 48, 12B (2006), B359.

[39] F. Casson et al. "Effect of turbulence on electron cyclotron current drive and heating in ITER", *Nuclear Fusion* 55, 1 (2015), p. 012002.

[40] P. Nikkola et al. "Modelling of the electron cyclotron current drive experiments in the TCV tokamak", *Nuclear Fusion* 43, 11 (2003), p. 1343.

[41] P. Blanchard et al. "High field side measurements of non-thermal electron cyclotron emission on TCV plasmas with ECH and ECCD", *Plasma Physics and Controlled Fusion* 44, 10 (2002), p. 2231.

[42] J. Kamleitner et al. "Suprathermal electron dynamics and MHD instabilities in a tokamak", *Plasma Physics and Controlled Fusion* 57, 10 (2015), p. 104009.

[43] M. Bornatici et al. "Electron cyclotron emission and absorption in fusion plasmas", *Nuclear Fusion* 23, 9 (1983), p. 1153.

[44] T. H. Stix. *The Theory of Plasma Waves*. McGraw-Hill, 1962.

[45] E. Poli et al. "TORBEAM, a beam tracing code for electron-cyclotron waves in tokamak plasmas", *Computer Physics Communications* 136, 1–2 (2001), pp. 90–104. ISSN: 0010-4655.

[46] D. Farina. "A quasi-optical beam-tracing code for electron cyclotron absorption and current drive: Gray", English, *Fusion Science and Technology* 52, 2 (2007). 14$^{\text{th}}$ Joint Workshop on Electron Cyclotron Emission and Electron Cyclotron Resonance Heating, Santorini, GREECE, MAY 09-12, 2006, pp. 154–160. ISSN: 1536-1055.

[47] A. Kritz et al. *Ray-tracing study of electron-cyclotron heating in toroidal geometry*. Tech. rep. Princeton Univ., NJ (USA). Plasma Physics Lab., 1983.

[48] E. Westerhof. *Implementation of TORAY et JET*. Tech. rep. Stichting voor Fundamenteel Onderzoek der Materie, 1989.

[49] E. Mazzucato. "Relativistic effects on microwave reflectometry", *Physics of Fluids B* 4, 10 (1992), pp. 3460–3461.

[50] E. Westerhof. "Wave propagation through an electron cyclotron resonance layer", *Plasma Physics and Controlled Fusion* 39, 6 (1997), p. 1015.

[51] C. Tsironis. "On the simplification of the modeling of electron-cyclotron wave propagation in thermonuclear fusion plasmas", *Progress In Electromagnetics Research* 47, (2013), pp. 37–61.

[52] N. Marushchenko et al. "Ray-tracing code TRAVIS for ECR heating, EC current drive and ECE diagnostic", *Computer Physics Communications* 185, 1 (2014), pp. 165–176. ISSN: 0010-4655.

[53] D. Farina. "Relativistic dispersion relation of electron cyclotron waves", *Fusion Science and Technology* 53, 1 (2008), pp. 130–138.

[54] H. Bindslev. "Relativistic Effects in Millimeter Wave Applications on Magnetically Confined Plasma," *EC-9: Proceedings of the Ninth Joint Workshop on Electron Cyclotron Emission and Electron Cyclotron Heating*. World Scientific, 1995.

[55] F. Albajar et al. "Electron-cyclotron absorption in high-temperature plasmas: quasi-exact analytical evaluation and comparative numerical analysis", English, *Plasma Physics and Controlled Fusion* 49, 1 (2007), pp. 15–29. ISSN: 0741-3335.

[56] U. Bellotti et al. "Radiative energy transfer in anisotropic, spatially dispersive, weakly inhomogeneous and dissipative media with embedded sources", *La Rivista del Nuovo Cimento (1978-1999)* 20, 5 (1997), p. 1.

[57] S. S. Denk et al. "Analysis of electron cyclotron emission with extended electron cyclotron forward modeling", *Plasma Physics and Controlled Fusion* 60, 10 (2018), p. 105010.

[58] M. Bornatici et al. "Electron-cyclotron absorption AND EMIssion - Vexatae-quaestiones", English, *Physics of Plasmas* 1, 1 (1994), pp. 189–198. ISSN: 1070-664X.

[59] F. Jüttner. "Das Maxwellsche Gesetz der Geschwindigkeitsverteilung in der Relativtheorie", *Annalen der Physik* 339, 5 (1911), pp. 856–882. ISSN: 1521-3889.

[60] G. Garstka et al. "ECE electron temperature mapping errors in high-performance DIII-D discharges", *Fusion Engineering and Design* 53, 1–4 (2001), pp. 123–128. ISSN: 0920-3796.

[61] I. G. J. Classen. "Imaging and control of magnetic islands in tokamaks." PhD thesis. Technische Universiteit Eindhoven, 2007.

[62] V. Tribaldos. "Spatial resolution of the Electron Cyclotron Emission for JET typical Parameters", *EFDA-JET Reports* 2, (2001).

[63] A. Timofeev. "Cyclotron oscillations of an equilibrium plasma", *Moscow Energoizdat* (1985), pp. 56–226.

[64] F. Leuterer et al. *Interaction between an electron and an electromagnetic wave*. 1/355. 2014.

[65] R. Bilato et al. "On the nature of "collisionless" Landau damping", *Communications in Nonlinear Science and Numerical Simulation* 13, 1 (2008), pp. 18–23.

[66] B. V. Chirikov. "A universal instability of many-dimensional oscillator systems", *Physics reports* 52, 5 (1979), pp. 263–379.

[67] J. Killeen et al. *Computational methods for kinetic models of magnetically confined plasmas*. Springer Science & Business Media, 2012.

[68] A. Peeters. "High Power RF Heating and Nonthermal Distributions in Tokamak Plasmas." PhD thesis. Technische Universität Eidhoven, 1994.

[69] R. W. Harvey et al. "Power Dependence of Electron-Cyclotron Current Drive for Low- and High-Field Absorption in Tokamaks", *Phys. Rev. Lett.* 62, (1989), pp. 426–429.

[70] T. Görler et al. "The global version of the gyrokinetic turbulence code GENE", *Journal of Computational Physics* 230, 18 (2011), pp. 7053–7071. ISSN: 0021-9991.

[71] M. Bornatici et al. "The effect of radiative slowing down on current drive by electron cyclotron radiation in fusion plasmas", *Nuclear fusion* 35, 5 (1995), p. 613.

[72] F. Albajar et al. "Importance of electron cyclotron wave energy transport in ITER", *Nuclear Fusion* 45, 7 (2005), p. 642.

[73] M. Bornatici. "Relativistic Fokker-Planck equation for electron cyclotron radiation", *Physica Scripta* 1994, T50 (1994), p. 38.

[74] J. D. Jackson. *Electrodynamics*. Wiley Online Library, 1975.

[75] F. Andersson et al. "Damping of relativistic electron beams by synchrotron radiation", *Physics of Plasmas* 8, 12 (2001), pp. 5221–5229.

[76] E. Hirvijoki et al. "Guiding-centre transformation of the radiation–reaction force in a non-uniform magnetic field", *Journal of Plasma Physics* 81, 5 (2015).

[77] P. Sandquist et al. "Relativistic electron distribution function of a plasma in a near-critical electric field", *Physics of plasmas* 13, 7 (2006), p. 072108.

[78] B. Streibl et al. "Chapter 2: Machine design, fueling, and heating in ASDEX Upgrade," vol. 44. 3. Taylor & Francis, 2003, pp. 578–592.

[79] R. Neu et al. "Overview on plasma operation with a full tungsten wall in ASDEX Upgrade", *Journal of Nuclear Materials* 438, (2013), S34–S41.

[80] J. Roth et al. "Recent analysis of key plasma wall interactions issues for ITER", *Journal of Nuclear Materials* 390, (2009), pp. 1–9.

[81] D. Wagner et al. "Extension of the multi-frequency ECRH system at ASDEX upgrade," *EPJ Web of Conferences*. Vol. 149. EDP Sciences. 2017, p. 03004.

[82] D. Wagner et al. "The new multifrequency electron cyclotron resonance heating system for ASDEX Upgrade", *Fusion Science and Technology* 52, 2 (2007), pp. 313–320.

[83] N. Salmon. "First electron temperature edge measurements on the asdex upgrade tokamak using a heterodyne radiometer", English, *International Journal of Infrared and Millimeter Waves* 15, 1 (1994), pp. 53–60. ISSN: 0195-9271.

[84] S. Rathgeber. "Electron temperature and pressure at the edge of ASDEX Upgrade plasmas." PhD thesis. Ludwig-Maximilians-Universität München, 2013.

[85] H. J. Hartfuss et al. "Heterodyne methods in millimetre wave plasma diagnostics with applications to ECE, interferometry and reflectometry", *Plasma Physics and Controlled Fusion* 39, 11 (1997), p. 1693.

[86] J. Rasmussen et al. "Improved Collective Thomson Scattering measurements of fast ions at ASDEX upgrade," *American Institute of Physics Conference Series*. Vol. 1612. American Institute of Physics Conference Series. 2014, pp. 117–120. arXiv: 1310.2406 [physics.plasm-ph].

[87] S. K. Nielsen et al. "Modification of the collective Thomson scattering radiometer in the search for parametric decay on TEXTOR", *Review of Scientific Instruments* 83, 11 (2012), p. 113508.

[88] S. Preische et al. "Radially localized measurements of superthermal electrons using oblique electron cyclotron emission", *Physics of Plasmas* 3, 11 (1996), pp. 4065–4073. eprint: https://doi.org/10.1063/1.871564.

[89] G. Zhuang et al. "Influence of non-Maxwellian velocity distributions during ECRH and ECCD on electron temperature measurements by Thomson scattering", *Plasma Physics and Controlled Fusion* 47, 9 (2005), p. 1539.

[90] B. Kurzan et al. "Edge and core Thomson scattering systems and their calibration on the ASDEX Upgrade tokamak", *Review of Scientific Instruments* 82, 10 (2011), p. 103501. eprint: http://dx.doi.org/10.1063/1.3643771.

[91] H. Zohm. "Edge localized modes (ELMs)", *Plasma Physics and Controlled Fusion* 38, 2 (1996), p. 105.

[92] A. Hubbard et al. "Threshold conditions for transitions to I-mode and H-mode with unfavourable ion grad B drift direction", *Nuclear Fusion* 52, 11 (2012), p. 114009.

[93] R. C. Wolf. "Internal transport barriers in tokamak plasmas", *Plasma Physics and Controlled Fusion* 45, 1 (2003), R1.

[94] O. P. Ford et al. "Imaging motional Stark effect measurements at ASDEX Upgrade", *Review of Scientific Instruments* 87, 11 (2016), 11E537. eprint: `http://aip.scitation.org/doi/pdf/10.1063/1.4959873`.

[95] A. Mlynek et al. "Fringe jump analysis and implementation of polarimetry on the ASDEX Upgrade DCN interferometer", *Review of Scientific Instruments* 85, 11 (2014), p. 11D408. eprint: `https://doi.org/10.1063/1.4890574`.

[96] R. Fischer et al. "Integrated Data Analysis of profile diagnostics at ASDEX Upgrade", *Fusion Science and Technology* 58, 2 (2010), pp. 675–684. ISSN: 1536-1055.

[97] M. Willensdorfer et al. "Improved chopping of a lithium beam for plasma edge diagnostic at ASDEX Upgrade", *Review of Scientific Instruments* 83, 2, 023501 (2012).

[98] A. Mlynek et al. "Temporally resolved analysis of the response of density and temperature to modulated central electron heating on ASDEX Upgrade", *Nuclear Fusion* 52, 11 (2012), p. 114012.

[99] D. Farina et al. "SPECE: a code for Electron Cyclotron Emission in tokamaks", *AIP Conference Proceedings* 988, 1 (2008), pp. 128–131. eprint: `https://aip.scitation.org/doi/pdf/10.1063/1.2905053`.

[100] R. Sillen et al. *NOTEC, a code to simulate electron cyclotron emission spectra of plasmas which include non-thermal populations*. Tech. rep. Associatie Euratom-FOM, 1987.

[101] A. C. Hindmarsh. "ODEPACK, A Systematized Collection of ODE Solvers", *Scientific Computing* 1, 1 (1983), pp. 55–64.

[102] W. H. M. Clark. "The precision of electron cyclotron emission measurements from DITE Tokamak", *Plasma Physics* 25, 12 (1983), p. 1501.

[103] R. Prater. "Heating and current drive by electron cyclotron waves", *Physics of Plasmas* 11, 5 (2004), pp. 2349–2376. eprint: `https://doi.org/10.1063/1.1690762`.

[104] P. Dierckx. *Curve and surface fitting with splines*. Oxford University Press, 1995.

[105] H. Zohm. *Magnetohydrodynamic stability of tokamaks*. John Wiley & Sons, 2014.

[106] R. Fischer et al. "Coupling of the Flux Diffusion Equation with the Equilibrium Reconstruction at ASDEX Upgrade", *Fusion Science and Technology* 69, 2 (2016), pp. 526–536. eprint: `https://doi.org/10.13182/FST15-185`.

[107] R. Hawryluk. "An empirical approach to tokamak transport," *Physics of plasmas close to thermonuclear conditions*. Elsevier, 1981, pp. 19–46.

[108] *For more details on the TRANSP code, please visit the TRANSP webpage at http://w3.pppl.gov/ pshare/help/transp.htm.*

[109] M. Weiland. In work.

[110] P. J. McCarthy et al. "The CLISTE interpretive equilibrium code", (1999).

[111] O. Sauter et al. "Tokamak coordinate conventions: COCOS", *Computer Physics Communications* 184, 2 (2013), pp. 293–302.

[112] S. S. Denk et al. "Radiation transport modelling for the interpretation of oblique ECE measurements," *19th Joint workshop (EC-19) on Electron Cyclotron Emission (ECE) and Electron cyclotron Resonance Heating (ECRH)*. EPJ, 2016.

[113] G. Sichardt et al. "Electron cyclotron emission measurements at the optically thin plasmas of the stellarator TJ-K," *44th EPS Conference on Plasma Physics*. 2017.

[114] TSUJIMURA et al., *Plasma and Fusion Research* 1, (2016).

[115] M. Sato et al. "Effects of Relativistic Frequency Down-Shift and Optical Thickness on Measurements of Electron Temperature Profile from Electron Cyclotron Emission in Medium Temperature Tokamak Plasmas", *Journal of the Physical Society of Japan* 67, 9 (1998), pp. 3090–3099. eprint: `http://dx.doi.org/10.1143/JPSJ.67.3090`.

[116] W. Suttrop et al. *Practical Limitations to Plasma Edge Electron Temperature Measurements by Radiometry of Electron Cyclotron Emission*. IPP-Report 1/306. Max-Planck-Inst. für Plasmaphysik, 1996.

[117] S. S. Denk et al. "Shine-through in electron cyclotron emission measurements," *44th EPS Conference on Plasma Physics*. Proceedings of the 44th EPS Conference on Plasma Physics. 2017.

[118] D. Bartlett et al. *Recent Progress in the Measurement and Analysis of ECE on JET*. Tech. rep. JET Joint Undertaking, 1995.

[119] J. L. Ségui et al. "Precision and Resolution on Tore-Supra Ece Electron Temperature Profile Measurements," *Electron Cyclotron Emission and Electron Cyclotron Heating*. Ed. by G. Giruzzi. 2003, pp. 209–214.

[120] N. B. Marushchenko et al. "Optimization of ECE Diagnostics for the W7-X Stellarator", *Fusion science and technology* 50, 3 (2006), pp. 395–402.

[121] T. Odstrčil et al. "Optimized tomography methods for plasma emissivity reconstruction at the ASDEX Upgrade tokamak", *Review of Scientific Instruments* 87, 12 (2016), p. 123505.

[122] R. Fischer et al. "Magnetic equilibrium reconstruction using geometric information from temperature measurements at ASDEX Upgrade," *40th EPS Conference on Plasma Physics*. Proceedings of the 40th EPS Conference on Plasma Physics. 2013.

[123] M. E. Austin et al. "Electron temperature measurements from optically gray third harmonic electron cyclotron emission in the DIII-D tokamak", *Physics of Plasmas* 3, 10 (1996), pp. 3725–3731. eprint: `http://dx.doi.org/10.1063/1.871506`.

[124] E. de la Luna et al. "Impact of bulk non-Maxwellian electrons on electron temperature measurements (invited)", *Review of Scientific Instruments* 74, 3 (2003), pp. 1414–1420. eprint: `https://doi.org/10.1063/1.1538354`.

[125] B. Geiger et al. "Fast-ion D-alpha measurements at ASDEX Upgrade", *Plasma Physics and Controlled Fusion* 53, 6 (2011), p. 065010.

[126] M. Willensdorfer et al. "Plasma response measurements of external magnetic perturbations using electron cyclotron emission and comparisons to 3D ideal MHD equilibrium", *Plasma Physics and Controlled Fusion* 58, 11 (2016), p. 114004.

[127] M. Willensdorfer et al. "Dynamics of ideal modes and subsequent ELM-crashes in 3D tokamak geometry from external magnetic perturbations", (2018). submitted to Plasma physics and controlled nuclear fusion.

[128] M. Willensdorfer et al. "Three dimensional boundary displacement due to stable ideal kink modes excited by external n= 2 magnetic perturbations", *Nuclear Fusion* 57, 11 (2017), p. 116047.

[129] M. Willensdorfer et al. "Field-line localized destabilization of ballooning modes in three-dimensional tokamaks", *Physical review letters* 119, 8 (2017), p. 085002.

[130] B. Vanovac et al. "Effects of density gradients and fluctuations at the plasma edge on ECEI measurements at ASDEX Upgrade", *Plasma Physics and Controlled Fusion* 60, 4 (2018), p. 045002.

[131] B. Vanovac et al. "Mode analysis limitations of ECEI & ECE measurements at the plasma edge," To be published in proceedings of the 20th Joint workshop (EC-20) on Electron Cyclotron Emission (ECE) and Electron cyclotron Resonance Heating (ECRH).

[132] O. Samoylov. "Modelling of the Electron cyclotron Transport of MHD modes in a tokamak geometry." PhD thesis. Aix-Marseille-University, 2018.

[133] F. Jenko et al. "Nonlinear electromagnetic gyrokinetic simulations of tokamak plasmas", *Plasma Physics and Controlled Fusion* 43, 12A (2001), A141.

[134] S. J. Freethy et al. "Advances in turbulence measurements using new Correlation ECE and n-T-phase diagnostics at ASDEX Upgrade," To be published in proceedings of the 20th Joint workshop (EC-20) on Electron Cyclotron Emission (ECE) and Electron cyclotron Resonance Heating (ECRH).

[135] J. van Gelder et al. "Comparison of ECE spectra as observed from the high- and low-field side", English, *PLASMA PHYSICS AND CONTROLLED FUSION* 40, 6 (1998), pp. 1185–1199. ISSN: 0741-3335.

[136] J. F. M. van Gelder et al. "Comparison of ECE spectra as observed from the high- and low-field side", *Plasma Physics and Controlled Fusion* 40, 6 (1998), p. 1185.

[137] C. Schlatter et al. "Conditions for anomalous energy and momentum transfer from electrons to ions in ECCD discharges on TCV," *Proceedings of the 33rd European Physical Society Conference on Plasma Physics*. CRPP-CONF-2006-001. 2006.

[138] S. Coda et al. "Electron cyclotron current drive and suprathermal electron dynamics in the TCV tokamak", *Nuclear Fusion* 43, 11 (2003), p. 1361.

[139] E. Westerhof et al. "Resonance broadening as a consequence of strong focussing of electron cyclotron wave beams", *Plasma Physics and Controlled Fusion* 49, 9 (2007), p. 1509.

[140] "TORBEAM 2.0, a paraxial beam tracing code for electron-cyclotron beams in fusion plasmas for extended physics applications", *Computer Physics Communications* 225, (2018), pp. 36–46. ISSN: 0010-4655.

[141] D. Farina et al. "Potential of the ITER electron cyclotron equatorial launcher for heating and current drive at nominal and reduced fields", *Nuclear Fusion* 52, 3 (2012), p. 033005.

[142] R. Prater et al. "Benchmarking of codes for electron cyclotron heating and electron cyclotron current drive under ITER conditions", *Nuclear Fusion* 48, 3 (2008), p. 035006.

[143] A. B. Rechester et al. "Electron Heat Transport in a Tokamak with Destroyed Magnetic Surfaces", *Phys. Rev. Lett.* 40, (1978), pp. 38–41.

[144] C. Petty et al. “Effects of electron trapping and transport on electron cyclotron current drive on DIII-D”, *Nuclear Fusion* 43, 8 (2003), p. 700.

[145] D. Told. “Gyrokinetic microturbulence in transport barriers.” PhD thesis. Universität Ulm, 2012.

[146] T. Dabiel. private communication.

[147] M. Rosenbluth. “Synchrotron radiation in Tokamaks”, *Nuclear Fusion* 10, 3 (1970), p. 340.

[148] U. G. Matlab. “The mathworks”, *Inc., Natick, MA* 1992, (1760).

Acknowledgments

I would like to thank Dr. Rainer Fischer, who supervised me meticulously. The work on this thesis was very dear to me and every setback or failure touched me personally. Fortunately, you always managed to shine a positive light on all of my predicaments and give me a new direction for the continuation of my current project. Additionally, you also taught me how to work thoroughly which is something both, my school and university failed to accomplish.

I also would like to thank Prof. Dr. Ulrich Stroth, who allowed me to work on this quite niche topic. You struck a great balance between letting me work on my own and reigning me in when I was attempting to bite off more than I could swallow. I also appreciate the straightforward communication between us, since subtlety is lost on me.

Many thanks to Dr. Egbert Westerhof. Without your help it would not have been possible to do the analysis of the non-thermal plasmas. I was and still am amazed by the effort you put into this work. An example would be the parallelization you introduced into RELAX together with the HLST, which ended up saving me weeks if not months of run time. Aside of our work with RELAX it was great to be in direct correspondence with you, because I see you as the leading theoretical physicist in the field that this thesis falls into.

I would like to acknowledge Dr. Emanuele Poli and Dr. Omar Maj who were always there for me when I encountered some conundrum regarding electron cyclotron waves or Fokker-Planck theory. The discussions were always pleasant and I learned a lot every time I called upon you.

Many thanks to Dr. Stefan Kragh Nielsen, Dr. Morten Stejner Pedersen and the entire CTS-team. Without your support this work would not have been possible. Your can-do attitude is inspiring and it is truly appreciated that you even sacrificed some of your leisure time to support me and my experiments.

I would like to thank Dr. Matthias Willensdorfer for the enjoyable collaboration on the ECE diagnostic. Furthermore, I would like to thank you for incorporating my model into your research. Since the topic of my thesis is quite niche, there were not many occasions where I could contribute to the work of others and I am glad that you gave me this opportunity.

Similarly, I would like to thank Branka Vanovac, Dr. Simon Freethy and Oleg Samoylov for being a great user base and furthering the development of ECRad and its GUI.

Many thanks to Dr. Jörg Stober and Dr. Francois Ryter for your help in the discharge development and design.

I acknowledge Dr. Martin Schubert and the rest of the ECRH-group for their help with the experiments and the knowledge transfer regarding the more technical aspects of cyclotron waves and their generation.

I also would like to thank my colleagues Guillermo Suarez Lopez and Dr. Tomáš Odstrčil for the interesting and educational discussions during our lunch breaks.

I acknowledge Teobaldo Luda di Cortemiglia, Anton Jansen van Vuuren and Johannes Illerhaus who shared an office with me. The atmosphere in our office was relaxed, yet productive and all of you were very supportive.

Finally, I would like to thank everybody for the very positive working climate at the Max-Planck-Institut für Plasmaphysik. It is an honor to work in a team, where good cooperation flourishes.